Dissertation zur Erlangung des Doktorgrades
der Fakultät für Chemie und Pharmazie
der Ludwig-Maximilians-Universität München

Intrinsic Degradation Factors of Perovskite Semiconductors in Optoelectronic Devices

Fatma Meltem Aygüler

aus

Kazan, Turkey

2018

Erklärung

Diese Dissertation wurde im Sinne von § 7 der Promotionsordnung vom 28.November 2011 von Herrn Dr. Pablo Docampo betreut und von Herrn Prof. Dr. Thomas Bein von der Fakultät für Chemie und Pharmazie vertreten.

Eidesstattliche Versicherung

Diese Dissertation wurde eigenständig und ohne unerlaubte Hilfe bearbeitet.

München, 29.10.2018

_____

Fatma Meltem Aygüler

Dissertation eingereicht am:	29.10.2018
Erstgutachter:	Prof. Dr. Thomas Bein
Zweitgutachter:	Senior Lecturer Dr. Pablo Docampo
Mündliche Prüfung am:	26.11.2018

Acknowledgment

I have never imagined that writing this part will be that difficult. But I have to say that I wouldn't able to finish my PhD without all the people written here. I learned a lot from you not only about science but also about life! Thank you for making my PhD time unforgettable!

First of all, I would like to thank my supervisor Dr. Pablo Docampo. I learned so many things from you that I actually don't know where to start. Thank you for teaching me how to do science properly and how to communicate/collaborate with different people. You showed me that I can work and enjoy at the same time. You created such a harmony in the lab that we never had discussions or problems within the subgroup. I really appreciate that. You always supported and believed in me. When I stop believing myself, you still believed in me and kept saying "I have faith in you! You will do it!". I always remembered these two sentences which were one of my motivations during last 3.5 years when I was close to give up. Thanks for helping me to find my way when I lost it. I really appreciate that your door was always open. Whenever I discussed with you about project, I always left your office with full of motivation and enthusiasm. Thanks for keeping me always enthusiastic about what I am doing. Thank you for your patience and endless support during my PhD.

Another person that I am gratefully thankful is Prof. Thomas Bein. Thank you Thomas for being supportive and your inspiring ideas/suggestions/questions during our subgroup and group meetings. Thanks for providing optimum working conditions and the latest equipments in the group which saved so much time during my PhD. I really appreciate that you made me think in another perspective with your suggestions or comments in the meetings. I also think that I am one of the luckiest PhD students who could sing and dance with her professor in the conferences and Christmas parties in the group.

I would like to thank my defense committee, Prof. Achim Hartschuh, Prof. Alexander Urban, Prof. Konstantin Karaghiosoff and Prof. Philip Tinnefeld.

I greatly acknowledge the Scientific and Technological Research Council of Turkey and Bundesministerium für Bildung und Forschung for funding my PhD. I would like to thank Center for Nanoscience (CeNS) and Nanosystems Initiative Munich (NIM) for organizing helpful workshops and events. Your organizations helped me to develop myself and to meet a lot of new people. I additionally would like to thank Christoph (Criss) Hohmann for creating amazing cover image for my paper.

I would like to thank our secretaries Regina and Corinna for organizing everything smoothly and being there whenever I need a help. I would like to thank Tina Reuther for keeping the labs running.

I would like to thank my collaborators in University of Erlangen-Nuremberg, Bianka Puscher, Michael Weber and Dr. Ruben Costa for their efficient collaboration and patience about my questions. Thanks for opening your doors to me and hosting me in your lab and introducing LECs which became a big part of my thesis.

I gratefully acknowledge my collaborators in the University of Würzburg, Philipp Rieder, Dr. Andreas Baumann and Prof. Vladimir Dyakonov for their great support and fruitful collaboration. Thank you for introducing very interesting technique and making me think in a different aspect with your questions. Thanks for the fun times in the conferences!

I would like to thank my collaborators from the Technical University of Darmstadt, Dr. Michael Wussler and Prof. Wolfram Jaegermann for the UPS measurements. Thanks for the measurements and your patience about my endless questions about UPS. Thanks for the fun time in ABXPV conference in Valencia.

I would like to thank my collaborators, Dr. Yu Tong and Prof. Alexander Urban from LMU Physics department for their support during my PLQY measurements in their lab.

I would like to thank my collaborators in ZSW Stuttgart Dr. Erik Ahlswede and Moritz Schultes. Erik, thanks for organizing everything before my visits and helping us to measure super cool tandem solar cells. I always felt very-welcomed in ZSW. Moritz, I really don't know how to thank you. I really had a great time in my both visits. I will never forget our 'work hard party hard' times (13 hours of working and social events in the evening). Thanks for teaching me a lot of German phrases and making me meet a lot of people in one week! :) I hope I can pay back your help when you visit me in Turkey next year. Thanks for the 'vortrefflich' times in Stuttgart and don't forget 'Yemek buldun ye, dayak buldun kaç!'. :)

I would like to thank my in-house collaborators, Dr. Irene Grill and Prof. Achim Hartschuh. Irene, you are one of the most efficient people I have ever known. I really enjoyed working with you and thanks for helping me about German bureaucracy as well. Besides of our collaboration I always felt very welcomed in your office and had so much fun when I came to chat with you guys. Here, I have to thank Hartschuh boys, Alexander Biewald (the destroyer:) and Veit Giegold (Mr. Femtosecond:), as well for joining Irene and me. Guys, I will really miss your sense of humour and chats and thanks for the great time that we had in Venice!

I would like to thank whole AK Bein for the atmosphere that created in the group, particularly in the parties. I am very happy to know all of you. But I have to express my special thanks to Dr. Alexander Hufnagel and Sebastian Haeringer for introducing ALD and their support during SnO_x depositions. Thanks for organizing everything quite fast when I need the ALD. Especially you Alex, thanks for your patience during the optimization of the deposition.

I would like to thank my students Dominic Blätte and Andreas Weis for their great support in my projects. Andi, I am sorry that I left you in the lab and went for ice-cream, but I promise you that I will buy you ice-cream asap. :)

Now it comes to the hardest part, Perovskite Subgroup! I really don't know how I can say thank you guys. Thanks to Pablo, we all learned that we can work and enjoy at the same time. Thank you Yinghong (Hongi) Hu, Nadja Giesbrecht, Michiel Petrus, Maximilian (Ed) Sirtl, Andreas Binek, Fabian Hanusch, Enrico Greul for being there whenever I need a help! I enjoyed so much working with you guys in the same lab and I am a bit afraid that I won't have similar atmosphere in my future working places since you set the bar so high for me! Thanks for making my time in Germany unforgettable and fabulous.

But I have to thank specifically to Hongi, Nadja and Michiel. You guys were one of the reasons for me stay in this group and do my PhD in Germany. I learned that people around you are more important than anything else during PhD. I always felt lucky to have you as my colleagues/friends/my second family in Germany. I guess I can't express my gratitude here but thank you guys for being next to me all the time. You always enlightened me with your point of views to the situations! You guys always motivated me when I felt down or when I was so close to give up. Nadja and Hongi, thanks a lot for speaking English all the time in the office and helping for translations of German documents. :) I really enjoyed during the conferences with you. Michiel, you teached me to see the situations from different perspective. Nadja, I really appreciate your company during our coffee sessions (sometimes with delicious cupcakes:) and learned a lot of things about crystallization from you. Hongi, my twin sister, I will never forget our watermelon adventure during HOPV conference. Thanks for laughing so hard with me that we did annoy our office neighbors. :) There are so many memories that I want to mention but my acknowledgment is already too long but I will always remember them! :)

I also would like to thank Nespresso for keeping me awake and motivating me during my PhD with delicious coffee. Nadja, thanks for ordering and bringing my capsules! :)

Bilkent'te okuduğum için burnu havada biri olduğumu ve o yüzden mesajlarına cevap vermediğimi düşünen Begüm Bozkaya'ya tesekkür etmezsem olmaz. Almanya'daki ilk günümde yanimda olup yardımcı olduğun için ne söylesem az. Her şey için çok tesekkürler!

Lisans projemde tanıştığım ve bana araştirmayi ve birlikte çalışmanın muhteşem bir sey olduğunu gösteren Özlem Ünal'a teşekkür etmek istiyorum. Özlem, bana güvendiğin ve ne olursa olsun destek olduğun için ne söylesem az. Seni tanıdığım için çok şanslıyım ve dostluğun için çok teşekkür ederim!

Doktoranın getirdiği zorlukları birlikte göğüsledigimiz ve lisanstan sonra hep ayrı olsak da hala kontakta kalabildiğimiz (senin sayende) Damla İnan'a da teşekkür etmezsem olmaz. İhtiyacım olduğunda hep yanımda olduğun için çok teşekkür ederim. İnşallah senin doktora partinde ikimizin mezuniyetini de kutlayacağız!

Benimle birlikte kaç bayramı daha burada geçireceğimi sayan ve bana hep pozitif enerji veren taaaa ilkokuldan arkadaşım Merve (Merviş) Öztürk'e ne desem hiç bilmiyorum. Fiziken yanımda olmayıp ama hep yanımdaymış gibi hissettirdiğin için çok teşekkür ederim. Kötü hissettiğim zamanda atlayıp yanıma gelecek kadar koca yürekli olduğun için nasıl teşekkür etsem bilemiyorum. Senin gibi bir arkadaşım olduğu için hep çok şanslı hissettim!

Bu teşekkür etme işi gittikçe zorlaşıyor. Hele de benim gibi duygularını dışa vuramayan birisi için. Bu yüzden sana nasıl teşekkür edeceğimi hiç bilemiyorum Seda (Sedoş) Kavas. Bana her zaman destek olmakla kalmayıp saçmaladığım zamanlarda yolumu bulmama yardım ettiğin ve benim neyi sevdiğimi ya da sevmediğimi benden daha iyi bilen birisi olduğun için çok teşekkür ederim. O kadar çok anı var ki biriktirdiğimiz yazmaya başlarsam tezimden daha uzun olacak diye korkuyorum. :) Ama patlayana kadar abur cubur yemelerimizi, gezmelerimizi, kitaplar hakkında saatlerce konuşmalarımızı ve annenin yemeklerini asla unutmayacağım. Adeta beni de kendi kızı gibi gören ve neyi sevip neyi sevmediğimi bilip ona göre yemek hazırlayan Huri Teyze'ye de teşekkür etmezsem olmaz. Bir de tabi ki beni Esma (Esmoş) Arı ile tanıştırdığın için çok teşekkür ederim. Tabii ki de sana teşekkür etmeden geçmeyeceğim Esmoş. Benim göremedigim şeyleri benden önce tahmin ettiğin için ve saçmalıklarıma katlandığın için çok teşekkür ederim. Sedoş ile birlikte hep yanımda durduğunuz için size ne kadar teşekkür etsem az. Sizinle büyümek beni geliştirmekle kalmayıp hayata farklı açılardan da bakmayı öğretti. Her şey için çok teşekkür ederim!

Ve tabi ki son olarak beni her zaman sadece desteklemekle kalmayıp aramızdaki mesafelere rağmen her zaman yanımda olduklarını hissettiren annem Hatice, babam Rıfat ve ablam Melike Aygüler'e teşekkür etmek istiyorum. Benim için yaptığınız fedakarlıkları ödemem kesinlikle mümkün değil. Benim kendime inanmayı bıraktığım zamanlarda bile bana inanmaya devam ettiğiniz için ne diyeceğimi bilemiyorum. Annem, senin bütün ailemiz için yaptığın fedakarlıkları ödememiz mümkün değil. Babam, beni burada tek bir gün desteksiz bırakmadığın için çok teşekkur ederim. Ve son olarak canım ablam, hep örnek aldığım insan, sana da ne desem az. Kaç insanın kardeşi kötü hissettiği için aynı gün içinde uçağa atlayıp gelecek kadar çılgın bir ablası vardır ki?! :) Her şey için çok teşekkur ederim. Sizi çok seviyorum!

Every great and deep difficulty bears in itself its own solution. It forces us to change our thinking in order to find it.

Niels Bohr

Abstract

Semiconductors have had a monumental impact on our society, being at the heart of every electronic device in our daily lives. Undoubtedly, they have changed the world beyond anything that could have been imagined before them. Otherwise, we would be using computers like a monster of a machine, weighing more than 30 tons and consuming several kilowatts of electrical power that when it is turned on, the lights in a few cities would be dimmed.

Among all other semiconductor materials, so-called *hybrid organic-inorganic perovskites* have drawn a great deal of attention in the last decade due to dramatic strides in power conversion efficiencies (PCEs) as photoabsorbers in solar cells. Their similarities to gold standards of crystalline silicon have carried them to be some of the most intensely researched semiconductors by producing a plethora of optoelectronic devices. However, despite their versatility, there are several hurdles, holding their further improvement back. In this thesis, intrinsic properties of this family of materials and their limitations are profoundly investigated and solutions are provided for further developments.

In the first part of this thesis, a performance difference in the current-voltage scans of solar cells, so-called *anomalous hysteresis*, is unveiled. This phenomenon emerges from a combination of ion migration and charge recombination at the charge transport layer-perovskite interface and hampers the device performance severely. It is found that deep trap states at the interface likely trigger charge accumulation due to the Fermi level offset of SnO_x from the perovskite, which in turn leads to enhanced charge recombination, causing a higher degree of hysteresis in solar cells. It is suggested that if the band alignment between the perovskite absorber and the SnO_x layer is improved, the resulting device excels due to greatly reduced hysteresis and much better performance.

Charge transport characteristics and their limiting factors are of utmost importance in photovoltaic devices in order to extract the charges efficiently. The charge carrier mobilities in $CH_3NH_3PbI_3$ thin films extracted from lateral time-of-flight measurements are found to be 6 cm^2/Vs, whereas similar measurements performed on a solar cell architecture, i.e. in the vertical direction, show effective mobilities that are reduced by 3 orders of magnitude. By varying the thickness of the charge extraction layers, it is revealed that the limiting factors of the charge carrier transport time in working devices are the electron and hole transport layers rather than the perovskite material itself.

In chapters 5 and 6, the versatility of perovskite semiconductors was extended by synthesizing both hybrid and all-inorganic perovskite nanocrystals (NCs) with compositional engineering. It is found that exchanging cation and mixing halide ions in the perovskite structure not only altered their charge recombination rates as well as photoluminescence spectra but also the photoluminescence quantum yield (PLQY). The implementation of mixed halide systems into lighting devices, so-called light-emitting

electrochemical cells (LECs), revealed another major intrinsic concern of perovskites: *halide segregation*, forming bromide- and iodide-rich phases upon application of voltage in the devices. However, this problem was tackled by adding the salt KCF_3SO_3 in the active layer of LECs with mixed halide NCs. This addition not only suppresses the halide segregation by further stabilization of the perovskite lattice with potassium ions but also improves the brightness of the devices with low injection voltage.

In the last part of thesis, four-terminal *perovskite/CIGS tandem solar cells* were presented. In order to boost the efficiency of the CIGS bottom-cell in tandem configuration, the transparency of the top-cell is of paramount importance. Thus, wide-band perovskite top-cells with different transparent conductive oxides used for both substrates and back electrodes were investigated, revealing that the transparency of the substrate is more critical than the back electrode's transmittance to increase the performance of CIGS solar cells. Additionally, the reason of low voltage output in the top-cell is attributed to the halide segregation caused by application of voltage and illumination, where the formation of bromide- and iodide-rich phases was demonstrated by X-ray diffraction measurements. Finally, methods to improve the performance of perovskite top-cells were suggested as an outlook.

Table of Contents

List of Abbreviations

2-T	2-terminal
4-T	4-terminal
A	Absorbance
a_B	exciton Bohr radius
AFM	Atomic Force Microscope
ALD	Atomic Layer Deposition
BE	Back electrode
BSE	Back-scattered electrons
CB	Conduction band
CBM	Conduction band minimum
CCD	Charge-coupled device
CIGS	Copper indium gallium selenide
CRT	Cathode ray tube
E_F	Fermi level energy
E_g	Band gap
E_V	Vacuum level energy
EL	Electroluminescence
ENIAC	Electronic Numerical Integrator and Computer
EQE	External quantum efficiency
ETL	Electron transport layer
ETM	Electron transporting material
FA	Formadinium
FDC	Fast deposition cystallization

FF	Fill factor
FS	Forward scan
FTO	Fluorine-doped tin oxide
FWHM	Full width at half maximum
HI	Hysteresis index
HOIP	Hybrid organic-inorganic perovskite
HTL	Hole transport layer
HTM	Hole transporting material
IC	Integrated circuit
IO:H	Hydrogenated indium oxide
ITO	Indium tin-oxide
IZO	Indium-doped zinc oxide
J_{sc}	Short-circuit current
J-V	Current-voltage
LEC	Light-emitting electrochemical cell
LED	Light-emitting diode
LIV	Luminance-current vs. applied voltage
MA	Methylammonium
MAPI	Methylammonium lead iodide
MPP	Maximum power point
NC	Nanocrystal
NP	Nanoparticle
OA	Oleic acid
OLA	Oleylamine
OLED	Organic light-emitting diodes
PCE	Power conversion efficiency

PL	Photoluminescence
PLQY	Photoluminescence quantum yield
PMMA	poly(methyl methacrylate)
PSC	Perovskite solar cell
PXRD	Powder X-ray diffraction
RS	Reverse scan
QD	Quantum dot
R	Reflection
RMS	Root-mean-square
SAM	Self-assembled monolayer
S-Q	Schockley-Queisser
SE	Secondary electrons
SEE	Secondary electron edge
SEM	Scanning Electron Microscopy
Si	Silicon
T	Transmission
TCO	Transparent conductive oxide
TCSPC	Time-Correlated Single Photon Counting
TEM	Transmission Electron Microscopy
TMPE	Trimethylolpropane ethoxylate
ToF	Time of Flight
TSC	Thermally Stimulated Current
UPS	Ultraviolet Photoelectron Spectroscopy
UV-Vis	Ultraviolet-Visible
VB	Valence band
VBM	Valence band maximum

V_{oc}	Open-circuit voltage
XRD	X-Ray Diffraction

1 Introduction

1.1 Semiconductors

In 1931, Wolfgang Pauli, later a Nobel Laureate, was asked to express an opinion on semiconductors and he responded: "*One should not work on semiconductors, that is a filthy mess; who knows whether any semiconductor exists"*. Following that comment, who could have predicted that the present period will be called *"semiconductor age"*? In the modern world, semiconductors are ubiquituos, one would be hard-pressed to find an electronic device without semiconductor materials involved in its operation. Thus, semiconductors not only have enabled the building of the modern information society but have also revolutionized mankind's lifestyle at least as profoundly as the invention of steam engines and steel.[1]

The birth of semiconductors with the invention of the rectifier (AC-DC converter) in 1874[2] was followed by the first working prototype transistor, invented at Bell labs in 1947. A year later, the invention of the junction transistor heralded the arrival of the transistor era.[3] If one could imagine that the transistors were not discovered, mankind would still be using huge computers consisting of numerous vacuum tubes, occupying an entire building, similar to the first computer (Figure 1.1). This system would consume a huge amount of electricity as well as produce a lot of heat and would not generally be available to the public.[4-5]

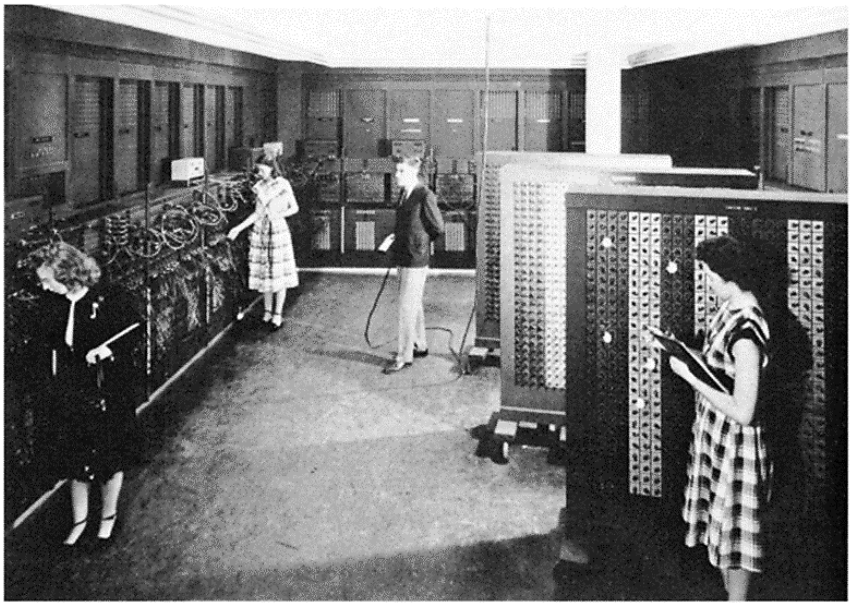

Figure 1.1 The first computer, Electronic Numerical Integrator and Computer (ENIAC).[4]

The semiconductor industry developed dramatically with the commercial production of the transistor and related devices. They proved to be smaller, lighter, more reliable and less expensive to build (Figure 1.2). Furthermore, the last few decades have witnessed the rapid expansion of the integrated circuit (IC) where several transistors are combined in a single device. Nowadays the number of transistors in these circuits has reached billions and this extreme density has opened the way to several applications such as cell phones, GPS devices, laptop computers and tablets.[6]

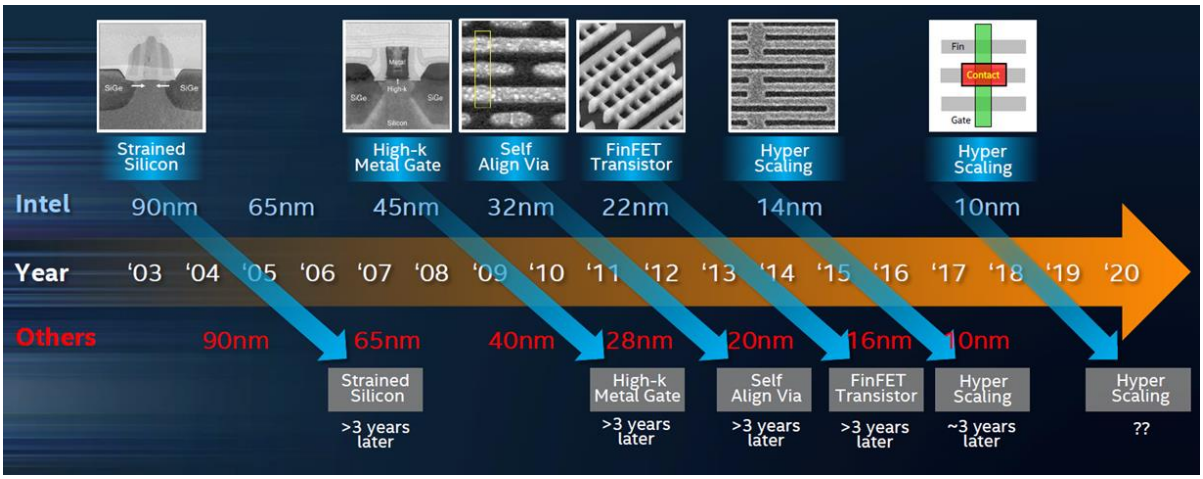

Figure 1.2 Intel leads the industry by at least 3 years in introducing major process innovations.[7]

1.1.1 What Makes Semiconductors Useful?

Semiconductors are the foundation of modern day electronics such as radio, computers and mobile phones. The reason why they are in the center of our lives is their unique atomic structure that allows their properties to be tuned.[8]

1.1.1.1 Energy Bands in Semiconductors

The electronic configuration of bulk materials such as conductors, semiconductors and insulators is described by *band theory*. Electrons in an isolated atom can only have discrete energy levels as shown in Figure 1.3A. However, these degenerate energy levels split into many seperated levels due to the atomic interaction in case of crystalline solids where atoms are brought together. These levels are treated as a continuous bands of allowed energy states since the levels are so closely packed together. The highest occupied and the lowest unoccupied energy bands are called *valence (VB) and conduction band (CB)*. These bands are separated by a region which designates energies that the electrons in the solid cannot possess. Therefore, this region is called the forbidden gap, or *band gap* (E_g) which is the energy difference between the maximum valence band energy and the minimum conduction band energy.[6, 9]

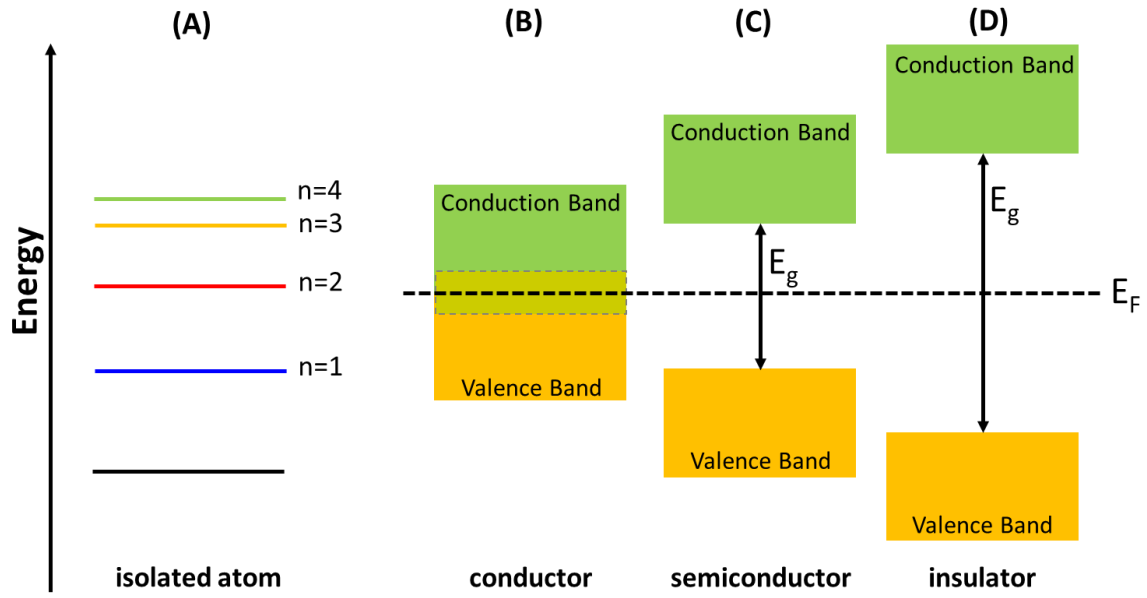

Figure 1.3 A relative representation of the energy bands for (A) discrete energy levels of isolated atom, (B) conductor, (C) semiconductor and (D) insulator. The marked dashed area is the overlapping of valence and conduction bands.

An important parameter in band theory is the Fermi level, named after physicist Enrico Fermi. The Fermi level is the energy level in a material at which there is a 50% probability that it is filled with electrons. In other words, levels below this value tend to be filled with electrons whereas the levels above tend to be empty. If the Fermi level of the material lies within a band, it is called a *conductor*. On the other hand, if the Fermi level lies between two widely separated bands, the material will be an *insulator*. If the Fermi level is between relatively close bands, the material is a *semiconductor*.[6] Figure 1.3 shows the schematic representation of the energy bands in these materials.

The large energy gap in insulators means that no electrons can reach the CB at ordinary temperatures whereas conductors do not possess a band gap since the valence and conduction bands overlap as shown in Figure 1.3B (marked with dashed rectangular area). In contrast to these two concepts, in semiconductors, the band gap is small enough that thermal energy can bridge the gap for a small fraction of electrons, providing the semiconductor limited conductivity. With such a small gap, the presence of a small percentage of a doping material can increase conductivity dramatically.[8]

1.1.1.2 Bands for Doped Semiconductors

Pure semicondutors, such as a Si crystal without any impurities, are named *intrinsic* semiconductors (Figure 1.4A). They are neither good conductors nor insulators and their conduction is largely dependent on temperature. However, the properties of the material can be modified by introducing foreign substances or impurities into the crystal, known as *dopants*. The semiconductor with an added dopant is

called *extrinsic* semiconductor. Some atoms in the lattice are replaced with the dopant atoms, altering the lattice structure and introducing extra energy levels. There are two different types of extrinsic semiconductors according to the doping of the material: *n-type* and *p-type* semiconductors.

In n-type band structure, the addition of donor impurities introduces electron energy levels high in the semiconductor band gap so that electrons can be easily excited into the CB. These donor electrons become free ionized electrons and leave behind ionized holes. The extra electrons add to the number of filled energy states and the Fermi level is pushed to a higher value, away from the VB and closer to the CB. This is shown in Figure 1.4A. Due to a significantly larger number of free electrons than the number of holes in n-type semiconductors, electrons in n-type materials are called the majority charge carriers for current flow while holes are the minority charge carrier.[10]

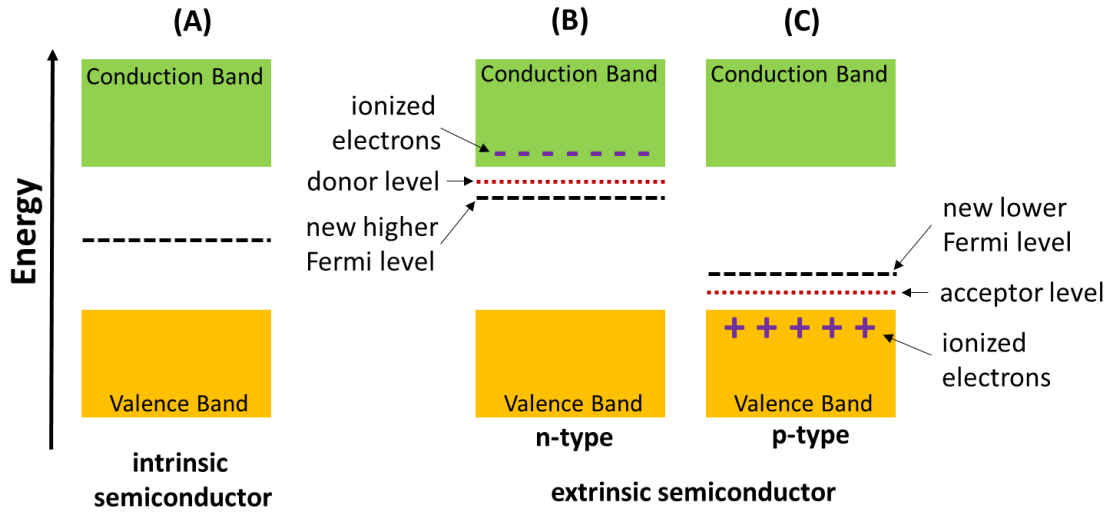

Figure 1.4 Energy band diagram of (A) intrinsic semiconductor, (B) n-type and (C) p-type extrinsic semiconductor.

In a p-type band structure, the addition of acceptor impurities lowers the hole level in the semiconductor band gap so that electrons can be easily excited from the VB, leaving mobile holes in the VB. The resulting situation is essentially the reverse of that of the n-type material, pushing the Fermi level down, closer to the VB. Figure 1.4B shows the energy band diagram for a p-type material. In p-type materials, the number of holes is dominant and the majority charge carriers are holes whereas electrons are the minority carriers.[6, 10]

1.1.1.3 Quantum Confinement of Semiconductors

As described by Moore's law, the semiconductor industry continues to make ever smaller transistors. This pushed the size of the materials to the smallest limits, where the size of the transistors recently became only a few nanometers wide.[11] Besides this, novel properties arise when the dimensions of a

semiconductor material reach the nanoscale, opening up a fascinating class of materials:[12] *semiconductor nanocrystals (NCs)*; which are crystalline particles, exhibiting size-dependent optical and electronic properties. These NCs display discrete electronic transitions (Figure 1.5) as well as useful properties of crystalline materials, while their bulk counterparts are characterized by composition-dependent E_g. With the absorption of a photon with energy greater than E_g, the excitation of an electron leaves an obital *hole* in the VB. The lowest energy state of a negatively charged electron and positively charged hole is an electrostatically bound electron-hole pair, known as an *exciton*.[13]

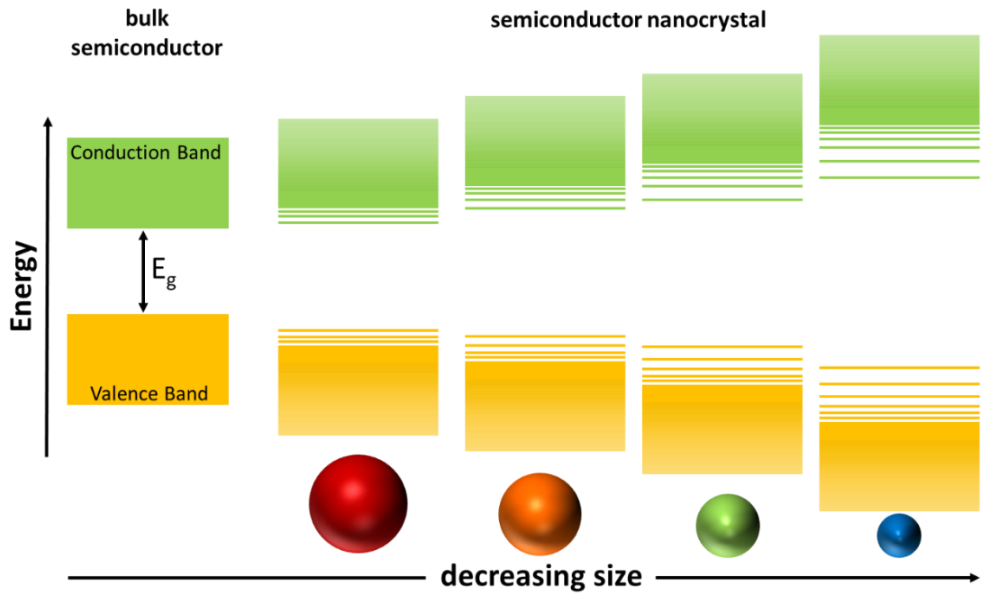

Figure 1.5 Schematic representation of quantum confinement effects: band gap increases and discrete energy levels appear at the band-edges with decreasing NC size.

When particle dimensions range in the nm scale, the size of the exciton, known as the exciton Bohr radius (a_B), becomes comparable to the size of semiconductor NC (r). If r is smaller than a_B, the charge carriers become spatially confined, which raises their energy. Thus, the exciton size determines the transition between the regime of bulk crystal properties and the *quantum confinement* region, in which the optical and electronic properties are dependent on the NC size.[13-16] The most striking consequence of the quantum confinement effect is the band gap tunability of nanocrystalline semiconductors, where the energy gap increases, leading to a blue shift of emission wavelength as the size decreases.[13-14, 17-18] Therefore, the whole visible spectrum from blue to red can be covered with semiconductor NCs by varying their size rather than their composition.[13-14]

The degree of the quantum confinement may be different in different directions of the NC, depending on its size and shape. If the exciton is spatially confined in all directions, a *quantum dot* (QD) is obtained, whereas NCs in which the exciton is confined only in the diameter direction are called *quantum wires*.

If the confinement is in the thickness direction only, this results in a *quantum well* (Figure 1.6). An increase in the number of dimensions yields a stronger degree of electronic confinement and thus a wider range of tunability in the band gap. This makes the optoelectronic properties of semiconductor NCs also profoundly shape-dependent.[13, 19]

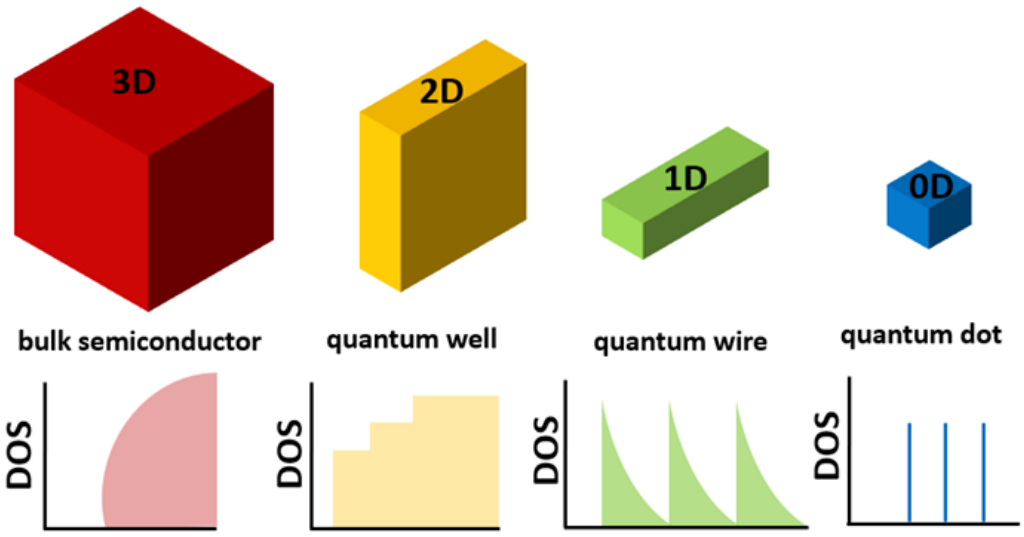

Figure 1.6 Schematic illustration of the energy level structure of a bulk semiconductor and semiconductor nanostructures with reduced dimensionality. DOS represents the density of electronic states.

1.1.2 What Are Semiconductors Used for?

The versatility of the properties of semiconductor materials open the doors towards numerous technological achievements. There are several applications of semiconductor devices that have become the backbone of today's technology. The smart phones or the computers which have millions of tiny transistors made from this material, power supplies, automobiles and amplifiers are only some of the technologies in our daily life. One of the principal uses of semiconductors in a wide range of electronic and optoelectronic devices is related to their capability to form various electrical junctions and resulting electrostatic inhomogeneities and built-in electric fields.[20] However, in this thesis, the *optoelectronic applications* of such materials will be focused on.

Optoelectronics is a technology, bringing optics and electronics together within a single device and a single material. Thus, the material needs to allow for manipulation of light and electrical current as well as their interaction. Semiconductors provide all the requirements since they can carry both electrical current and light waves, and even better they can transform light into current or vice versa.[21] Therefore, they are used in many optoelectronic applications, including solar cells[22-23], lighting technologies such

as light-emitting diodes[24-25], light-emitting electrochemical cells[26-28], lasers[25, 29], and photodetectors[30-31]. Among all applications, solar cells and lighting devices will be investigated throughout this thesis.

1.1.2.1 Solar Cells

The first practical use of solar cells, powering instruments on board of the Vanguard I satellite, was launched in 1958. Although the major driving force for the development of solar cells was initially related to space applications, the expected decrease of fossil fuel sources coupled with environmental concerns, such as CO_2 emission and other greenhouse gases into the atmosphere, has shifted the main goal towards terrestrial applications. Therefore, the use of the most abundant permanent energy source, *solar radiation*, has become inevitable, where the solar energy reaching the Earth's surface provides far more than the global energy demand.[32-34]

The operation of solar cells is based on the photovoltaic effect, which is the direct conversion of incident light into electricity by a p-n or p-i-n junction semiconductor device. In the first step, photons with higher energies than the band gap of the semiconductor are absorbed to generate electron-hole pairs.[32] In a fully assembled solar cell, interfaces are used to extract the photoexcited electrons out of the device. In a classical juntion device, charge seperation occurs at a junction between an n-doped material (high electron conductivity) and a p-doped material (high hole conductivity), as photogenerated charges move into the two materials defining the junction (Figure 1.7A). Following the formation of the p-n junction, electrons from the n-doped side diffuse towards the p-doped side and vice-versa. These electrons and holes recombine in the center of the solar cell, creating a depletion region where no mobile charges are present. The diffusion of electrons from the n-doped side leads to the formation of the positively charged part, whereas the p-doped side becomes negatively charged. This charge difference creates a built-in field and there are no mobile charges left in the junction area.[35] In principle, the dark characteristics of the diode and the photogenerated current can be linearly superimposed, resulting in the current-voltage (*J-V*) curve at the output of a solar cell as shown in Figure 1.7B (also described by the solar cell equivalent circuit).[36]

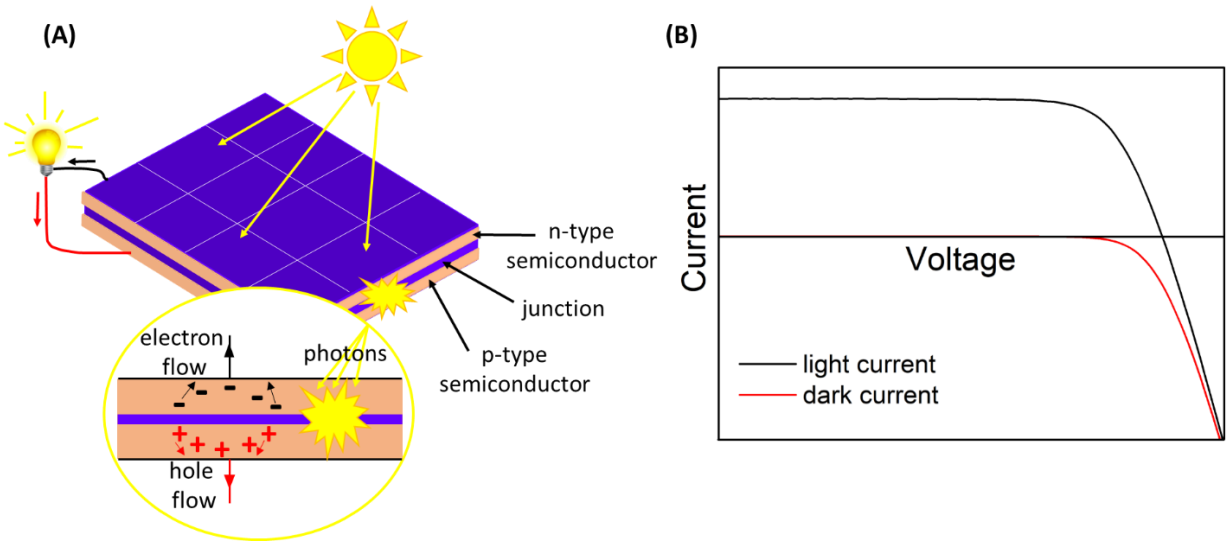

Figure 1.7 (A) Solar cell working principle. (B) Typical *J*-*V* characteristics of a solar cell.

The power conversion efficiency of single-junction solar cells is governed by the thermodynamical Shockley-Queisser (S-Q) limit of ~31%, meaning that an ideal solar cell converts approximately 30% of the solar radiation into electrical power under direct sunlight due to the below-band gap absorption loss and the thermal-relaxation loss of hot charge carriers.[32] A way to improve this performance beyond the S-Q limit would be to integrate wide-band gap (1.7-1.85 eV) top solar cells with low-band gap bottom solar cells (~1.1 eV).[36-37] These tandem configurations allow the high-energy photons to be absorbed in the top-cell, generating high voltage to reduce the thermalization loss and allow the bottom-cell to absorb the transmitted low-energy photons, which leads to a more efficient harvesting of the solar spectrum.[37]

1.1.2.2 Light-Emitting Electrochemical Cells (LECs)

The light-emitting electrochemical cell (LEC) is a thin-flim and area-emitting device that has been deposited onto a broad range of surfaces such as plastic[38], paper[39], textile[40] and metal[41] as shown in Figure 1.8. LECs, featuring a single-layer active material sandwiched between two air-stable electrodes, can be fabricated from environmentally friendly raw materials with low-cost and scalable solution-based methods. These devices can also cover the whole visible spectrum as dictated by the band gap of the semiconductor in the active layer. These benefits separate the LEC from commercially introduced emission technologies such as the light-emitting diode (LED), the organic LED (OLED) and light-emitting capacitor, promising the emergence of important and paradigm-shifting emissive applications such as point-of-care diagnostic and treatment devices, emissive and conformable fabrics and low-cost and low-voltage illumination panels.[42-43]

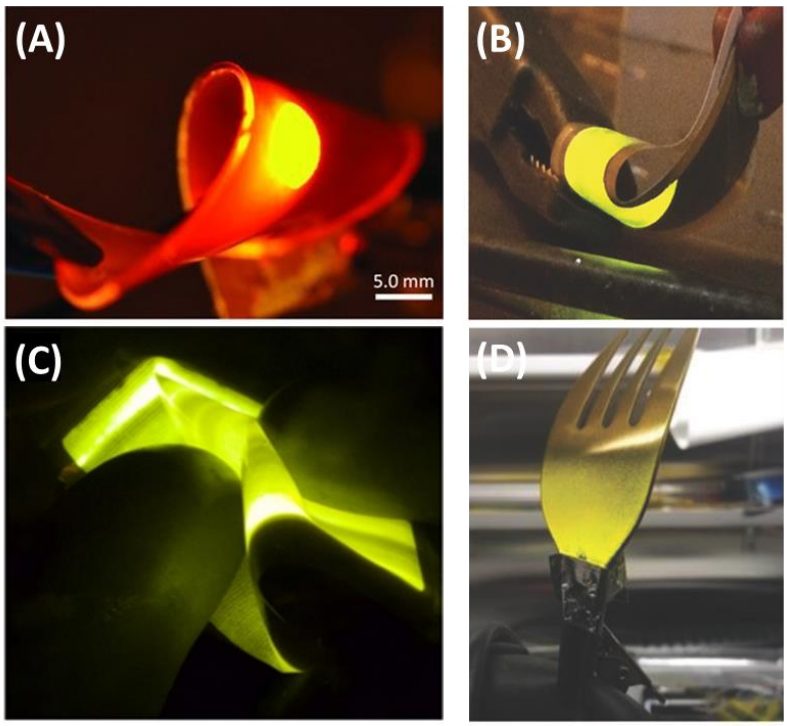

Figure 1.8 (A) Twisted stretchable LECs.[38] (B) Bent specialty-paper LECs.[39] (C) Ultra-flexible and light-weight LEC textile during severe deformation between two fingers.[40] (D) A light emitting fork, as realized by spray-sintering a stainless-steel fork with an active layer and a top cathode.[41]

The versatility of this technology is highlighted by the application of a wide range of materials such as luminescent polymers[44], phosphorescent ionic transition metal complexes[45], quantum dots[28, 46-47] and small molecules[48]. The latter are blended with either ionic liquids or ionic polyelectrolytes that provide the necessary amount of mobile anions to assist both charge injection and transport processes upon applying a voltage over time.[49]

A characteristic feature of the LEC is the presence of mobile ions in the active layer, enabling the in-situ formation of a p-i-n junction that is self-assembled through electrochemical doping during operation.[26, 50-51] Furthermore, this dynamic doping mode not only is advantageous for large and balanced electron and hole currents but also a high recombination rate of electrons and holes into excitons. Even though this brings a challenge since the exciton will be quenched when it impinges upon an electron or a hole, resulting a severe quenching in LEC devices, this problem can be solved using host-guest approaches in the active layer.[42]

1.2 The Emergence of Perovskites

Perovskite semiconductors have opened a new era for low-cost and high-efficiency solar cells and have spread the so-called *perovskite fever* all around the world in the last decade.[52] Thanks to the tremendous research efforts, they have already reached photovoltaic efficiencies exceeding 22%[53], which is also the highest-performing solution-processed solar cell on record. It is noteworthy to mention that such a growth of the power conversion efficiency (PCE) has actually taken decades for other photovoltaic solar cells to accomplish as shown in Figure 1.9.[54] This unexpected breakthrough and rapid evolution of this family of materials have energized not only the photovoltaic community but also the efforts of other optoelectric communities dealing with devices such as photodetectors[55], field transistors[56], resisitive memory devices[57] and lighting devices[58-59] to create devices from these constituents, *e.g.*, methylammonium lead halide ($CH_3NH_3PbX_3$, X = Cl, Br, I) and its analogs.[60]

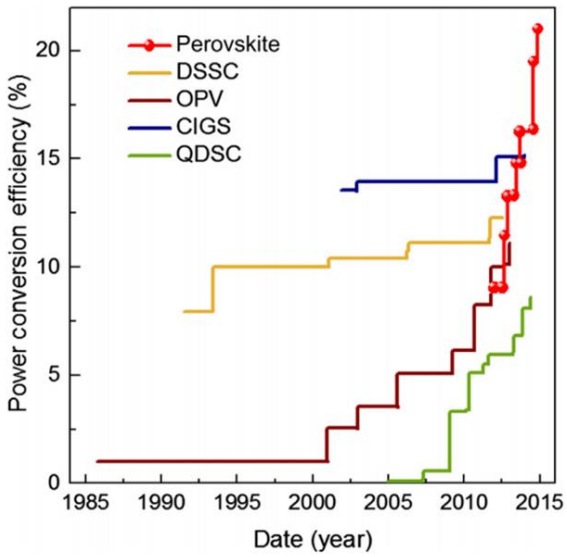

Figure 1.9 Perovskite solar cells have increased in PCE at a phenomenal rate compared to other types of photovoltaics.[61]

A major feature of perovskites that has brought this success is the similarity to the gold standards of crystalline silicon and GaAs semiconductors, including a sharp band gap close to the ideal value, high absorbance, crystalline film formation with low defect densities, balanced electron-hole transport and excellent charge carrier mobilities.[37, 61] Furthermore, the materials are inexpensive and earth-abundant and they can be recovered from other industrial materials and products.[62] Other distinct advantages of these materials are the easy fabrication on various substrates without the need for lattice matching (unlike III-V semiconductors which need lattice and thermal-expansion-coefficient match with the substrates) thanks to their softness and defect-tolerance as well as their deposition by low-temperature processes such as spin-coating, doctor-blading, slot-die coating, dip-coating and thermal evaporation.

These features make them also suitable candidates as top cell semiconductors in tandem applications.[37] Moreover, the band gap of perovskites can be tuned by both compositional engineering and quantum confinement effect as seen in Figure 1.10.[59, 63-64]

Figure 1.10 Photographs of the perovskite films with increasing band gap from right to left with compositional engineering.[65]

Before their recent exploration in optoelectronics, they have been studied extensively in crystalline families of hybrids.[66-67] The archetypal perovskite has a formula of ABX_3, where A is a monovalent cation, B is a divalent metal cation and X is a halide anion. The B cations are coordinated with X anions forming octahedrons that are connected with each other as shown in Figure 1.11. The A site cations have two functions: (i) filling the void generated between the connected octahedra and (ii) neutralization of the charge of the octahedron networks.[68-72] There are two major classes of these perovskites depending on the monovalent cation. One is the inorganic perovskite in which an inorganic cation is used and all the bonded atoms are inorganic. The replacement of the inorganic A-site cation by an organic cation leads to the formation of hybrid organic-inorganic perovskites (HOIP).[68] The most commonly used A-site cations in these perovskites are methylammonium (MA, $CH_3NH_3^+$) and formamidinium (FA, $CH(NH_2)_2^+$) as organic sources[59, 73] whereas cesium (Cs^+) and recently introduced rubidium (Rb^+) cations are utilized as inorganic constituents[74-75]. Regarding the B-metal cation, the most widely investigated are lead (Pb^{2+}) and tin (Sn^{2+}). Lastly, X-site anions can be chloride (Cl^-), bromide (Br^-) and iodide (I^-).[76]

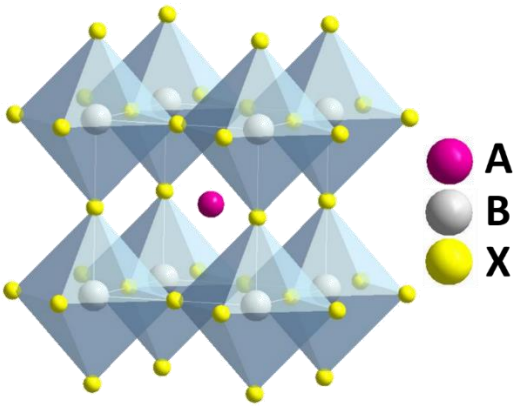

Figure 1.11 Single unit cell of an ABX_3 halide perovskite crystal, where A is an organic cation, B is a divalent metal and X is a halide anion.

1.2.1 Perovskite Nanostructures

Rather low energy barriers have to overcome to form organic-inorganic hybrid perovskite structures from approproate reactants, thus obtaining a crystalline phase by merely mixing and grinding the precursor salts at room temperature. Typically, halide perovskites are synthesized by wet-chemistry routes which enable mixing at the molecular level and result in materials with high phase purity.[25] By carefully controlling the reaction conditions, such as temperature, solvent and ligands, their morphology (from 3D to 0D) and size (from mm to nm range) can be easily modified as shown in Figure 1.12.[71, 77-80] Due to the ease of preparation of a wide variety of nanostructured perovskites and presence of outstanding properties at the nm scale, the nano-structuring of such materials has become widely studied in a short time.[25]

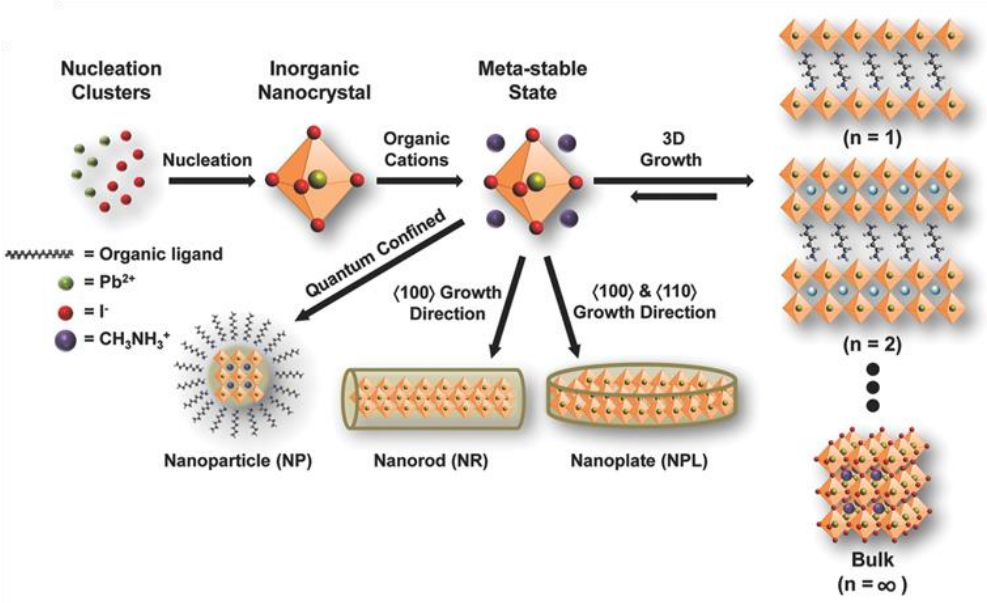

Figure 1.12 Schematic representation of the perovskites with different morphologies.[25]

Perovskite nanocrystals (NCs) show a considerably higher photoluminescence quantum yield (PLQY) without any surface passivation than their bulk counterparts due to quantum confinement leading to an increase in exciton binding energy that results in an enhancement of the radiative recombination.[25, 59, 63, 81] The high PLQY combined with the compositional flexibility of these semiconductors position these perovskites as robust technological candidates, distinguished by: (i) high color purity with emission full width at half maximum (FWHM) of around 20 nm;[46, 63] (ii) band gap tunability to cover the whole spectrum of visible light[82] as shown in Figure 1.13A and B and (iii) low-to-moderate ionization energy to form stable functional interfaces[83]. All these attractive features of perovskite nanostructures make them applicable for light-emitting diodes[78, 84] as well as in lasing applications and photodetectors.[29, 85]

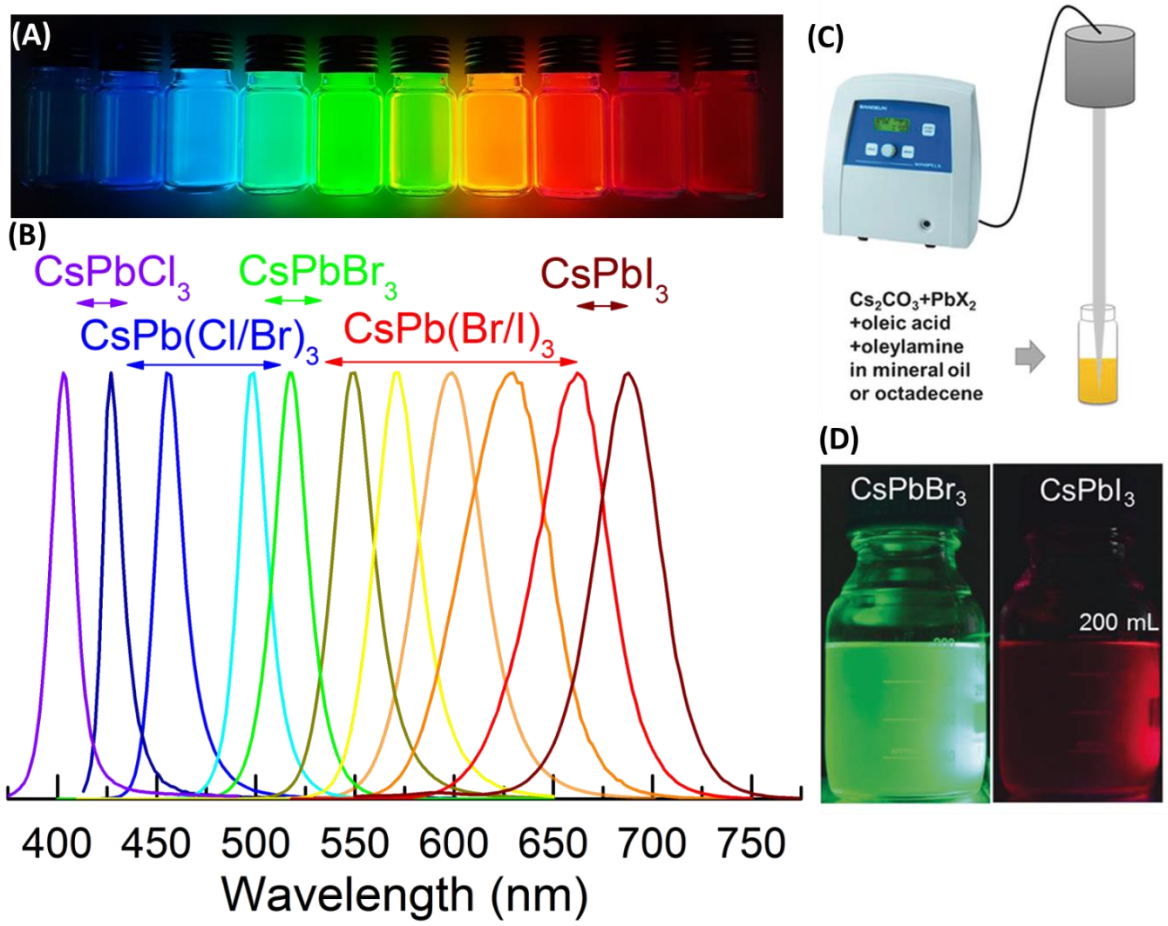

Figure 1.13 (A) Colloidal $CsPbX_3$ NCs synthesized by a hot-injection method observed under UV light (λ = 366 nm). (B) Perovskite NCs with tunable band gap energies covering the entire visible spectrum. (C) Synthesis of $CsPbX_3$ NCs through single-step tip sonication.[86] (D) Scalable synthesis of NCs. Photograph of $CsPbBr_3$ and $CsPbI_3$ colloidal dispersions under UV light.[86]

Perovskite NCs can be synthesized by various methods such as recrystallization in an antisolvent and by the hot injection method.[87] The former is predominantly used for the synthesis of HOIP NCs at low temperatures (<80 °C). In this method, polar solvents, in which lead salts and ammonium halide salts are soluble, are injected into a nonpolar poor solvent in the presence of coordinating ligands to stabilize the particles.[71] On the contrary, inorganic perovskite NCs are prepared by a hot-injection method where a cesium precursor is swiftly injected into a flask containing PbX_2 in non-coordinating solvents with ligands at temperatures ranging from 140-200 °C under inert atmosphere.[63] In addition to these routes, a polar-solvent-free and single-step approach for the large-scale synthesis of inorganic perovskite NCs is realized by direct ultrasonication of corresponding precursors in the presence of organic ligands under ambient conditions (Figure 1.13C and D).[86]

1.2.2 Challenges of Halide Perovskites

Although the PCE of perovskite solar cells has gone from single digits to over 22% in a few years' research, they still face challenges that prevent them from competing with established technologies.[23, 88] Therefore, at this stage of their development, the key issues are how to achieve further improvements in efficiency and long-term stability of these materials under device operation. The advancements in materials processing in the past couple of years have led the research community to profoundly investigate intirinsic vs. extrinsic degradation mechanisms.[23]

The stability issue is a major hurdle for the commercialization of perovskite optoelectronics.[64, 89] The degradation factors of perovskites can be divided into two: (i) extrinsic environmental and (ii) intrinsic degradation factors. Before investigating the intrinsic ones in detail in the next chapter, it is important to understand the extrinsic environmental degradation factors that increase degradation pathways, which tend to be irreversible.[23] First, ultraviolet (UV) light, present in the full solar spectrum, is detrimental to the long-term stability of perovskites due to the absorption by the electron-selective contact, initiating a chemical degradation.[90] Second, analogous to organic PV, perovskites are severely affected by moisture which induces rapid degradation of the perovskite layer in the devices.[91-92] In addition to these factors, elevated temperature[93] and oxygen[94] are also responsible for the instability of the perovskites. These extrinsic factors can be retarded using the sealing technologies industrialised for organic electronics, enabling oxygen and humidity barriers and protection against UV light.[95]

1.3 Stability of Perovskites : Intrinsic Degradation Factors

The performance losses still occur even when ruling out any of the external sources of degradation that have been discussed above. This is simply due to their intrinsic properties such as migration of ionic defects within the organic-inorganic perovskite lattice.[95] Halide anion (X) vacancies have been calculated to show the lowest formation energies[96], with Br^- ones being favored over I^-[97]. Two common phenomena caused by these movements are so-called hysteresis and halide segregation in mixed halide systems.

1.3.1 Hysteresis

One typical charasteristic of perovskite solar cells (PSCs) is the presence of *anomalous hysteresis* in the *J-V* measurement under light illumination. This is defined as change in the measured *J-V* curves upon switching the scanning direction and rate; and the illumination conditions before the measurement as shown in Figure 1.14.[64, 88, 98] This anomalous hysteresis is one of the main drawbacks of PSCs, slowing their development since it impairs the accurate determination of a steady state device efficiency, where cells with a pronounced hysteresis show a larger loss in performance than those with a lower hysteresis.

It is important to keep in mind that only the steady-state values under continuous illumination have practical significance and should take precedence over simple *J-V* curve scans.[64, 98-99]

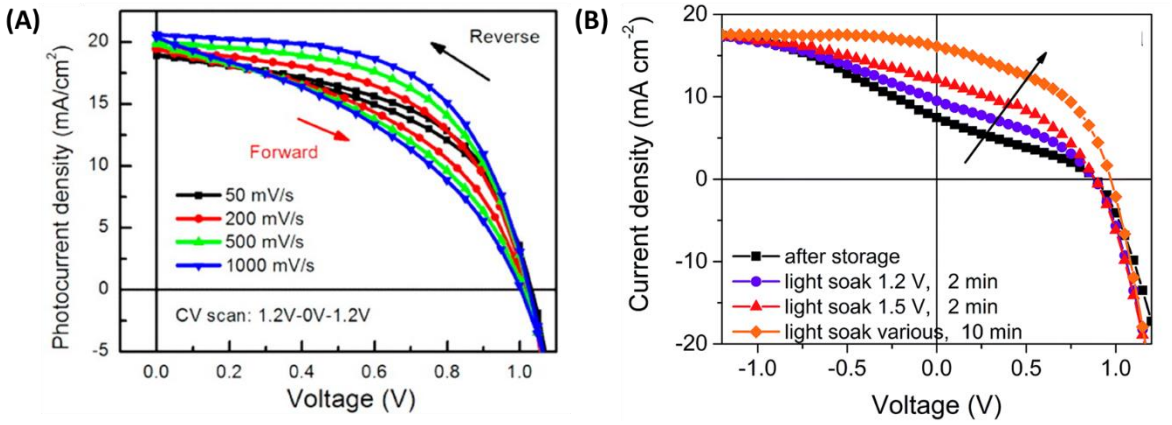

Figure 1.14 *J-V* response of PSCs at different (A) scan rates[100] and (B) light-soaking conditions[101].

There are several suggested mechanism for understanding the origin of hysteresis.[102-103] The leading model among them is ion migration associated with a change in interfacial fields and barriers resulting from accumulation of ions at interfaces, which causes charge recombination.[104-105] In the presence of an electric field created by an external voltage bias or light, ions migrate across the bulk of the perovskite layer and reach the external interfaces where they accumulate. The charge collection efficiency of the device is adversely affected where these interfaces act as recombination regions. Instead, if recombination at the interfaces is reduced, then the build-up of photogenerated charge carriers contirbutes to efficient collection of diffusive currents during the forward scan. Therefore, low hysteresis is resulted from the combination of low interfacial recombination and resultant high photogenerated carrier populations at forward bias, despite the presence of ion migration. This model also explains the reduction in hysteresis when the contact materials are changed, while this is unlikely to significantly influence the behaviour of mobile ionic charges within the perovskite phase.[104]

Based on this model, the degree of hysteresis is highly dependent on the interface properties and choice of contact materials, which appear to control the interfacial trap density as shown in Figure 1.15.[99, 103-104, 106-107] To suppress the hysteresis, the traps can be passivated by modifying the interface with fullerene derivatives to reduce the nonradiative recombination channels due to the reduction in the trap density at this interface.[106] Additionally, the hysteresis can be alleviated by the fine-tuning of the Fermi level of the contact material and the perovskite. With this, the charge transport is promoted through the contacts, which ultimately decreases the hysteresis, instead of accumulation and recombination of the charges at the interface.[99] However, the hysteresis of PSCs is still under lively debate and no effective methodology has been discovered yet despite much effort to better understand the origin and minimization of the hysteresis.[102]

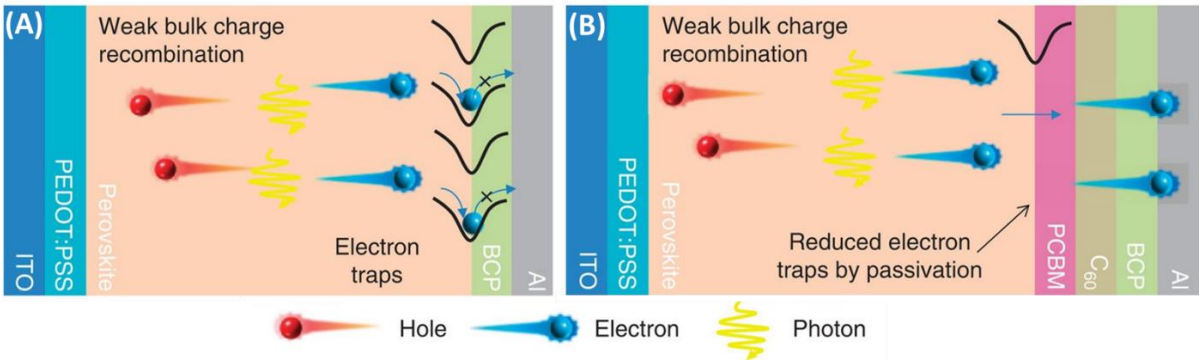

Figure 1.15 Schematic representation of the surface recombination reduction by passivating the trap states.[106]

1.3.2 Halide Segregation

It is estimated that a halide perovskite with a band gap of around 1.7-1.85 eV can boost the PCE of commercial PV devices to 30%, where PSCs are used as a top cell in tandem applications. Nevertheless, most of the highest-performing PSCs have band gaps around 1.5-1.6 eV.[37, 98, 108] Although the desired band gap can be easily achieved by tuning the halide composition, there has been a unique challenge called *halide segregation* under illumination in mixed halide perovskites which is detrimental to the PV performance and an obstacle in the path of applications of PSCs in high-efficiency tandem solar cells (Figure 1.16).[37, 64, 109-110]

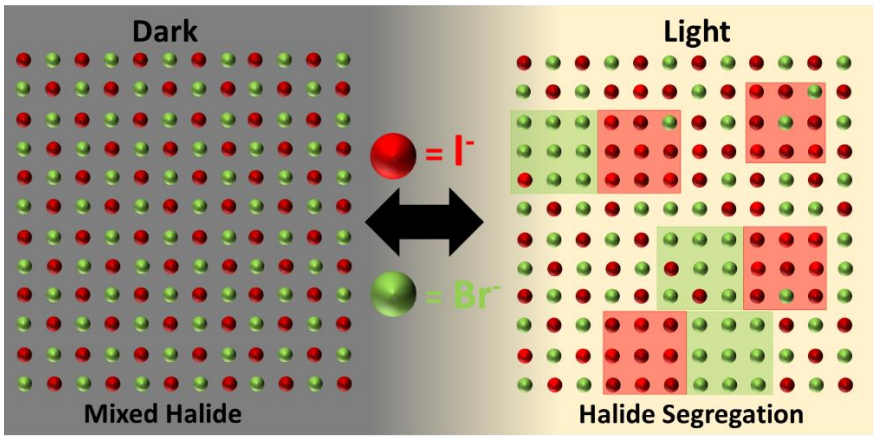

Figure 1.16 Schematic representation of halide segregation in perovskites.

When the perovskite is illuminated, the photovoltage induces an additional electric field acting across the perovskite layer, and causing the migration of ions/vacancies.[64] This results in two phases which are iodide-rich minority and bromide-enriched majority domains, causing the formation of a new peak in PL spectra as well as a splitting in X-ray diffraction (XRD) reflections.[111] Although the segregation effects are reversible under short-term illumination, the research community has voiced concerns

regarding the influence of halide ion mobility on the long-term stability and open circuit voltage of PSCs.[112] Therefore, several strategies were suggested to overcome the photo-instability of mixed halide systems such as growing larger grain sizes[113] to obtain fewer grain boundaries where ion migration predominantly occurs[114] and reduction of the Goldschmidt tolerance factor which improves the stability of perovskite films[115-116].

In addition to the PV applications, lighting devices prepared from perovskites suffer from this phenomenon due to the application of voltage instead of illumination. It has been noticed that the emission from mixed halide perovskite NCs in LEDs red-shifts reversibly during device operation and returns slowly toward the original state after resting. Since the electroluminescence (EL) and PL shifts are completely consistent with each other, these shifts are interpreted as a result of intrinsic changes within the perovskites, e.g. halide segregation. Therefore, it was suggested that band gap tuning of pure (non-mixed) halide systems via quantum size effects might be a more successful way to cover the entire visible spectrum in lighting applications.[117]

1.4 Outline of the Thesis

In this thesis, we focused on the understanding of the intrinsic degradation factors of perovskites such as hysteresis and halide segregation and suggested solutions how to decrease/remove these hurdles in both solar cells and lighting devices.

Chapter 3 describes the relation between the Fermi level alignment between an SnO_x electron transport layer (ETL) combined with multiple-cation mixed-halide perovskite and anomalous hysteresis in *J-V* measurements in PSCs. In addition, the depth of trap states in the ETL and/or at the ETL-perovskite interface was investigated via thermally stimulated current (TSC) measurements, and correlated with Fermi level positions revealed by ultra-violet photoelectron spectroscopy (UPS).

The charge transport characteristics and their limiting factors in PSCs are in the focus of *Chapter 4*. The charge carrier mobilities in mehylammonium lead iodide (MAPI) thin films and solar cells derived from these films were examined by performing time-of-flight (ToF) measurements. Furthermore, complementary experiments on devices with varying thicknesses of charge extraction layers were performed with the aim to reveal the relevant limiting factors.

Chapter 5 elaborates the versatility of perovskite semiconductors by showing nanostructuring of this class of material and applications in lighting devices. Importantly, the synthesis concept of hybrid organic-inorganic perovskite nanoparticles (NPs) was expanded by the exhange of organic cations in the structure, which allowed us to tune the photophysical features that were analyzed by time-resolved photolumuniscence measurements. Additionally, the implementation of these NPs in light-emitting

electrochemical cells (LECs) was demonstrated for the first time by an easily scalable spray-coating technique.

In *Chapter 6*, the superior features of all inorganic perovskite nanocrystals (NCs) over hybrid organic-inorganic counterparts were shown in the concept of LECs. Luminance-current versus applied voltage (LIV) measurements revealed improvements in device features such as brightness, injection voltage as well as spectral elecroluminescence (EL) width when all inorganic perovskite NCs were used instead of hybrid ones. Moreover, stabilization of halide segregation in mixed halide perovskite systems was demonstrated by the use of the salt KCF_3SO_3 in the active layer of the lighting device.

Four-terminal perovskite/CIGS tandem solar cells with an efficiency of 19% are presented in *Chapter 7*. The impact of transparency of a perovskite top-cell on the performance of CIGS bottom-cells was elucidated by employing different transparent conductive oxides as substrates as well as back-electrodes. The observe low voltage of these tandem devices was attributed to the halide segregation in the perovskite top-cell detected by XRD measurements upon application of illumination and bias, and suggestions to overcome this challenge were provided.

1.5 References

1. Mehrer, H., *Diffusion in Solids: Fundamentals, Methods, Materials, Diffusion-Controlled Processes*. Springer Berlin Heidelberg: 2007.
2. Lidia, Ł.; Andrzej, J., *Journal of Telecommunications and Information Technology* **2010,** 1, 3-9.
3. Ross, I. M., *Proceedings of the IEEE* **1998,** 86, 7-28.
4. Platzman, G. W., *Bulletin of the American Meteorological Society* **1979,** 60, 302-312.
5. McCartney, S., *ENIAC: The Triumphs and Tragedies of the World's First Computer*. Walker & Company: 1999; p 240.
6. Fiore, J. M., *Semiconductor Devices:Theory and Application*. 2018.
7. Bohr, M., Continuing Moore's Law. 2017.
8. Pantelides, S. T., *Reviews of Modern Physics* **1978,** 50, 797-858.
9. Blakemore, J. S., *Semiconductor Statistics*. Dover: 2002.
10. Orton, J. W.; Press, O. U., *The Story of Semiconductors*. OUP Oxford: 2004.
11. Koole, R.; Groeneveld, E.; Vanmaekelbergh, D.; Meijerink, A.; de Mello Donegá, C., Size Effects on Semiconductor Nanoparticles. In *Nanoparticles: Workhorses of Nanoscience*, de Mello Donegá, C., Ed. Springer Berlin Heidelberg: Berlin, Heidelberg, 2014; pp 13-51.
12. Rotello, V. M., *Nanoparticles: Building Blocks for Nanotechnology*. Kluwer Academic/Plenum Publishers: 2004.
13. Smith, A. M.; Nie, S., *Acc. Chem. Res.* **2009,** 43, 190-200.
14. Sinha, S. N., N.K., Nanotechnology Vol. 8:Electronics and Photovoltaics. Studium Press LLC: 2013; p 411.
15. Buhro, W. E.; Colvin, V. L., *Nat. Mater.* **2003,** 2, 138.
16. Wise, F. W., *Acc. Chem. Res.* **2000,** 33, 773-780.
17. Donega, C. d. M., *Chem. Soc. Rev.* **2011,** 40, 1512-1546.
18. Alivisatos, A. P., *Science* **1996,** 271, 933-937.
19. Rabouw, F. T.; de Mello Donega, C., *Top. Curr. Chem.* **2016,** 374, 58.
20. Applications of Semiconductors. In *Semiconductor Materials: An Introduction to Basic Principles*, Springer US: Boston, MA, 2003; pp 107-134.
21. Piprek, J., *Semiconductor Optoelectronic Devices: Introduction to Physics and Simulation*. Academic Press: 2003.
22. Matteo, B.; Claudio, P., *Progress in Photovoltaics: Research and Applications* **2007,** 15, 51-68.
23. Correa-Baena, J.-P.; Saliba, M.; Buonassisi, T.; Grätzel, M.; Abate, A.; Tress, W.; Hagfeldt, A., *Science* **2017,** 358, 739-744.
24. Schubert, E. F., *Light-Emitting Diodes (3rd Edition)*. 2018.

25. Veldhuis, S. A.; Boix, P. P.; Yantara, N.; Li, M.; Sum, T. C.; Mathews, N.; Mhaisalkar, S. G., *Adv. Mater.* **2016,** 28, 6804-6834.
26. Qian, G.; Lin, Y.; Wantz, G.; Davis, A. R.; Carter, K. R.; Watkins, J. J., *Adv. Funct. Mater.* **2014,** 24, 4484-4490.
27. Costa, R. D.; Orti, E.; Bolink, H. J.; Monti, F.; Accorsi, G.; Armaroli, N., *Angew. Chem. Int. Ed.* **2012,** 51, 8178-8211.
28. Aygüler, M. F.; Weber, M. D.; Puscher, B. M. D.; Medina, D. D.; Docampo, P.; Costa, R. D., *J. Phys. Chem. C* **2015,** 119, 12047-12054.
29. Zhu, H., et al., *Nat Mater* **2015,** 14, 636-642.
30. Farrell, A. C.; Senanayake, P.; Meng, X.; Hsieh, N. Y.; Huffaker, D. L., *Nano Lett.* **2017,** 17, 2420-2425.
31. Ramasamy, P.; Lim, D.-H.; Kim, B.; Lee, S.-H.; Lee, M.-S.; Lee, J.-S., *Chem. Commun.* **2016,** 52, 2067-2070.
32. Avrutin, V.; Izyumskaya, N.; Morkoç, H., *Superlattices Microstruct.* **2011,** 49, 337-364.
33. Goswami, D. Y., *Principles of Solar Engineering, Third Edition*. CRC Press: 2015.
34. Sahoo, S. K.; Manoharan, B.; Sivakumar, N., Chapter 1 - Introduction: Why Perovskite and Perovskite Solar Cells? In *Perovskite Photovoltaics*, Thomas, S.; Thankappan, A., Eds. Academic Press: 2018; pp 1-24.
35. *Fundamentals of Materials for Energy and Environmental Sustainability*. Cambridge University Press: Cambridge, 2011.
36. Shah, A.; Torres, P.; Tscharner, R.; Wyrsch, N.; Keppner, H., *Science* **1999,** 285, 692-698.
37. Chen, B.; Zheng, X.; Bai, Y.; Padture, N. P.; Huang, J., *Adv. Energy Mater.* **2017**, 1602400-n/a.
38. L., F. H.; C., P. G.; Stephen, C. R.; E., D. G. J.; Breen, C. T., *Adv. Mater.* **2012,** 24, 2673-2678.
39. Amir, A.; Andreas, S.; Christian, L.; Roger, B.; Martti, T.; Ronald, Ö.; Ludvig, E., *Adv. Funct. Mater.* **2015,** 25, 3238-3245.
40. Lanz, T.; Sandström, A.; Tang, S.; Chabrecek, P.; Sonderegger, U.; Edman, L., *Flex. Print. Electron.* **2016,** 1, 025004.
41. Sandström, A.; Asadpoordarvish, A.; Enevold, J.; Edman, L., *Adv. Mater.* **2014,** 26, 4974-4974.
42. Tang, S.; Sandström, A.; Lundberg, P.; Lanz, T.; Larsen, C.; van Reenen, S.; Kemerink, M.; Edman, L., *Nat. Commun.* **2017,** 8, 1190.
43. Lindh, E. M.; Lundberg, P.; Lanz, T.; Mindemark, J.; Edman, L., *Sci. Rep.* **2018,** 8, 6970.
44. Pei, Q.; Yu, G.; Zhang, C.; Yang, Y.; Heeger, A. J., *Science* **1995,** 269, 1086-1088.
45. Hierlinger, C.; Trzop, E.; Toupet, L.; Ávila, J.; La-Placa, M.-G.; Bolink, H. J.; Guerchais, V.; Zysman-Colman, E., *J. Mater. Chem. C* **2018,** 6, 6385-6397.
46. Meltem, F. A.; Bianka, M. D. P.; Yu, T.; Thomas, B.; Alexander, S. U.; Ruben, D. C.; Pablo, D., *J. Phys. D* **2018**.

47. Bader, A. J. N.; Ilkevich, A. A.; Kosilkin, I. V.; Leger, J. M., *Nano Lett.* **2011,** 11, 461-465.
48. D., W. M.; Matthias, A.; R., T. R.; D., C. R., *Adv. Funct. Mater.* **2015,** 25, 5066-5074.
49. Puscher, B. M. D.; Aygüler, M. F.; Docampo, P.; Costa, R. D., *Adv. Energy Mater.* **2017,** 7, 1602283.
50. Johannes, Z.; Luca, P.; Tobias, R.; Ana, S.-S.; David, M.; Gerardo, H.-S., *Adv. Funct. Mater.* **2018,** 28, 1705795.
51. Liu, J.; Oliva, J.; Tong, K.; Zhao, F.; Chen, D.; Pei, Q., *Sci. Rep.* **2017,** 7, 1524.
52. Watthage, S. C.; Song, Z.; Phillips, A. B.; Heben, M. J., Chapter 3 - Evolution of Perovskite Solar Cells. In *Perovskite Photovoltaics*, Thomas, S.; Thankappan, A., Eds. Academic Press: 2018; pp 43-88.
53. NREL, **2018,** accessed: July 2018.
54. R., V. P., *Helvetica Chimica Acta* **2017,** 100, e1700090.
55. Dou, L.; Yang, Y.; You, J.; Hong, Z.; Chang, W.-H.; Li, G.; Yang, Y., *Nat. Commun.* **2014,** 5, 5404.
56. Chin, X. Y.; Cortecchia, D.; Yin, J.; Bruno, A.; Soci, C., *Nat. Commun.* **2015,** 6, 7383.
57. Ji, Y. E.; Miaoqiang, L.; Jung-Ho, Y.; Jung, K. C.; Jin, C. Y.; Lianzhou, W., *Adv. Mater.* **2015,** 27, 6170-6175.
58. Sadhanala, A., et al., *Nano Lett.* **2015,** 15, 6095-6101.
59. Lozano, G., *J. Phys. Chem. Lett.* **2018**, 3987-3997.
60. Quyet, L.; Won, J. H.; Young, K. S., *Small Methods* 0, 1700419.
61. Boix, P. P.; Agarwala, S.; Koh, T. M.; Mathews, N.; Mhaisalkar, S. G., *J. Phys. Chem. Lett.* **2015**.
62. Chen, P.-Y.; Qi, J.; Klug, M. T.; Dang, X.; Hammond, P. T.; Belcher, A. M., *Energy Environ. Sci.* **2014,** 7, 3659-3665.
63. Protesescu, L.; Yakunin, S.; Bodnarchuk, M. I.; Krieg, F.; Caputo, R.; Hendon, C. H.; Yang, R. X.; Walsh, A.; Kovalenko, M. V., *Nano Lett.* **2015,** 15, 3692-3696.
64. Xiao, Z., et al., *Mat. Sci. Eng. R* **2016,** 101, 1-38.
65. Eperon, G. E.; Stranks, S. D.; Menelaou, C.; Johnston, M. B.; Herz, L. M.; Snaith, H. J., *Energy Environ. Sci.* **2014,** 7, 982-988.
66. Colella, S.; Mazzeo, M.; Rizzo, A.; Gigli, G.; Listorti, A., *J. Phys. Chem. Lett.* **2016,** 7, 4322-4334.
67. Mitzi, D. B.; Wang, S.; Feild, C. A.; Chess, C. A.; Guloy, A. M., *Science* **1995,** 267, 1473-1476.
68. Akhtar, J.; Aamir, M.; Sher, M., Chapter 2 - Organometal Lead Halide Perovskite. In *Perovskite Photovoltaics*, Thomas, S.; Thankappan, A., Eds. Academic Press: 2018; pp 25-42.
69. Mitzi, D. B., *J. Chem. Soc., Dalton Trans.* **2001**, 1-12.
70. Mitzi, D. B., *Chem. Mater.* **2001,** 13, 3283-3298.

71. Schmidt, L. C.; Pertegas, A.; Gonzalez-Carrero, S.; Malinkiewicz, O.; Agouram, S.; Minguez Espallargas, G.; Bolink, H. J.; Galian, R. E.; Perez-Prieto, J., *J. Am. Chem. Soc.* **2014,** 136, 850-853.
72. Tan, Z.-K., et al., *Nat. Nanotechnol.* **2014,** 9, 687-692.
73. Green, M. A.; Ho-Baillie, A.; Snaith, H. J., *Nat. Photonics* **2014,** 8, 506.
74. Saliba, M., et al., *Science* **2016**.
75. Saliba, M., et al., *Energy Environ. Sci.* **2016,** 9, 1989-1997.
76. Banerjee, D.; Chattopadhyay, K. K., Chapter 5 - Hybrid Inorganic Organic Perovskites: A Low-Cost-Efficient Optoelectronic Material. In *Perovskite Photovoltaics*, Thomas, S.; Thankappan, A., Eds. Academic Press: 2018; pp 123-162.
77. Saidaminov, M. I., et al., *Nat. Commun.* **2015,** 6, 7586.
78. Zhang, F.; Zhong, H.; Chen, C.; Wu, X.-g.; Hu, X.; Huang, H.; Han, J.; Zou, B.; Dong, Y., *ACS Nano* **2015,** 9, 4533-4542.
79. Tyagi, P.; Arveson, S. M.; Tisdale, W. A., *J. Phys. Chem. Lett.* **2015,** 6, 1911-1916.
80. Wong, A. B.; Lai, M.; Eaton, S. W.; Yu, Y.; Lin, E.; Dou, L.; Fu, A.; Yang, P., *Nano Lett.* **2015,** 15, 5519-5524.
81. Nedelcu, G.; Protesescu, L.; Yakunin, S.; Bodnarchuk, M. I.; Grotevent, M. J.; Kovalenko, M. V., *Nano Lett.* **2015,** 15, 5635-5640.
82. Akkerman, Q. A.; D'Innocenzo, V.; Accornero, S.; Scarpellini, A.; Petrozza, A.; Prato, M.; Manna, L., *J. Am. Chem. Soc.* **2015,** 137, 10276-10281.
83. Kulbak, M.; Cahen, D.; Hodes, G., *J. Phys. Chem. Lett.* **2015,** 6, 2452-2456.
84. Huang, H.; Zhao, F.; Liu, L.; Zhang, F.; Wu, X.-g.; Shi, L.; Zou, B.; Pei, Q.; Zhong, H., *ACS Appl. Mater. Interfaces* **2015,** 7, 28128-28133.
85. Zhuo, S.; Zhang, J.; Shi, Y.; Huang, Y.; Zhang, B., *Angew. Chem.* **2015,** 127, 5785-5788.
86. Tong, Y., et al., *Angew. Chem. Int. Ed.* **2016,** 55, 13887-13892.
87. Le, Q. V.; Kim, J. B.; Kim, S. Y.; Lee, B.; Lee, D. R., *J. Phys. Chem. Lett.* **2017**, 4140-4147.
88. Liyan, Y.; Alexander, T. B.; David, G. L.; Tao, W., *Rep. Prog. Phys.* **2016,** 79, 026501.
89. Bhati, M.; Rai, R., Chapter 13 - Commercialization of Large-Scale Perovskite Solar Energy Technology and Scaling-Up Issues. In *Perovskite Photovoltaics*, Thomas, S.; Thankappan, A., Eds. Academic Press: 2018; pp 387-445.
90. Leijtens, T.; Eperon, G. E.; Pathak, S.; Abate, A.; Lee, M. M.; Snaith, H. J., **2013,** 4, 2885.
91. Leguy, A. M. A., et al., *Chem. Mater.* **2015,** 27, 3397-3407.
92. L., P. M.; Yinghong, H.; Davide, M.; Philip, C.; A., L. A. M.; F., B. P. R.; Pablo, D., *ChemSusChem* **2016,** 9, 2699-2707.
93. Jacobsson, T. J.; Tress, W.; Correa-Baena, J.-P.; Edvinsson, T.; Hagfeldt, A., *J. Phys. Chem. C* **2016,** 120, 11382-11393.

94. Deretzis, I.; Smecca, E.; Mannino, G.; La Magna, A.; Miyasaka, T.; Alberti, A., *J. Phys. Chem. Lett.* **2018,** 9, 3000-3007.
95. Domanski, K., et al., *Energy Environ. Sci.* **2017,** 10, 604-613.
96. Yin, W.-J.; Shi, T.; Yan, Y., *Appl. Phys. Lett.* **2014,** 104, 063903.
97. Buin, A.; Comin, R.; Xu, J.; Ip, A. H.; Sargent, E. H., *Chem. Mater.* **2015,** 27, 4405-4412.
98. Ansari, M. I. H.; Qurashi, A.; Nazeeruddin, M. K., *J. Photochem. Photobiol. C* **2018,** 35, 1-24.
99. Aygüler, M. F., et al., *ACS Appl. Mater. Interfaces* **2018,** 10, 11414-11419.
100. Chen, B., et al., *J. Phys. Chem. Lett.* **2015,** 6, 4693-4700.
101. Unger, E. L.; Hoke, E. T.; Bailie, C. D.; Nguyen, W. H.; Bowring, A. R.; Heumüller, T.; Christoforo, M. G.; McGehee, M. D., *Energy Environ. Sci.* **2014,** 7, 3690-3698.
102. Son, D.-Y.; Kim, S.-G.; Seo, J.-Y.; Lee, S.-H.; Shin, H.; Lee, D.; Park, N.-G., *J. Am. Chem. Soc.* **2018,** 140, 1358-1364.
103. Snaith, H. J., et al., *J. Phys. Chem. Lett.* **2014,** 5, 1511-1515.
104. Calado, P.; Telford, A. M.; Bryant, D.; Li, X.; Nelson, J.; O'Regan, B. C.; Barnes, P. R. F., *Nat. Commun.* **2016,** 7, 13831.
105. van Reenen, S.; Kemerink, M.; Snaith, H. J., *J. Phys. Chem. Lett.* **2015,** 6, 3808-3814.
106. Shao, Y.; Xiao, Z.; Bi, C.; Yuan, Y.; Huang, J., *Nat. Commun.* **2014,** 5, 5784.
107. Guerrero, A.; Bou, A.; Matt, G.; Almora, O.; Heumüller, T.; Garcia-Belmonte, G.; Bisquert, J.; Hou, Y.; Brabec, C., *Adv. Energy Mater.* 0, 1703376.
108. Leijtens, T.; Bush, K. A.; Prasanna, R.; McGehee, M. D., *Nature Energy* **2018**.
109. Samu, G. F.; Janáky, C.; Kamat, P. V., *ACS Energy Lett.* **2017,** 2, 1860-1861.
110. Barker, A. J., et al., *ACS Energy Lett.* **2017,** 2, 1416-1424.
111. Hoke, E. T.; Slotcavage, D. J.; Dohner, E. R.; Bowring, A. R.; Karunadasa, H. I.; McGehee, M. D., *Chem. Sci.* **2015,** 6, 613-617.
112. Yoon, S. J.; Kuno, M.; Kamat, P. V., *ACS Energy Lett.* **2017**, 1507-1514.
113. Miao, H.; Cheng, B.; Yongbo, Y.; Yang, B.; Jinsong, H., *Adv. Sci.* **2016,** 3, 1500301.
114. Shao, Y., et al., *Energy Environ. Sci.* **2016,** 9, 1752-1759.
115. McMeekin, D. P., et al., *Science* **2016,** 351, 151-155.
116. Beal, R. E.; Slotcavage, D. J.; Leijtens, T.; Bowring, A. R.; Belisle, R. A.; Nguyen, W. H.; Burkhard, G. F.; Hoke, E. T.; McGehee, M. D., *J. Phys. Chem. Lett.* **2016,** 7, 746-751.
117. Li, G., et al., *Adv. Mater.* **2016,** 28, 3528-3534.

2 Characterization Techniques

2.1 X-Ray Diffraction (XRD)

XRD is a rapid analytical technique used for phase identification of a crystalline material as well as for the study of unit cell dimensions. It is based on constructive interference of monochromatic X-rays and crystalline samples. These X-rays are filtered to produce monochromatic radiation and collimated to concentrate and direct them toward the sample. The collimated beam of X-rays is incident on a sample and diffracted by crystalline phases in the sample according to Bragg's law,

$$\lambda = 2d\sin\theta \tag{2.1}$$

which describes the consructive intereference where d is the spacing between atomic planes in the crystalline phase, θ is the incident angle and λ is the X-ray wavelength (Figure 2.1). These diffracted X-rays are then detected, processed and counted. The sample is scanned through a range of 2θ angles to attain all possible diffraction directions of the lattice due to the random orientation of the material. Conversion of the diffraction peaks to d-spacings often allows for the identification of the material because of the uniqueness of d-spacing combiantions for each material.

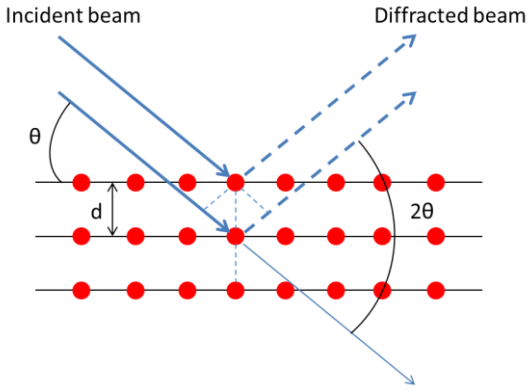

Figure 2.1 Schematic illustration of X-ray diffraction in a crystal lattice. Red circles represent the scattering centers (atoms). θ is X-ray incidence angle. d is the distance between reflecting planes.

X-ray diffractometers consist of three basic elements: an X-ray tube, a sample holder, and an X-ray detector. X-rays are generated in a cathode ray tube by heating a filament to produce electrons. These electrons are accelared toward a target by applying a voltage and the target is bombarded with electrons. When they have sufficient energy to dislodge inner shell electrons of the target material, characteristic X-ray spectra are produced. These spectra have several components such as K_α and K_β.

Copper is the most common target material for single crystal diffraction, with the wavelength of CuK_α radiation = 1.5418 Å. The intensity of the reflected X-rays is recorded as the sample and detector are rotated. When the conditions satisfy Bragg's law, constructive interference occurs and a peak in intensity appears. The signal is recorded by the detector and converted to a count rate, which is output to a device such as a printer or a computer monitor.[1]

2.2 Ultraviolet-Visible (UV-Vis) Absorption Spectroscopy

UV-Vis spectroscopy is a tool to investigate the optical transitions of materials from the ground state to various electronically excited states. The UV region covers a range from 190 nm to 400 nm while the visible is the range between 400 nm and 800 nm. Both quantitative and qualitative studies can be conducted with this technique.

The absorbance (A) at a certain wavelength of the sample is related to the intensity of the incident (I) and measured (I_0) beam, which is defined in the equation

$$A = -log\frac{I}{I_0} \tag{2.2}$$

The Beer-Lambert Law states that the concentration of a substance in solution is directly related to A of the solution

$$A = \epsilon cL \tag{2.3}$$

where ϵ is molar extinction coefficient, c is the concentration of the solution and L is the optical path length.[2]

For samples with multi-layers, Beer-Lambert Law is not applicable due to the scattering and diffraction of the light at the interfaces between two media and this must be taken into account. A reliable determination of the absorbance for this type of materials can be obtained by measurements using an integrating sphere, corrected by choosing a suitable reference.[3]

There are three possibilities of interactions between light and the sample: (i) absorption, (ii) transmission and (iii) reflection (and/or scattering). First, the baseline of the instrument needs to be measured without any sample in the transmission port (100%T) and a Spectralon white standard in the reflectance port (100%R). Later, the transmittance (%T) of both the sample and reference at the transmission port are measured at the transmission port. In the reflectance (%R) measurements, the sample is positioned outside the integrating sphere.

The percentage of the absorbed light %A can be calculated according to the equation

$$\%A = 1 - \%T - \%R \tag{2.4}$$

The absorbance is then given by:

$$A = -\log(1 - \%A) \tag{2.5}$$

$$A_{film} = A_{sample} - A_{reference} \tag{2.6}$$

A Tauc plot is used in order to estimate the band gap of the semiconductors. Typically, Tauc plot shows the quantity hυ (the energy of the light) on the abscissa and the quantity $(\alpha h\upsilon)^{1/r}$ on the ordinate where α is the absorption coefficient of the material. The value of the exponent r denoted the nature of the transition, where r = ½ is for direct allowed transitions and r = 2 is for indirect allowed transition. Therefore, the intersection point of the linear fit of the square of the absorption coefficient and photon energy with the energy axis is found to be a band gap of the semiconductors with direct band gap, whereas in semiconductors with indirect band gap, the intersection point of the linear fit of the square root of the absorption coefficient and photon energy with the energy axis is the band gap.

2.3 Photoluminescence (PL) Spectroscopy

PL spectroscopy is a contactless and non-destructive method to probe the electronic structure of materials. In essence, light is applied to a sample, where it is absorbed and imparts excess energy into the material in a process called *photo-excitation*. This excess energy can be released through the emission of light, so-called *luminescence.* In the case of photo-excitation, this luminescence is called PL. This spectroscopy is of great significance in semiconductors since the band gap and impurities and defect levels of this class of materials can be determined by this technique.

When the energy of the incident photon has sufficient energy, it will excite the electron from the valence band (VB) into the conduction band (CB) across the band gap. When the electrons return to equilibrium (from an excited state to ground state), known as *recombination*, this process can involve both radiative and non-radiative processes.

Radiative recombination is band-to-band recombination where a photon is emitted when an electron moves from its CB to the empty VB state associated with the hole. On the other hand, the electron-hole recombination can also occur without any emission in non-radiative processes. Surface states or bulk defects and traps can cause this kind of recombination (Figure 2.2).[4]

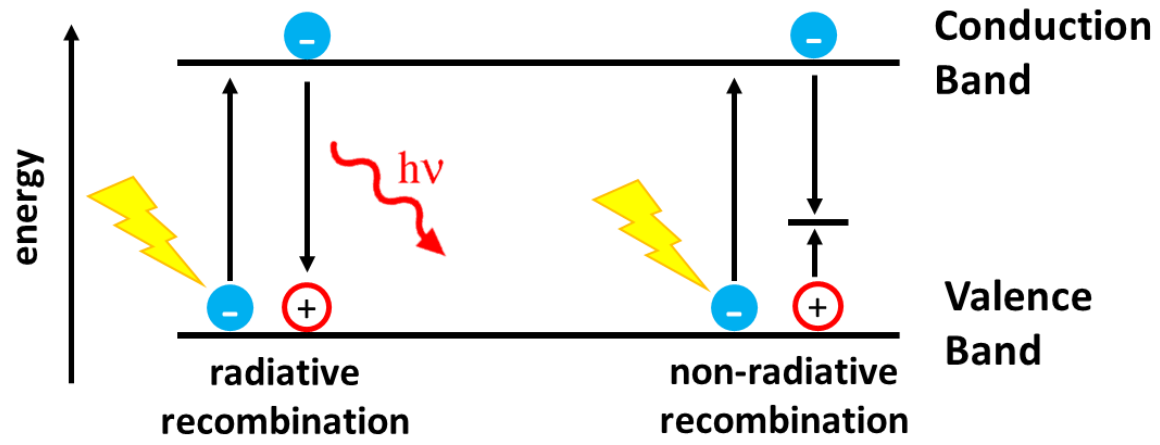

Figure 2.2 Schematic illustration of radiative and non-radiative recombination.

2.4 Time-Correlated Single Photon Counting (TCSPC)

TCSPC is a method to characterize materials and molecules based on their fluorescent properties. It is a time-resolved spectroscopy unlike steady-state methods determining the PL. In this technique, a short pulse of light is used to excite a sample and to observe a decay in a dark environment, where the intensity of the signals is recorded as a function of time. The lifetime of a fluorescent sample is defined as the time necessary for the light intensity of a fluorescent sample to decrease to the fraction 1/e. In short, the lifetime is the average amount of time that a molecule spends in the excited state.

The instrument records the time between when a pulse is generated by the excitation source and when a photon is emitted (Figure 2.3). This information is transferred and the intensity of the emitted photons is plotted against the time. It is important that each time only one photon is measured and each photon is plotted on a histogram (Figure 2.4). A decay curve is generated after the collection of several photons. The reason for using the photon count is that the emission intensity is directly proportional to the probability of detecting a photon at a given time.

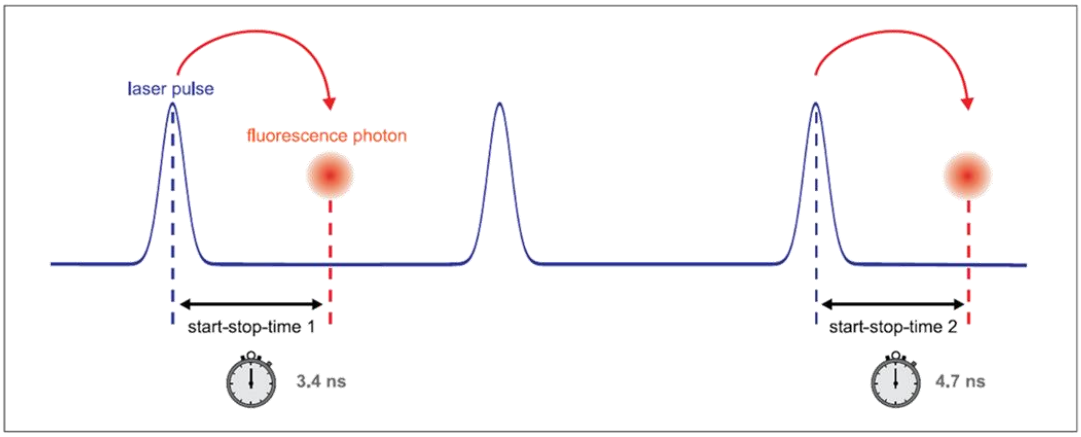

Figure 2.3 Measurement of start-stop times in TCSPC.[5]

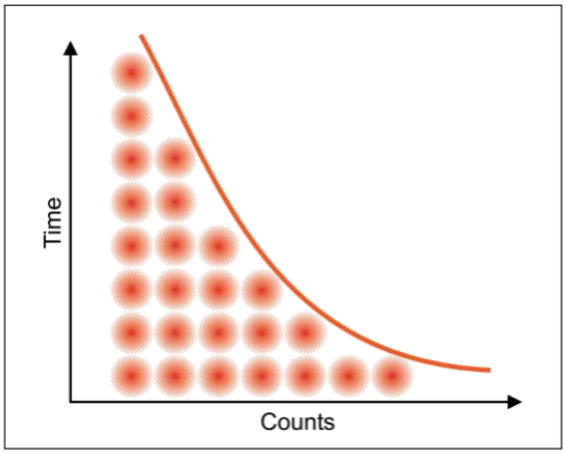

Figure 2.4 Histogram of start-stop times with TCSPC measurements.[5]

As mentioned above, only one photon per excitation must be measured. In case of pulse pileup, the intensity of multiple photons is monitored erroneously for a given time. This will cause a distortion in the early part of the decay curve. To eliminate this problem, the emission beam is attenuated in the instrument.[4]

2.5 Electron Microscopies

Electron microscopes are scientific instruments where highly energetic electrons, in a manner analogous to light, are used to visualize objects on a very fine scale. This tool provides information about not only the topography and morphology but also on composition and crystallographic details.

There are two types of electron microscopies: transmission and scanning electron microscopies.

2.5.1 Transmission Electron Microscopy (TEM)

TEM is a technique where an electron beam interacts and passes through a specimen. In TEM, both compositional and crystallographic information can be obtained. This technique can be compared with a slide projector (Figure 2.5). In TEM, the light source is replaced by an electron source and the glass lenses are replaced by magnetic lenses. A fluorescent screen or an electronic imaging device such as charge-coupled device (CCD) camera, is used instead of a projector screen in TEM. The whole electron trajectory (from source to screen) is under vacuum and the sample needs to be very thin to allow the electrons to pass through it.[6]

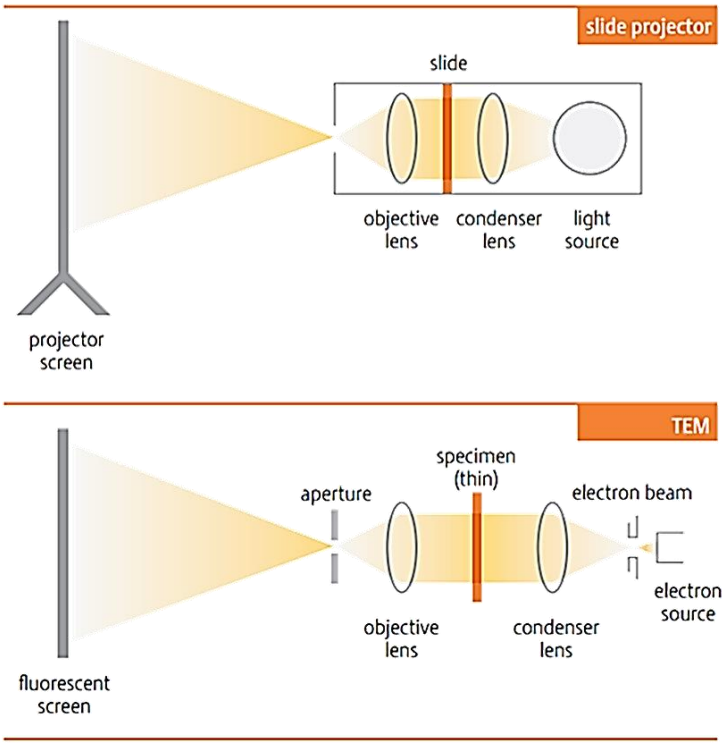

Figure 2.5 TEM compared with a slide projector.[6]

After the generation of the electrons by a source, they are focused and magnified by magnetic lenses. The geometry of the TEM is shown in Figure 2.6. The electron beam confined by the condenser lenses passes the condenser aperture and hits the sample surface. The transmitted beams which are formed due to elastic scattering of the electrons pass through the objective lens. The image display occurs in the objective lens and elastically scattered electrons which form the image of the microscope are chosen in the objective and selected area aperture. Lastly, the beam goes to a magnifying system and the formed image is shown on the monitor.

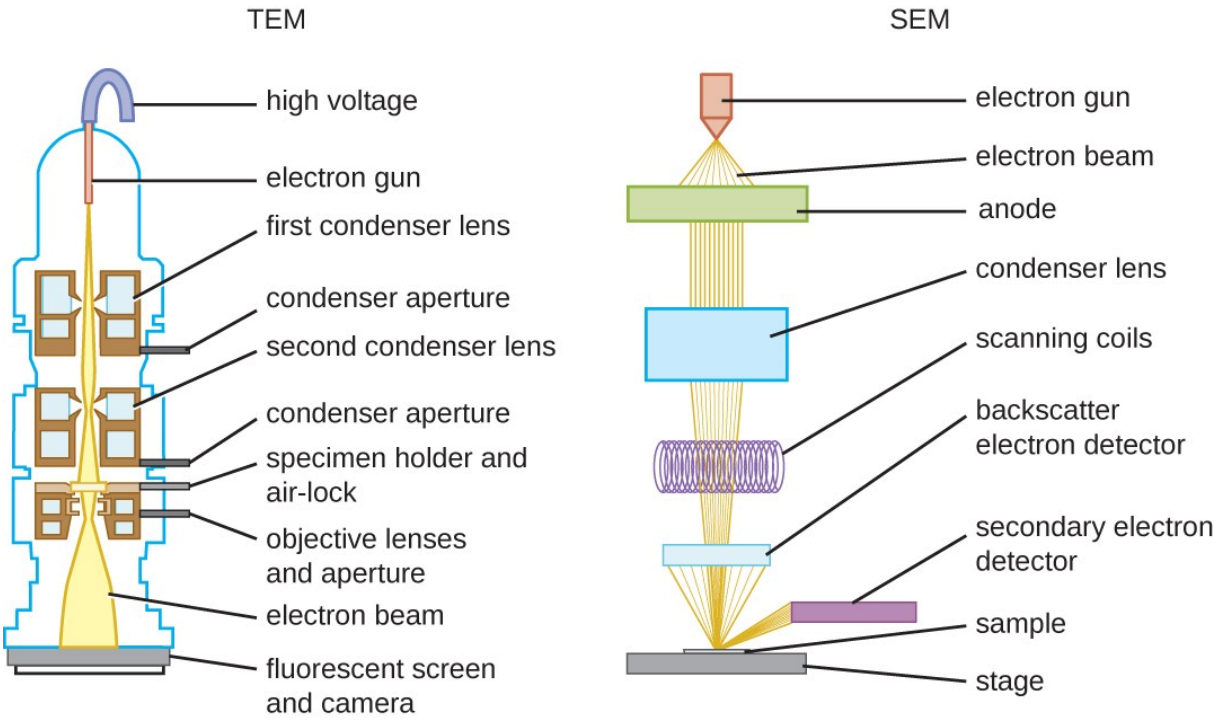

Figure 2.6 Schematic illustrations comparing TEM and SEM.[7]

TEM enables one to obtain different types of images by using different types of electrons selected through different apertures. For instance, diffraction patterns are shown because of the scattered electrons. If the unscattered beam is chosen, a bright field image is obtained whereas dark field images are attained when the diffracted beam is selected by the objective aperture.[8]

2.5.2 Scanning Electron Microscopy (SEM)

SEM is a type of electron microscopy where the images are produced by scanning the sample surface with a focused beam of electrons. The electron beam passes through an objective lens and scan coils and that deflect horizontally and vertically so that the beam scans the surface of the sample (Figure 2.6).

When the electrons penetrate the sample surface, several interactions take place such as emission of electrons or photons from or through the surface. The detectors collect a fraction of the emitted electrons and the output can be used to modulate the brightness of a cathode ray tube (CRT) where the image is produced. Every point that the beam hits on the sample is mapped directly onto a corresponding point on the screen.[8]

The most commonly imaged signals in SEM are from secondary electrons (SE) and backscattered electrons (BSE) (Figure 2.7). Due to their rather low energies, they can leave the sample only when they originate very close to the sample surface. Therefore, SE images have high spatial resolution and topographic contrast. On the other hand, the BSE signal is used for its strong atomic number contrast. For elemental microanalysis, characteristic X-rays can be used in SEM.[6]

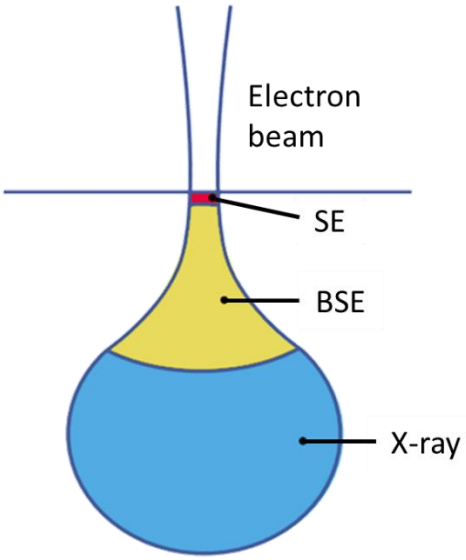

Figure 2.7 Different types of signal originate from different interaction volumes of the electrons with the sample.[6]

2.6 Atomic Force Microscope (AFM)

AFM allows for measuring surface structure with high resolution and accuracy. For example, it is possible to see the arrangement of individual atoms in a sample and the structure of individual molecules. The quantitative information about features such as roughness and height distributions can be obtained from this technique.

Unlike other microscopes focusing light or electron beam onto a surface of the sample, an AFM physically senses the sample's surface with a sharp probe and maps the height of the sample's surface. This feature is very different from an imaging microscope where rotation of the sample is needed to obtain the height of the sample.[9]

In AFM, a cantilever-type spring is used as a tip to probe the surface. The cantilever is deflected as a response to the force between tip and sample. The scanning of the sample followed by digitization of the deflection of the cantilever or the z-movement of the piezo-stage as a function of lateral positions x, y forms the images in AFM. Typical forces between tip and sample range from 10^{-11} to 10^{-6} N. AFM can operate in either contact, semi-contact, or non-contact modes by controlling the separation of the probe at fixed distances from the sample surface.[10]

2.7 Atomic Layer Deposition (ALD)

ALD is a thin film deposition method based on alternating saturative surface reactions in a chemical gas phase. By dosing alternating pulses of the source vapours into the reactor, ALD differs from other chemical-vapor-deposition techniques. In each precursor exposure step, the surface is saturated with a near monomolecular layer of that precursor. ALD offers excellent conformality and uniformity and simple and accurate film thickness control due to a unique self-limiting film growth mechanism.[11]

Most ALD processes are based on binary reaction sequences, forming binary compound where two surface reactions occur as shown in Figure 2.8. A finite number of surface species can only be deposited because of the presence of a finite number of (reactive) surface sites. If each of the two surface reactions is self-limiting, the two reactions may sequentially proceed to deposit a thin film with atomic level control.

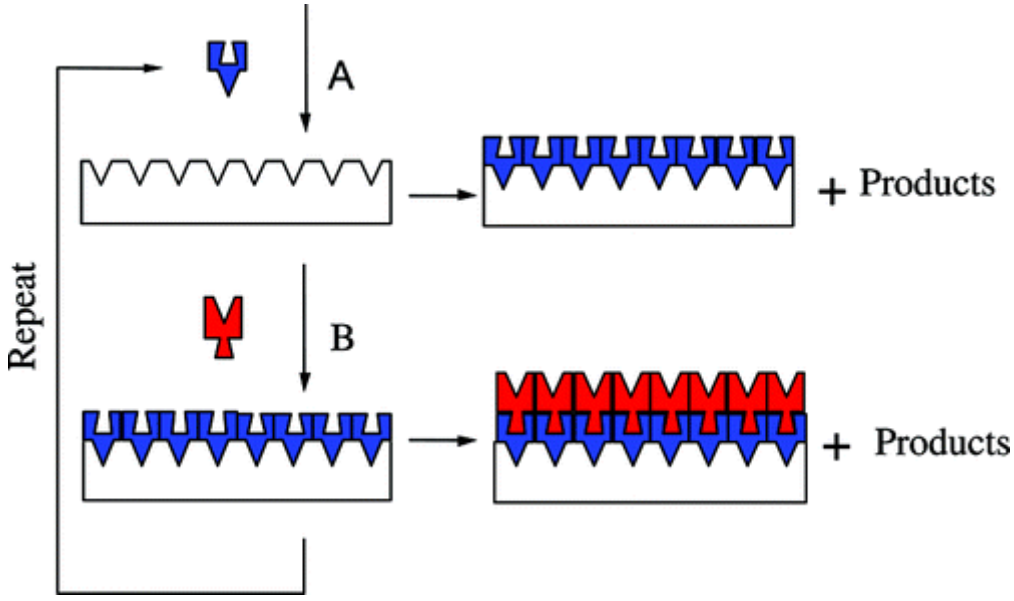

Figure 2.8 Schematic representation of ALD using self-limiting surface chemistry and an AB binary reaction sequence.[12]

During the deposition, some surface areas will react before other surface areas due to the different precursor gas fluxes. However, the precursors will adsorb and subsequently desorb from the surface areas if the reaction is completed. The precursors will react with other unreacted surface areas.

ALD processing can be used to deposit the compounds on rather large substrates as well as to process multiple substrates due to the gas phase of the precursors, filling all space independent of substrate geometry. Moreover, highly conformal coatings can be achieved on corrugated surfaces due to the self-limiting nature of the deposition steps. ALD is only limited by the size of the reaction chamber.[12]

2.8 Ultraviolet Photoelectron Spectroscopy (UPS)

UPS is a standard method to investigate the electronic valence states in materials. It is an extremely surface sensitive technique for the surface characterization, where even a monolayer coverage of an adsorbate or contaminant is sufficient to change the signal from a surface.[13]

UPS relies on the photoemission, where a beam of monochromatic incident photons ejects electrons from the valence/conduction band region of a material into a vacuum (Figure 2.9A). The reference energy is the Fermi level E_F for metals, and the valence band maximum (VBM) used for semiconductors. The lower cutoff of the photoelectron spectrum corresponds to the vacuum level E_V and the upper cutoff to $E_F + h\upsilon$ as shown in Figure 2.9B. The difference ΔE between the two cutoffs can be used to determine the work function $\Phi = E_V - E_F = h\upsilon - \Delta E$. The equivalent quantity for semiconductors is the ionization energy, $E_I = E_V -$ VBM. The work function can be obtained by substracting the energy width from the photon energy. Ionization energy is obtained by this procedure in semiconductos.[14]

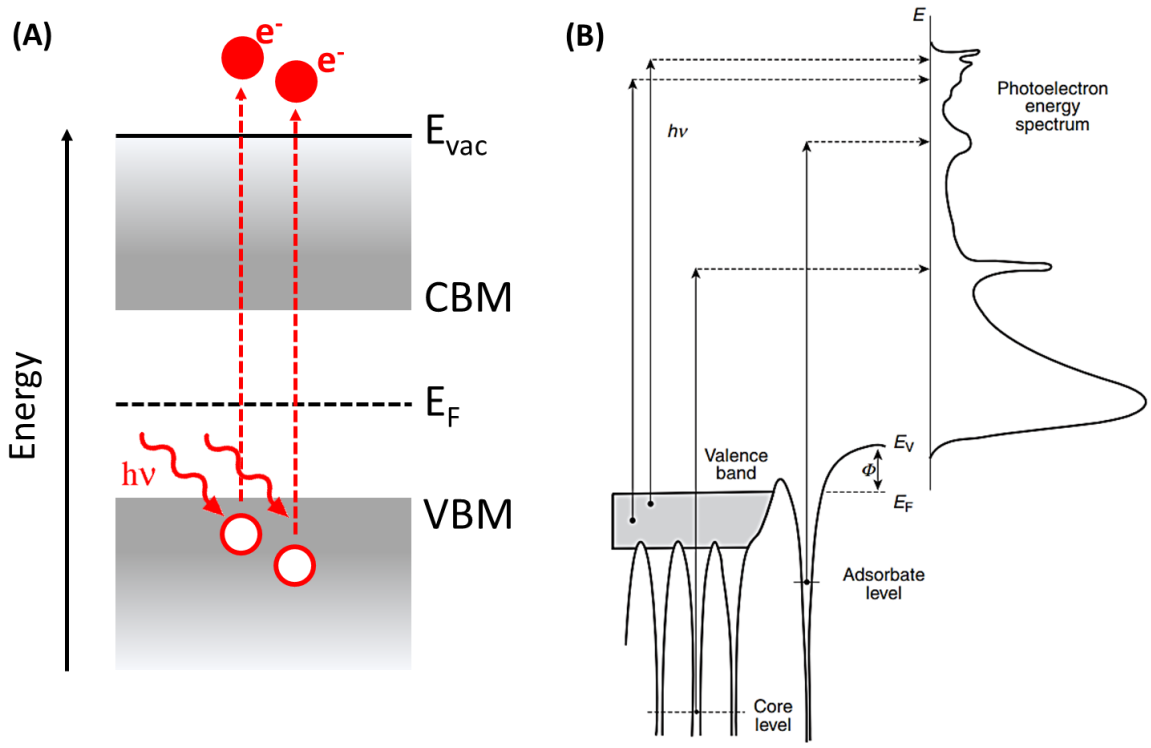

Figure 2.9 (A) Schematic presentation of a UPS. (B) A photoemission experiment.[14]

In UPS, the photons are generated by a gaseous discharge that produces hard UV radiation. The most commonly used gas is helium (He). This will provide an energy of 21.2 eV (He I) or 40.82 eV (He II) with very narrow line widths (~20 meV). Since the bandwidth of the conduction and valence band of many materials is in the range of 5-10 eV, these sources are energetic enough to probe the entire band

structure of most materials. The photoemitted electrons consist of two main groups: (i) the excited electrons within the uppermost atomic layers that do not suffer from inelastic collisions and (ii) the electrons which have had either one or more inelastic collisions or the secondary electrons that have sufficient energy to escape from the material.[13]

2.9 Thermally Stimulated Current Spectroscopy (TSC)

TSC is a powerful method to probe electronic trap states in semiconducting materials or complete photovoltaic devices. The contacted thin films or fully processed solar cells are first cooled down to very low temperatures (~30 K) in dark conditions. The free charge carriers are generated using a white light LED without heating the sample. After the light is turned off, charge carriers relax into the deepest trap states during a certain dwell time where charge carriers populate available trap states in the bulk and at the interfaces in the devices. Due to the lack of sufficient energy, the charge carriers cannot be released from these states. A gradual release of the trapped charges is initiated by heating up the sample to room temperature at a constant rate. The current flow originating from tap release, as shown in Figure 2.10, is precisely recorded and is used to investigate the trap depth as well as the density of defect states in the probed system.

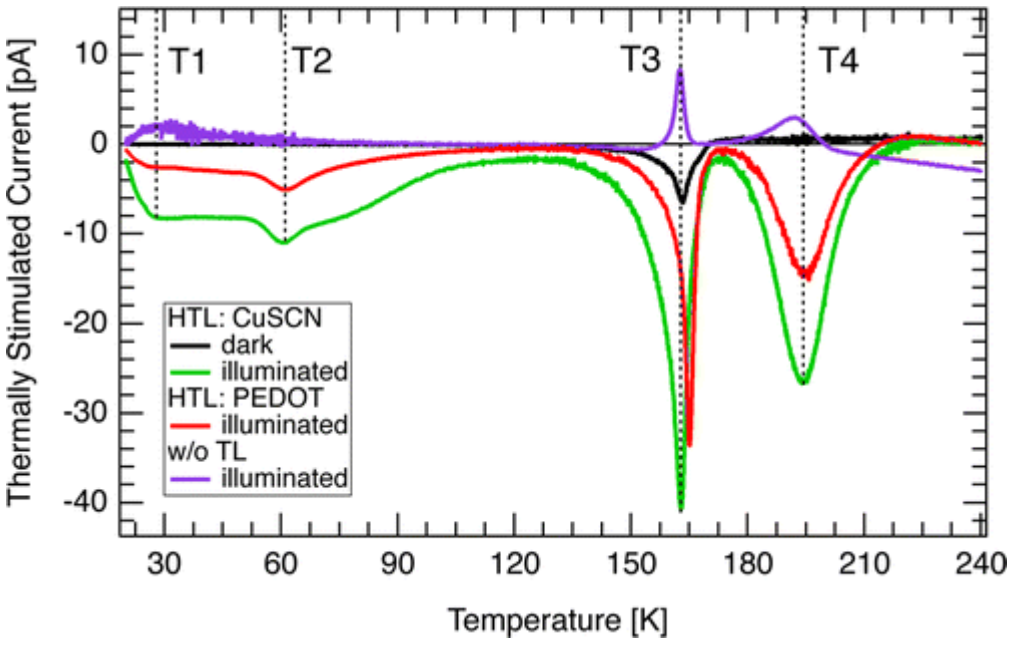

Figure 2.10 Typical TSC signals for photovoltaic devices with different architectures.[15]

In TSC measurements, the peaks arise due to the electronic trap distributions with different thermal activation energies. The intensity of the peaks is ascribed to the density of the trap states. Furthermore, TSC enables one to extract the activation energy of the trap states using the initial rise of the TSC peak which corresponds to the start of trap release due to thermal activation following an activated

(Arrhenius) process. It can be determined by fitting the slope of the TSC peak according to the following equation:

$$I_{TSC} \propto exp\left(-\frac{E_A}{k_B T}\right) \tag{2.7}$$

where E_A, k_B, and T are the activation energy, Boltzmann constant and temperature, respectively. A higher activation energy represents the deeper trap states in the probed system, whereas shallow traps have a lower activation energy.[15]

2.10 Solar Cell Characterization

Measuring solar cell performance is done by performing a *J-V* sweep where different voltages are applied across the solar cell during the measurement of the resulting current. From these curves, a wealth of information is provided that they will be discussed later in this chapter. Figure 2.11 shows a typical *J-V* curve of a perovskite solar cell.

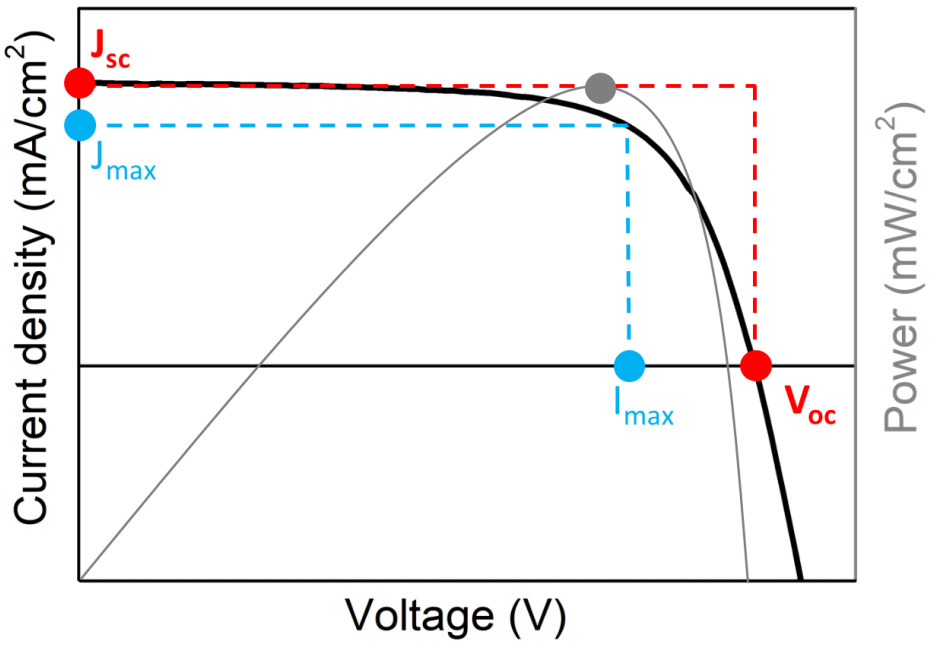

Figure 2.11 A typical *J-V* and power curve for a perovskite solar cell under illumination.

The *J-V* curve of an illuminated solar cell resembles a diode. A solar cell model includes not only a diode and current source as implied in Figure 2.12, but also (optimally minimized) series and (optimally maximized) shunt resistances in the device designed to be useful for performance optimization. Figure 2.12 shows the equivalent circuit diagram for a solar cell. A current source originates from the absorbed light, a diode reflects the directional properties of the solar cell stack, a series resistor R_S represents the resistance in the open diode state and a shunt resistance R_{SH} represents the short-circuited diode state;

all these elements are parts of the equivalent circuit diagram. Therefore, total current through the circuit can be extracted from the following equation:

$$I = I_L - I_D - I_{SH} \tag{2.8}$$

where I is the ouput current of the solar cell, I_L is the photogenerated current, I_D is the diode current and I_{SH} is the shunt current.

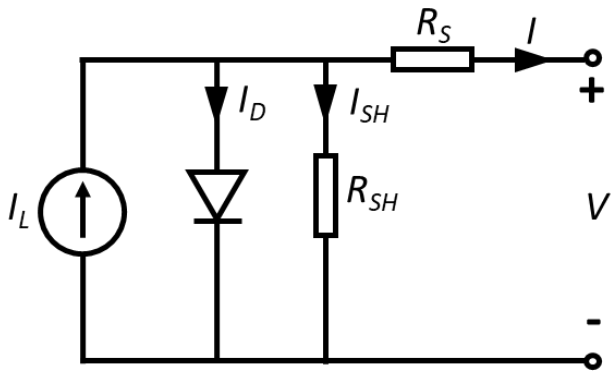

Figure 2.12 Solar cell diode model.

Measurement conditions need to be standardized in order to be able to compare different type of architectures, samples and the results of different laboratories. One important paramaeter is the light intensity, which is standardized to a total light intensity 1000 W/m^2 to represent a full-sunlight condition (1 sun). A standard sunlight spectrum is called air mass 1.5 global (AM1.5G), derived from a representative atmospheric transmittance model where the sun is about 41^o above the horizon.

Solar cell parameters that can be gained from *J-V* curves of the solar cells are short circuit current, J_{sc}, open circuit voltage, V_{oc}, the current J_{max} and voltage V_{max} at the maximum power point P_{max}, fill factor (*FF*) and the power conversion efficiency (*PCE*) of the solar cell, as seen in Figure 2.11. V_{oc} is the maximum voltage that the solar cell will supply whereas J_{sc} is the maximum current of the solar cell under conditions of a zero resistance load.

In order to extract *FF* and the maximum power of the solar cell, the power in each point of the *J-V* curve can be found by the product of the voltage and current. The gray curve in Figure 2.11 represents the power as a function of voltage, where the maximum power point (MPP) is the peak point of the power curve with the corresponding points on the voltage and current axes, V_{max} and J_{max}.

FF is an indication of internal losses, meaning how large the maximum power (represented by blue dotted lines in Figure 2.11) is with respect to the product of V_{oc} and J_{sc}. It can be found by the ratio between maximum power and the full square spanned by V_{oc} and J_{sc} (red dotted lines in Figure 2.11):

$$FF = \frac{J_{max}V_{max}}{J_{sc}V_{oc}} \quad (2.9)$$

The PCE of the solar cells represents the general efficiency of the the solar cells and is directly proportional to the ratio of generated electricity to incoming light energy. The formula for the PCE is:[16]

$$PCE = \frac{J_{sc}V_{oc}\,FF}{P_{light}} \quad (2.10)$$

2.11 Luminance-Current-Voltage (LIV) Characterization

Characterization of light emitting devices can be done by mesasuring their current density (I) as a function of the applied voltage and the luminance (L) as a function of the voltage (V) as shown in Figure 2.1. In these measurements, the injected current and emitted flux are obtained with applied voltage. The current is converted to the current density to consider the active surface area of the device. The flux is converted to luminance (cd/m^2).[17]

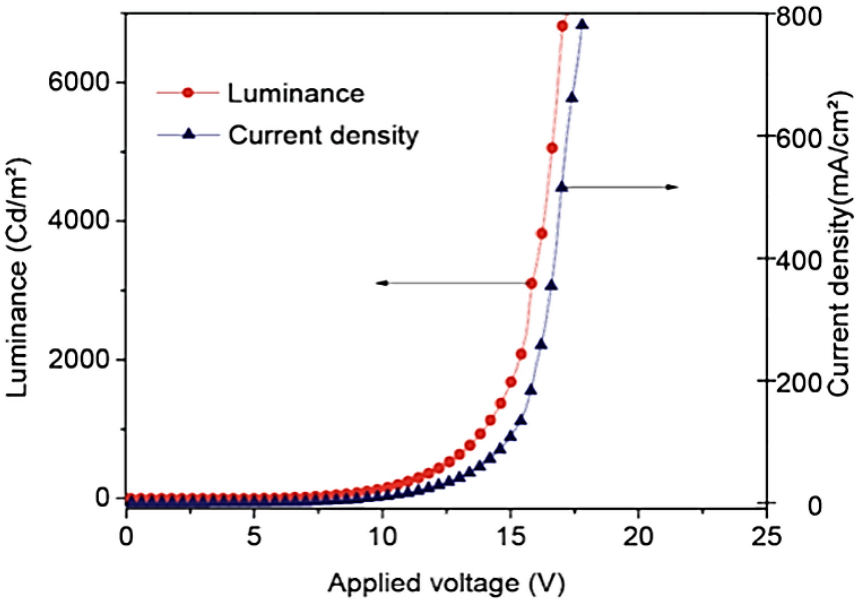

Figure 2.13 LIV characteristics of an OLED.[17]

The above mentioned standard tool for the characterization of light-emitting devices is not applicable to light-emitting electrochemical cells (LECs) used in this thesis since the application of voltage triggers the movement of ionic charges and physically modifies the device itself. Therefore, to perform LIV analysis on LECs, a method was developed that applies a fixed voltage and monitors the current density and luminescence over time while performing rapid LIV scans at set intervals. It is crucial that there is

no ionic movement during these measurements since the electronic characteristics of the device for a given ionic distribution is of interest.[18]

2.12 Time of Flight (ToF)

ToF is a well-established method to extract the mobility of charge carriers in semiconductors and solar cells.[19] The ToF mehod is based on the measurement of the carrier transit time, namely, the time required for a sheet of charge carriers photogenerated near one of the electrodes by pulsed light irradiation to drift across the sample to the other electrode under an applied electric field. In a typical ToF configuration, the semiconducting material to be measured is sandwiched between two electrodes, where one of them is transparent or semitransparent to allow the illumination to reach the semiconductor. One of the advantages of using this technique is that the hole and electron mobility can be investigated separately.[20] Since the charge carriers are locally created near one electrode, the polarity of the applied voltage determines whether the contribution of electrons or holes to the photocurrent extracted at the opposite electrode is observed.[21] ToF requires thick semiconductor films for accurate measurement since the charge transporting distance (film thickness) should be at least over one order of magnitude larger than the materials absorption depth. In ToF meausurements, a low intensity optical excitation should be used to ensure that photogenerated charge carriers do not change the spatial uniformity of the built-in or applid electric field.[22]

2.13 References

1. Bunaciu, A. A.; Udriştioiu, E. g.; Aboul-Enein, H. Y., *Critical Reviews in Analytical Chemistry* **2015,** 45, 289-299.
2. *Royal Society of Chemistry* **2009**.
3. Snaith, H. J.; Ducati, C., *Nano Lett.* **2010,** 10, 1259-1265.
4. Raja, P. M. V.; Barron, A. R., Physical Methods in Chemistry and Nano Science. 2018.
5. Wahl, M. Technical Note on Time-Correlated Single Photon Counting *PicoQuant GmbH* [Online], 2014.
6. *FEI Company* **2010**.
7. Instruments of Microscopy. Accessed 26/06/2018.
8. Voutou, B.; Stefanaki, E.-C., *Phys. Adv. Mater. Winter School* **2008**, 1-11.
9. Eaton, P.; West, P., *Atomic Force Microscopy*. OUP Oxford: 2010.
10. Meyer, E., *Progress in Surface Science* **1992,** 41, 3-49.
11. Ritala, M.; Leskelä, M., Chapter 2 - Atomic layer deposition A2 - Nalwa, Hari Singh. In *Handbook of Thin Films*, Academic Press: Burlington, 2002; pp 103-159.
12. George, S. M., *Chem. Rev.* **2010,** 110, 111-131.
13. Leckey, R., Ultraviolet Photoelectron Spectroscopy of Solids. In *Surface Analysis Methods in Materials Science*, O'Connor, D. J.; Sexton, B. A.; Smart, R. S. C., Eds. Springer Berlin Heidelberg: Berlin, Heidelberg, 1992; pp 291-300.
14. Ultraviolet Photoelectron Spectroscopy. In *Characterization of Materials*.
15. Baumann, A.; Väth, S.; Rieder, P.; Heiber, M. C.; Tvingstedt, K.; Dyakonov, V., *J. Phys. Chem. Lett.* **2015,** 6, 2350-2354.
16. Methods and Instruments for the Characterization of Solar Cells. In *Photovoltaic Solar Energy*.
17. Boudrioua, A.; Chakaroun, M.; Fischer, A., *An Introduction to Organic Lasers*. Elsevier Science: 2017.
18. Costa, R. D.; Orti, E.; Bolink, H. J.; Monti, F.; Accorsi, G.; Armaroli, N., *Angew. Chem. Int. Ed.* **2012,** 51, 8178-8211.
19. Andreas, B.; Irene, G.; Niklas, H.; Kristina, P.; G., H. A.; Matthias, H.; Pablo, D.; Achim, H.; Thomas, B., *Chemistry – An Asian Journal* **2016,** 11, 1199-1204.
20. Tiwari, S.; Greenham, N. C., *Optical and Quantum Electronics* **2009,** 41, 69-89.
21. Grill, I.; Aygüler, M. F.; Bein, T.; Docampo, P.; Hartmann, N. F.; Handloser, M.; Hartschuh, A., *ACS Appl. Mater. Interfaces* **2017,** 9, 37655-37661.
22. Xiao, Z., et al., *Mat. Sci. Eng. R* **2016,** 101, 1-38.

3 Influence of Fermi Level Alignment on the Hysteresis of Perovskite Solar Cells

This chapter is based on the following publication:

Meltem F. Aygüler, Alexander G. Hufnagel, Philipp Rieder, Michael Wussler, Wolfram Jaegermann, Thomas Bein, Vladimir Dyakonov, Michiel L. Petrus, Andreas Baumann, Pablo Docampo, *ACS Applied Materials and Interfaces*, 2018, 10, 11414-11419.

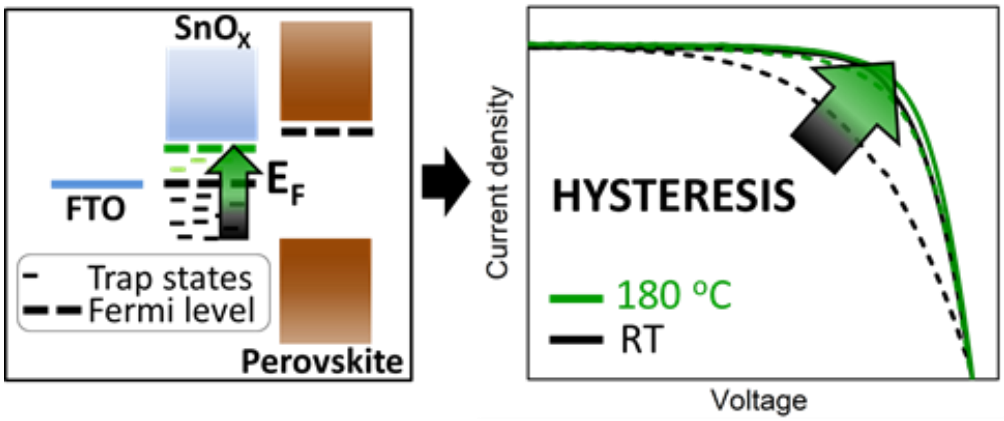

Keywords

Perovskite solar cells, hysteresis, perovskite-contact interface, Fermi level alignment, trap depth energy, tin oxide

3.1 Introduction

An astonishing improvement in power conversion efficiency (PCE) of perovskite solar cells (PSCs) from 3.8% up to more than 22% in a few years has brought them to the forefront of photovoltaic research with the goal of producing low-cost and solution-processed yet competitively efficient solar cells.[1-3] In spite of the enormous growth in the field, their development is still hampered by anomalous hysteresis in the characteristic current-voltage (*J-V*) scan of the solar cells.[4] This effect has been linked to several processes such as ion migration in the perovskite phase, trapping of electronic carriers at the perovskite - electron transport layer (ETL) or hole transport layer (HTL) interface as well as ferroelectric polarization.[5-6] However, none of these processes fully account for the behavior observed: perovskites have poor polarization retention at room temperature[7], charge trapping and detrapping occurs on a much faster timescale than hysteresis (microseconds vs tens of seconds); and ion migration cannot offer a complete explanation of why changing the interfacial contact materials, i.e. fabrication of inverted solar cells employing PEDOT:PSS and PCBM, yield such pronounced differences regarding the hysteretic behavior of the devices.[6]

Despite the limited understanding of hysteresis in PSCs, several studies have demonstrated that the hysteresis can be suppressed by modifying the interface between ETL and perovskite or replacing the contact materials. The first approach was realized with fullerene derivatives with/without self-assembled monolayers (SAMs), resulting in negligible hysteresis in solar cells by reducing the non-radiative recombination channels due to the reduction in the trap density at this interface.[8-10] Additionally, ZnO was shown to be a promising alternative to TiO_2 due to better electron mobility, very high transmittance as well as lower fabrication cost.[11] However, there are still issues regarding degradation of the perovskite due to the basic surface of ZnO which therefore requires the use of organic interfacial layers to maximize performance and minimize hysteresis.[12-13] Although thermal annealing of the ZnO layers improves the perovskite stability on ZnO, it does not guarantee long-term stability of the system.[12]

More recent efforts by van Reenen *et al.* demonstrated that several mechanisms are at play, where both ion migration and electronic charge traps must be included to achieve hysteresis in the modeled *J-V* characteristics.[4] Recently, Calado *et al.* confirmed this hypothesis by showing ion migration regardless of whether the devices show hysteresis or not. Their transient optoelectronic measurements as well as device simulations revealed that hysteresis requires the combination of both mobile ionic charge and recombination near the perovskite - contact interfaces.[6] Furthermore, any built-in field at the ETL-perovskite interface is expected to be screened by

mobile ions.[14] Therefore, matching the Fermi levels of the charge transport layers and the perovskite absorber is important to ensure effective charge extraction and to avoid charge accumulation and recombination.[15]

Here, we have investigated the influence of the Fermi level alignment between the ETL and the absorber on the hysteresis of multiple-cation mixed-halide PSCs. Our ultra-violet photoelectron spectroscopy (UPS) measurements show that annealing SnO_x layers at different temperatures allows fine tuning of their Fermi level, as schematically shown in Figure 3.1A. Furthermore, we link the Fermi level position to the presence of energetically deep trap states in the ETL or at the ETL-perovskite interface with the help of thermally stimulated current (TSC) measurements. We show that the trap depth correlates with an increase in hysteresis of PSCs, likely due to increased charge recombination at the interface. Moreover, our measurements show that if the band alignment between the perovskite absorber and SnO_x layer is fulfilled, the resulting device excels due to greatly reduced hysteresis and much better performance.

3.2 Solar Cell Characterization

The solar cell architecture used in this work is shown in Figure 3.1B in a typical device stack composed of FTO/SnO_x/Perovskite/Spiro-OMeTAD/Gold. Briefly, we deposited SnO_X layers on a fluorine-doped tin oxide (FTO) substrate *via* atomic layer deposition (ALD) at 118 °C.[16] The perovskite absorber, $Cs_{0.05}(FA_{0.83}MA_{0.17})_{0.95}Pb(I_{0.83}Br_{0.17})_3$, was then deposited according to a procedure published by Saliba *et al*.[17] The solar cells were finalized by spin-coating of 2,2′,7,7′-tetrakis-(N,N-dimethoxyphenylamine)-9,9′-spirobifluorene (Spiro-OMeTAD) as a hole transport layer and thermal-deposition under vacuum of gold (Au) electrodes. The full experimental description of the device fabrication can be found in the Experimental Section.

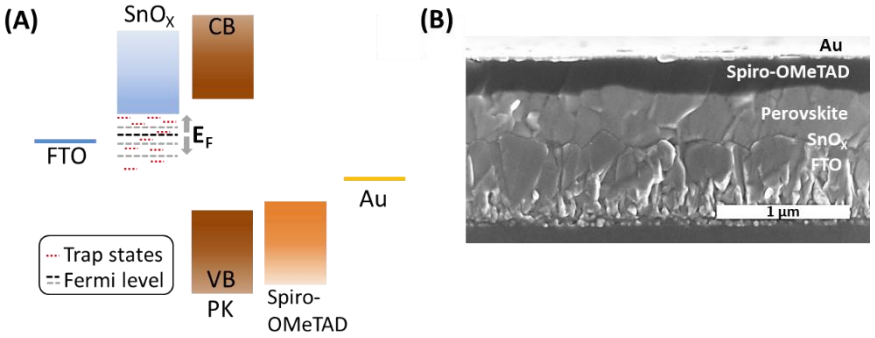

Figure 3.1 (A) Schematic diagram of energy level alignment of PSCs used in this work. Gray dashed lines and arrows depict the Fermi level tuning of SnO_x, which depends on the annealing temperature. Red dashed lines represent the trap states. (B) SEM cross-section of a solar cell.

Solar cells were prepared with as-deposited SnO_x layers as well as layers annealed in air at up to 300 °C. Top-view scanning electron microscopy (SEM) images show that the morphology of the SnO_x (10 nm) layers does not change upon annealing of the substrates (Figure 3.2D, E and F). Also, the morphology of the perovskite layers was not affected by the annealing temperature of the ETL (Figure 3.2A, B, and C).

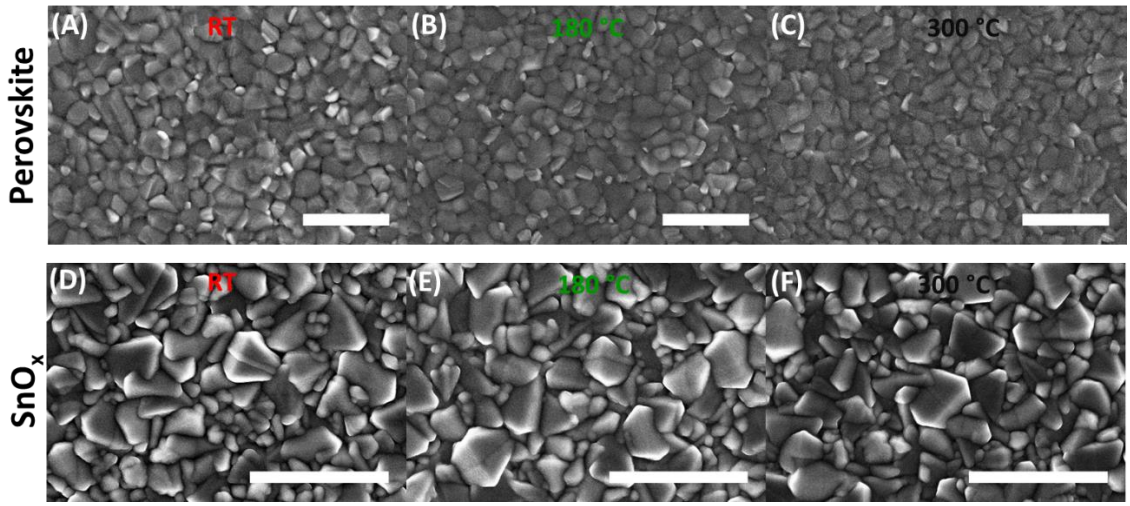

Figure 3.2 SEM top-view images of perovskite on SnO_x (A-C) and SnO_x layers annealed at different temperatures (D-F). Scale bar is 1 µm for all images.

To investigate the influence of the annealing temperature of the SnO_x layer on the device performance, we recorded *J-V* characteristics (Figure 3.3A) of the solar cells and additionally fabricated reference devices incorporating a planar TiO_2 ETL. A summary of the PCEs of the solar cells extracted from the reverse scan of the *J-V* curves is given in Figure 3.3B and the corresponding stabilized power output *via* maximum power point tracking is shown in Figure 3.3C. The PCE of the solar cells slightly increases with the annealing of SnO_x, showing the maximum performance average at an intermediate annealing temperature of 180 °C (Figure 3.3B). On the other hand, solar cells with layers annealed at higher temperatures lose their PCE from 16.1 % (for 180 °C) to 13.9 % (for 300 °C). The observation of a PCE maximum at an ETL annealing temperature of 180 °C is attributed to the change in fill factor (FF), which shows the same trend as the PCE (Figure 3.3D). This key parameter rises up to the optimum annealing temperature (180 °C) and decreases at higher annealing temperature. The drop in open-circuit voltage (V_{oc}) at higher annealing temperatures is likely related to an increase in detrimental defect states formed in SnO_x films (Figure 3.3E).[11] Furthermore, external quantum efficiency (EQE) measurements were performed on the solar cells and integrated current densities from these

measurements are in good agreement with short-circuit current (J_{sc}) values obtained from *J-V* scans (Figure 3.3F).

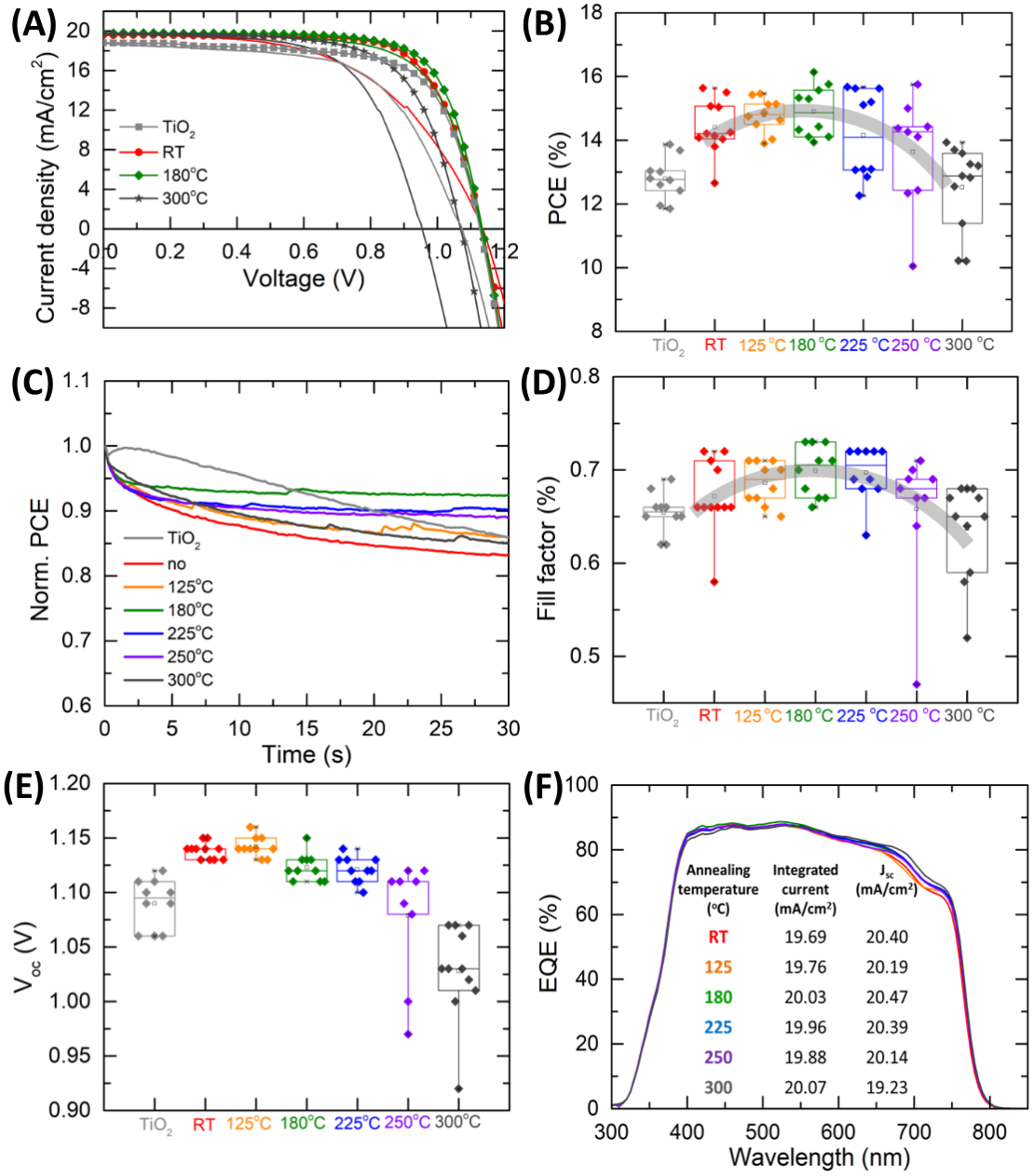

Figure 3.3 (A) *J-V* curve of solar cells fabricated with non- and 180 °C-annealed SnO_x and TiO_2, demonstrating a significant difference in hysteresis between the samples annealed at different temperatures. (B) PCE, (C) maximum power point tracking, (D) FF, (E) V_{oc} and EQE of the solar cells fabricated on SnO_x annealed at different temperatures (9-11 devices for each annealing temperature). The values in (B), (D) and (E) were extracted from the reverse scan of the *J-V* curves. The grey lines are a visual aid to interpret the trend of the results.

All solar cells exhibit some degree of hysteresis (Figure 3.3A), which can be quantified by the so-called hysteresis index (HI).[6] This parameter is extracted from comparing forward and reverse *J-V* curve scans as:

$$HI = \frac{PCE_{rev}}{PCE_{for}} - 1$$

where PCE_{rev} and PCE_{for} are the PCEs extracted from the reverse and forward scan, respectively.[6] Interestingly, we observed that a minimum in hysteresis occurs at the same annealing temperature as the optimum performance, 180 °C, as shown in Figure 3.4.

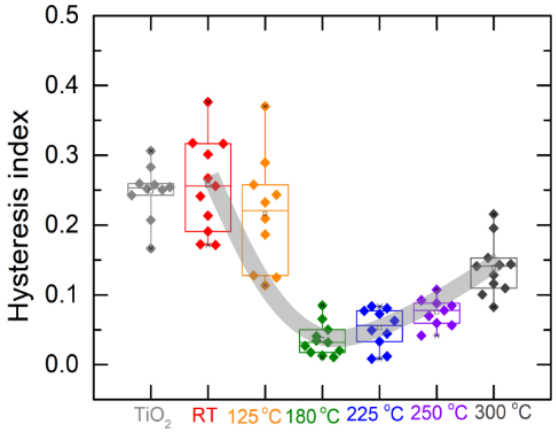

Figure 3.4 HI of the solar cells fabricated on SnO_x annealed at different temperatures (9-11 devices for each annealing temperature). The grey line is a visual aid to interpret the trend of the results.

Furthermore, we have characterized the solar cells comprising TiO_2 and SnO_x (annealed at 180 °C) as ETL at different scan rates (Figure 3.5). We found for both architectures that the PCE increases while the HI decreases with an increase in scan rate. This behavior is attributed to the charge carrier collection efficiencies at different scan rates which depend on ion accumulation at the interfaces.[14]

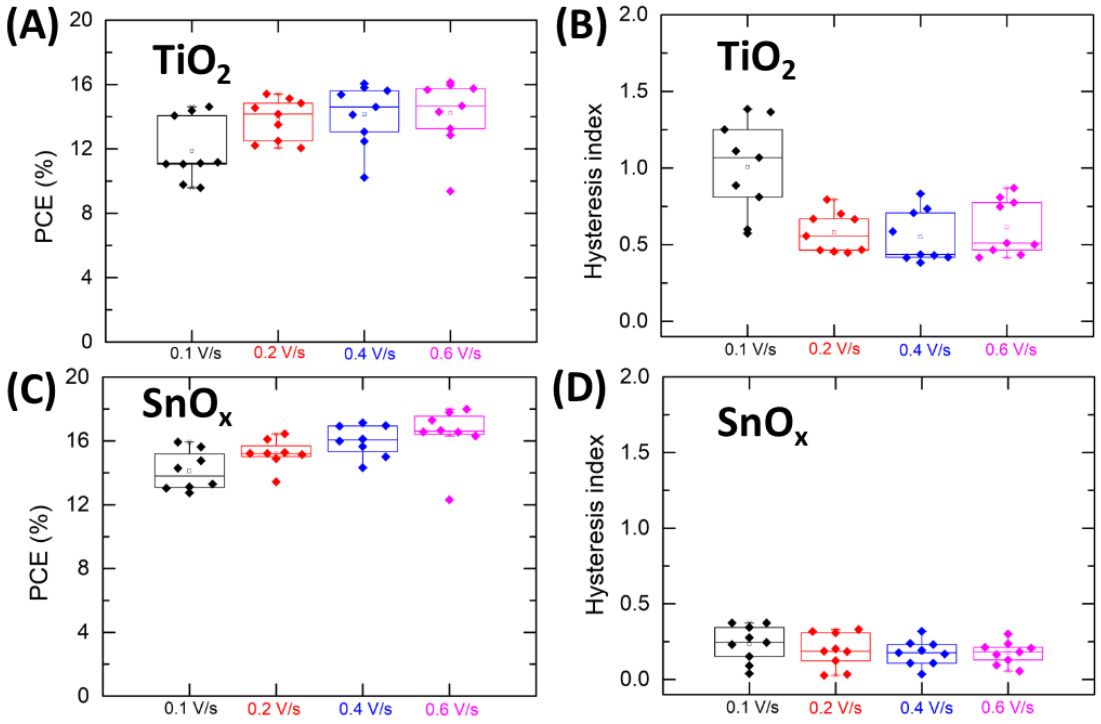

Figure 3.5 (A) and (B) show the PCE and HI of the solar cells on TiO_2 while (C) and (D) demonstrate the PCE and HI of the solar cells on SnO_x annealed at 180 °C at different scan rates, respectively.

3.3 Determination of Fermi Levels of ETL and Perovskite

To understand the observed trends in device performance and to gain insight into the effect of thermal annealing on SnO_x, we first determined the band alignment between the ETL and the perovskite by measuring the work function of both in ultrahigh vacuum via UPS (Figure 3.6). The valence band maximum (VBM) was found by a linear extrapolation of the leading edge of the valence band spectra (Figure 3.6B). The conduction band minimum (CBM) was determined by subtracting the band gap energies of SnO_x, which do not change at different annealing temperatures and which were estimated via Tauc plots of absorbance measurements (Figure 3.7). The Fermi levels were extracted by subtracting the value found by a linear extrapolation of the secondary electron edge from *hv* (Figure 3.6A). Further experimental and evaluation details of UPS measurements are given in the Experimental Section. Our results show that both the SnO_x and perovskite show n-type character with very little gap between their Fermi level and CBM, considering that UPS analyzes only the surface properties. Figure 3.6 shows a schematic diagram of the band alignment between the ETL and perovskite in the solar cells, where we obtained

different Fermi levels (dashed black lines below CBM) from different annealing temperatures of SnO_x.

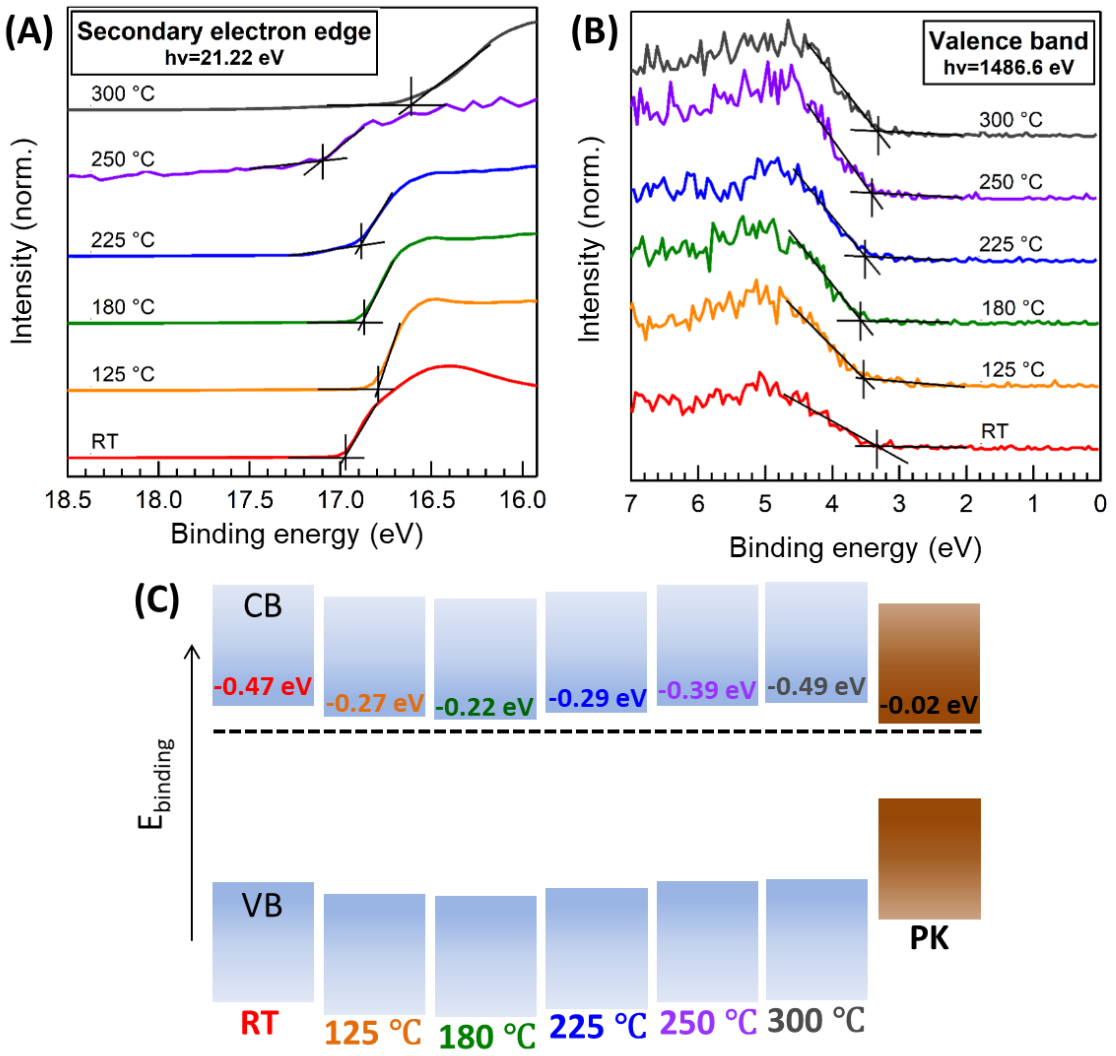

Figure 3.6 Linear fits of (A) secondary electron edge (SEE) and (B) valence band maximum (VBM) of SnO_x from UPS and XPS measurements, respectively. (C) Schematic diagram of the energy bands of the ETL and perovskite. The temperatures at the bottom of the band diagram are the annealing temperatures of the SnO_x layers. The energy levels are aligned according to Fermi level. (CB, VB and PK are conduction and valence band, and perovskite respectively. Dashed black line represents the Fermi level.)

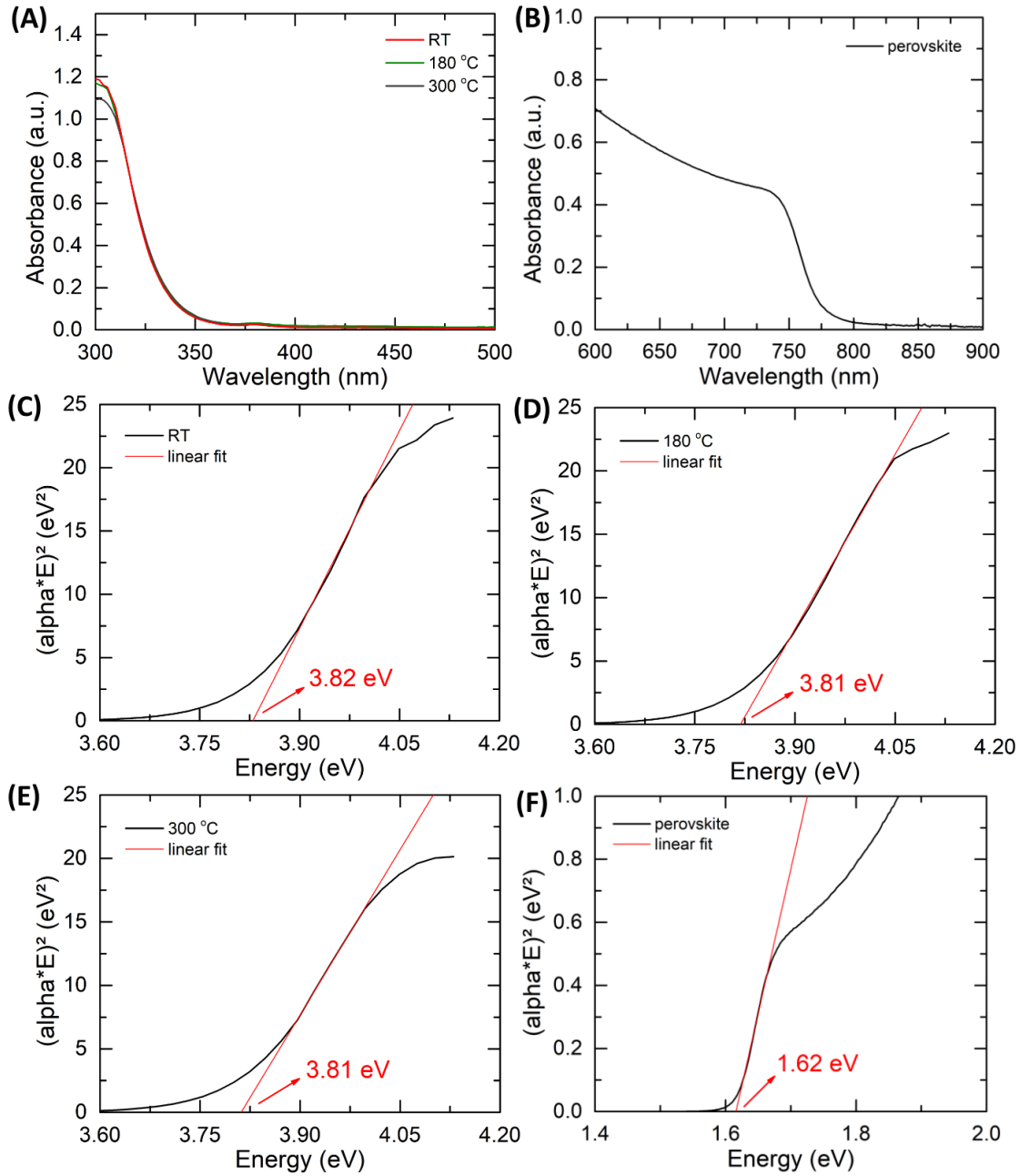

Figure 3.7 Absorbance spectra of (A) SnO_x layers and (B) perovskite. Tauc plots of SnO_x layers (C) without annealing, (D) 180 °C and (E) 300 °C and (F) perovskite.

UPS measurements highlight a remarkable connection: The smallest energetic distance between Fermi level and CBM corresponds to the lowest HI. Samples annealed at 180 °C, which demonstrate the highest PCE and lowest HI, exhibit the smallest energy offset between the Fermi level and CBM of 0.22 eV. When compared to the Fermi level of the perovskite, it can be seen that the annealing at 180 °C results in the best energy alignment since the Fermi level of SnO_x is the closest to the CBM of the perovskite, whereby the photogenerated electrons can be efficiently

extracted into the SnO_x layer. At annealing temperatures below or above 180 °C, the Fermi level shifts further away from the respective CBM, where lower PCEs and higher HI values were obtained due to the inefficient charge collection.

The change in Fermi level energy can be explained by means of the defect states formed in the metal oxide layer. In a semiconductor, the work function of the material is defined not only by the band structure and the density of states of the pristine material, but also by defects which causes charge carrier trap states within the band gap. Therefore, it is likely that the SnO_x used in this work is defect-rich since the films are not crystalline (Figure 3.8). In fact, Du *et al.* have shown that the oxygen vacancy defect in TiO_2 causes deep defect levels located 0.4-1.18 eV below the CBM of TiO_2.[18] Analogously, the defects in SnO_x layers are attributed to oxygen vacancies,[19-20] leading to similar defect distributions below the CBM. Therefore, changing the density and depth of the trap states in the semiconductor allows for Fermi level tuning, which in our case can be achieved by thermal annealing in air.[21]

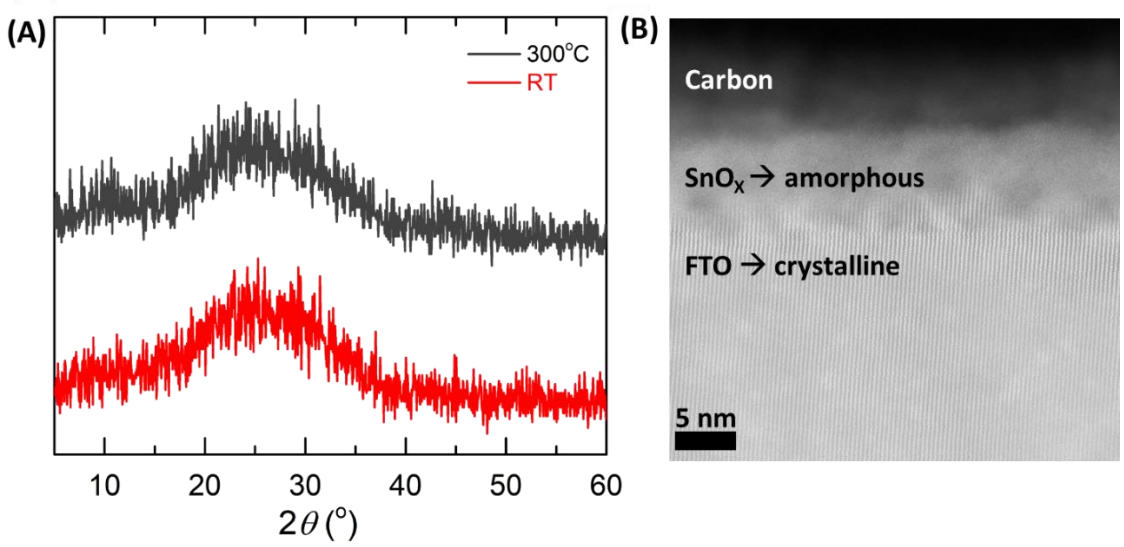

Figure 3.8 (A) XRD pattern of SnO_x layers on glass. (B) Annular dark field – STEM image of a cross-section of FTO/SnO_x annealed at 300 °C.

3.4 Trap Landscape at the Interface between ETL-Perovskite

To fully understand this connection, we investigated the energetic trap landscape in devices fabricated with different SnO_x films via TSC[22] measurements, which we applied successfully to PSCs in previous work.[23-24] As TSC is performed on fully processed solar cells (as described above), it enables probing of electronic trap states and allows linking the results directly to the device performance. The devices are first cooled down to very low temperatures (here: 30 K) in

dark conditions. The illumination with white light LED then generates free charge carriers without heating the solar cell. After the light is turned off, charge carriers relax into the deepest trap states during a certain dwell time. During this limited timeframe, charge carriers populate available trap states in the bulk and at the interfaces with the charge extraction layers. Due to the low thermal energy available, the charge carriers cannot be released from these states. Subsequently, the device is heated up to room temperature at a constant rate (here: 3 K/min), which initiates a gradual release of the trapped charges as soon as they gain enough thermal energy to escape. The current flow originating from trap release is precisely monitored and is used to determine the trap depth as well as density of the electrically active defect states in the probed system. Further details on the measurements technique can be found elsewhere.[23]

Figure 3.9 shows the resulting TSC signals for solar cells, where the SnO_x ETL was annealed at temperatures of up to 225 °C. Starting at approximately 180 K, a strong current was detected in all investigated devices, with a distinct shoulder at around 240 to 250 K (marked by shaded area). The TSC signal is the largest for the device with the non-annealed SnO_x layer (Figure 3.9A, red curve) and it dramatically decreases upon annealing of the SnO_x layer with a minimum in TSC signal for the 180 °C-annealed device, for which we observed also the best device performance and minimum HI. We note that for higher temperatures than 225 °C, the occurrence of leakage current due to a decrease in shunt resistance prevented reliable detection of very small TSC signals. As the layout is identical for all devices studied, we ascribe the decrease in TSC signal to a reduction in the density of trap states in the ETL or at the ETL-perovskite interface. Interestingly, the density of traps increases again for devices with SnO_x above the annealing temperature of 180 °C. This increase in trap density could be due to the surface of SnO_x annealed at higher temperatures which might trigger the formation of perovskite decomposition products.[2]

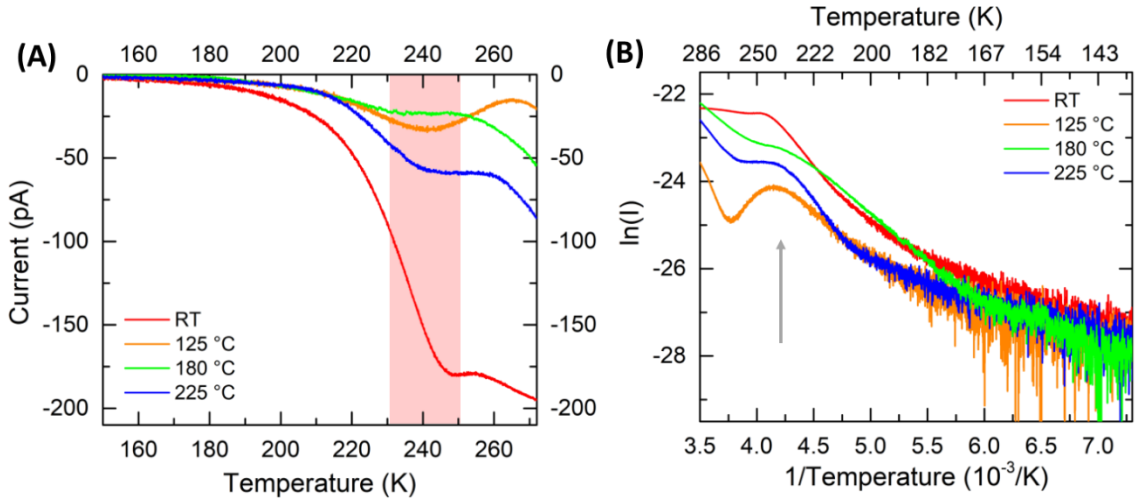

Figure 3.9 (A) TSC signals of solar cells fabricated on SnO_x annealed at different temperatures. (B) Corresponding Arrhenius plot of the TSC signals with the activation energy peak marked with an arrow for all devices.

To extract the activation energy of the trap states, the slope of the initial rise of the TSC current, which was attributed to the start of trap release, is fitted in the Arrhenius plot (Figure 3.9B) for each annealing temperature according to the following equation:

$$I_{TSC} \propto exp\left(-\frac{E_A}{k_B T}\right)$$

where E_A, k_B, and T are the activation energy, Boltzmann constant and temperature, respectively.[25-26] The values of the activation energies to release electrons from trap states are summarized in Table 3.1. These energies follow a remarkably similar trend with one we observed in UPS measurements as well as for the HI: The activation energy decreases with increasing annealing temperature, where a significant drop is observed from 275 (non-annealed ETL) to 202 meV for ETLs annealed at only 125 °C. The activation energy of the trap states reduces further to 187 meV with annealing of the SnO_x layer at 180 °C. Interestingly, for annealing temperatures above 180 °C, the trend reverses, showing even higher activation energy (307 meV) than the non-annealed sample.

Table 3.1 The activation energies to detrap electrons from the traps according to annealing temperatures of SnO_x layers.

Annealing temperature (°C)	Trap depth energy (eV)
RT	0.275
125	0.202
180	0.187
225	0.307

3.5 Discussion

The results from UPS and TSC, summarized in Figure 3.10 are in noticeably good agreement: Annealing of as-prepared SnO_x films leads to a significant reduction in the trap density as well as energetic depth of the trap states in the ETL or at the ETL-perovskite interface, resulting in a shift of the ETL Fermi level closer to the CBM. Particularly, we find the trap depth plays a significant role in charge accumulation at the interface since charge transport in metal oxides such as the SnO_x layers relies on a trapping-detrapping mechanism.[27] The photogenerated electrons are transferred from the absorber into the SnO_x layer where they relax and localize in sub-band gap states. Electron transport then occurs *via* thermal detrapping, diffusion in the conduction band and again retrapping. In this way, charge transport is limited by the detrapping events, which is highly dependent on the energetic depth of the trap state.[27] Ultimately, the highest PCE and lowest HI are found for the solar cell with the ETL annealed at a temperature of 180 °C, where the shallowest trap states result in the best Fermi level matching. Additionally, we point out that these trap states in SnO_x are unlikely to cause a light-soaking effect in PSCs. This effect has previously been assigned to light-induced ion/defect migration in the perovskite lattice.[28] In fact, in other solar cell systems, UV-light soaking effects are reduced when TiO_2 is exchanged by SnO_x.[29]

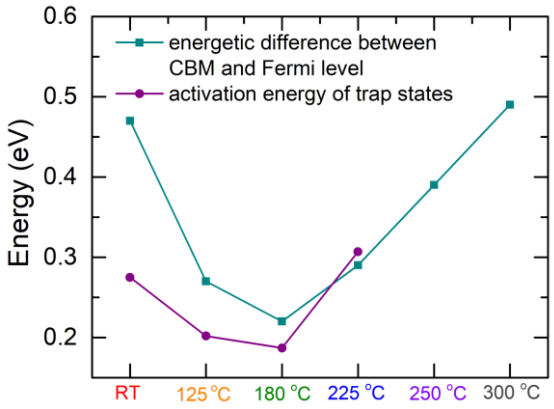

Figure 3.10 Comparison of energetic difference between CBM and Fermi level of SnO_x and trap depth energies of solar cells.

Based on this, we propose that charge accumulation occurs at the interface and is determined by the energy gap between the electron acceptor's Fermi level and its CBM. Essentially, deeper traps, given by the Fermi level position in the SnO_x layer, cause more charge accumulation at the interface between ETL and perovskite due to the lack of available thermal energy required to release electrons from these states. This, in turn, leads to enhanced recombination as can be observed by (i) an increase in HI (Figure 3.4) and (ii) V_{oc} (Figure 3.3E), which is in good agreement with literature.[6, 30] Furthermore, the stabilized power output demonstrates that the solar cells with a high HI show a larger loss in performance than those one with a lower HI (Figure 3.3C).

3.6 Conclusion

In this work, we unveil the influence of Fermi level alignment between the SnO_x ETL and perovskite absorber as well as associated trap depth on the PCE and hysteresis of PSCs. We were able to tune the Fermi levels of ALD SnO_x layers by thermal annealing. We obtained the maximum PCE and the smallest HI at the optimum annealing temperature of 180 °C. We find a strong correlation between the Fermi level positions of SnO_x and the trap depth deduced from the UPS and TSC measurements, respectively: Based on the trapping-detrapping charge transport mechanism in SnO_x layers, deep trap states likely trigger charge accumulation at the interface, which in turn leads to enhanced charge recombination at the SnO_x-perovskite interface, causing a higher HI in solar cells. Therefore, a decrease in the trap energy, partially eliminating trap states in the ETL or at the ETL - absorber interface, results in a better Fermi level alignment and hence in more efficient and hysteresis-free PSCs.

3.7 Experimental Section

3.7.1 Solar Cell Assembly

3.7.1.1 ETL preparation

Fluorine-doped tin oxide (FTO) coated glass substrates (<7 Ω/sq) were patterned by etching with zinc powder and HCl solution (3 M). The substrates were washed with deionized water and a 2% Hellmanex detergent solution. They were consecutively cleaned with deionized water, acetone and ethanol and dried by pressurized air. The substrates were further cleaned by oxygen plasma for 5 min. The compact TiO_2 layer was coated on the FTO substrates as an electron transport layer via a sol-gel approach. For this, a mixture containing dried 2-propanol (2.5 mL) and 2 M HCl (35 µL) was added drop-wise into a mixture of dried 2-propanol and titanium(IV) isopropoxide (Sigma Aldrich, 367.5 µL) under vigorous stirring. The TiO_x solution was filtrated through a 0.45µm syringe filter and spin-coated on the oxygen plasma cleaned FTO substrates at 2000 rpm for 45 s, followed by annealing at 150 °C for 10 min and subsequently at 500 °C for 45 min.

SnO_x ETLs were prepared by ALD on FTO coated glass substrates which were patterned and cleaned as in the TiO_x preparation. Tetrakis(dimethylamino)tin (IV) (TDMASn, Strem, 99.99%) was used as a tin precursor. The deposition was conducted at 118 °C with a base pressure of 5 hPa in a Picosun R-200 Advanced ALD reactor. The precursor was held in a glass vessel at 75 °C. Ozone was produced by an ozone generator (INUSA AC2025). Nitrogen (99.999%, Air Liquide) was used as the carrier gas and purge gas with a flow rate of 50 sccm. The growth rate measure, determined by ellipsometry on Si (100) substrates placed next to the FTO during depositions, was 0.69 Å/cycle. The Cauchy model was used for the SnO_x layer.

Ozone gas: 1% N_2 in O_2 (99.995%, Air Liquide)
Ozone generator: INUSA AC2025, power setting 50%, flow rate 500 sccm pulse parameters:
TDMASn: 2 pulses per cycle, pulse time 1.6 s, purge time 4s/10s,
Ozone: 1 pulse per cycle, pulse time 10 s, purge time 5 s,
Non-uniformity (200 mm wafer): 3.2 %

3.7.1.2 Perovskite deposition

The organic cations methylammonium bromide (MABr) and formamidinium iodide (FAI) were purchased from Dyesol and cesium iodide (>99%) from Sigma Aldrich. The lead iodide and bromide were purchased from TCI. All chemicals were used without any further purification.

$Cs_{0.05}(FA_{0.83}MA_{0.17})_{0.95}Pb(I_{0.83}Br_{0.17})_3$ perovskite was prepared according to the published report by Saliba *et al*.[17] A triple cation mixed halide perovskite was synthesized by mixing PbI_2 (507.1 mg, 1.1 mmol), $PbBr_2$ (73.4 mg, 0.2 mmol), FAI (171.97 mg, 1 mmol) and MABr (22.4 mg, 0.2 mmol) in 1 mL of a 4:1 (v/v) mixture of anhydrous DMF (Sigma Aldrich) and DMSO (Sigma Aldrich). This mixture was heated up to 100 °C in order to dissolve the solids completely. The CsI (389.72 mg, 1.5 mmol) was dissolved in anhydrous DMSO at 100 °C. After both solutions were cooled down to room temperature, 42 µL of CsI solution was added to the previous mixture in order to obtain a 5% Cs content in the desired perovskite mixture. The solution was filtered through a 0.45 µm syringe filter before use.

The perovskite deposition was carried out in a nitrogen-filled glove-box. The prepared perovskite solution was deposited in a two-step spin-coating procedure, 1000 rpm for 10 s and 6000 rpm for 20 s, respectively. In the last 5 s of the second-step, 500 µL of anhydrous chlorobenzene (CB, Sigma Aldrich) was dripped onto the film. The films were annealed at 100 °C for 1 h on a hotplate.

3.7.1.3 Hole transporter layer and back electrode deposition

2,2',7,7'-tetrakis-(*N*,*N*-di-*p*-methoxyphenyl-amine)-9,9'-spirobifluorene (75 mg, spiro-OMeTAD, Borun Chemicals, 99.8%) was dissolved in 1 mL of anhydrous chlorobenzene and filtered through a 0.45 µm syringe filter. Later, this solution was doped with 10 µL 4-*tert*-butylpyridine (Sigma-Aldrich, 96%) and 30 µL of a 170 mg/mL lithium bistrifluoromethanesulfonimidate (Li-TFSI) (Sigma-Aldrich, 99.95%) solution dissolved in anhydrous acetonitrile (Sigma-Aldrich). This solution was deposited by spin-coating at 1500 rpm 40 s and 2000 rpm 5 s in a nitrogen-filled glove-box. The samples were stored in air at a relative humidity of 25-30%. 40 nm of Au was deposited as a back electrode by thermal evaporation at $9 \cdot 10^{-7}$ mbar.

3.7.2 Solar cell characterization

Current-Voltage (*J-V*) curves were measured under ambient conditions using a Newport OrielSol 2A solar simulator with a Keithley 2400 source meter under simulated AM 1.5G sunlight, with an incident power of 100 mW cm^{-2}, calibrated with a Fraunhofer ISE certified silicon cell (KG5-filtered). The active area of the solar cells was defined by a square metal aperture mask of 0.0831 cm^2. *J-V* curves were recorded by scanning the input bias from 1.5 V to 0 V (reverse scan) and then from 0 V to 1.5 V (forward scan) at a scan rate of 0.2 V/s after the devices had been at 1.5 V for 5 s under illumination. The stabilized power output was measured by tracking the photocurrent at the maximum power point without pre-biasing the device. To obtain the EQE spectra, the respective solar cell was illuminated with the chopped light of a tungsten lamp, split into its

wavelength components with the help of a monochromator. The light beam is further split to hit the sample as well as a reference silicon photodetector (Hamamatsu S2281-01) at the same time. The resulting wavelength dependent current response of both devices is recorded simultaneously by two lock-in amplifiers (Signal Recovery 7265, Stanford Research Systems 830) at a chopping frequency of 14Hz. The incident illumination power, determined via the reference photodetector, is used to calculate the EQE response of the perovskite solar cell.

3.7.3 Ultraviolet Photoelectron Spectroscopy (UPS)

3.7.3.1 Experimental details

Photoemission spectroscopy data were acquired at an ESCALAB 250 system by Thermo Fisher under UHV conditions (~10^{-9}mbar). A monochrome X-ray source with Al-Kα 1486.6 eV with a FWHM of 0.25 eV was used for the XPS measurements. A helium discharge lamp was used as an excitation source for the UPS measurements. The He Lα line (21.22 eV) was used for the secondary edge as well as for spectra of the valence band region. The sample was grounded to the analyzer and the energy scale was calibrated to the Fermi-edge of a sputtered metallic silver sample, $Ag3d_{5/2}$ of 368.26 eV and $Cu2p_{3/2}$ of 932.67 eV. The emission in the normal direction was characterized. The concentric hemispherical analyzer was set to a pass energy of 10 eV for XPS and 2.5 eV for UPS measurements. To reinforce the secondary electron edge for the determination of the work function, a bias voltage of 4 eV was applied between the sample and the analyzer.

3.7.3.2 Analysis details

The spectrometer was calibrated in such a manner that the Fermi-energy is located at 0 eV of binding energy. The energetic position of the valence band maximum therefore represents the distance to the Fermi-level. The valence band maximum was determined by a linear extrapolation of the leading edge of the valence band spectra. The trends in the position of the valence band maxima were also found in the binding energy of the core-level emissions namely Sn 3d and O 1s. The conduction band minima were calculated by subtracting the energy of the band gap from the position of the valence band maxima. To determine the value of the secondary electron edge, a linear function was fitted similarly to the procedure described for the valence band maximum. The energy, at which this line extrapolates to zero intensity, was considered as the secondary edge. The work function can be calculated by the formula $\phi=h\nu-SEE$.

3.7.4 Thermally Stimulated Spectroscopy (TSC)

The TSC measurements were conducted in a closed cycle He cryostat. Trap filling was achieved via illumination of a cold white LED for 10 min at 30 K. The TSC signals were monitored with a

sub-femtoamp remote source meter (Keithley 6430) without applying any external bias to the device.

3.7.5 Film Characterization

SEM images were taken with a FEI Helios Nanolab G3 UC DualBeam scanning electron microscope, operated at an acceleration voltage of between 2 and 5 keV. STEM was performed in annular dark field mode on a probe-corrected FEI Titan Themis at 300 kV. Absorbance spectra were recorded using a PerkinElmer Lambda 1050 spectrophotometer equipped with a 150 mm integrating sphere. XRD measurements were performed with a Bruker D8 Discover X-ray diffractometer operating at 40 kV and 30 mA, employing Ni-filtered Cu $K_{\alpha 1}$ radiation (λ = 1.5406 Å) and a position-sensitive LynxEye detector.

3.8 References

1. Kojima, A.; Teshima, K.; Shirai, Y.; Miyasaka, T., *J. Am. Chem. Soc.* **2009,** 131, 6050-6051.
2. Hu, T., et al., *Adv. Mater.* **2017,** 29, 1606656.
3. http://www.nrel.gov/ncpv/.
4. van Reenen, S.; Kemerink, M.; Snaith, H. J., *J. Phys. Chem. Lett.* **2015,** 6, 3808-3814.
5. Snaith, H. J., et al., *J. Phys. Chem. Lett.* **2014,** 5, 1511-1515.
6. Calado, P.; Telford, A. M.; Bryant, D.; Li, X.; Nelson, J.; O'Regan, B. C.; Barnes, P. R. F., *Nat. Commun.* **2016,** 7, 13831.
7. Coll, M.; Gomez, A.; Mas-Marza, E.; Almora, O.; Garcia-Belmonte, G.; Campoy-Quiles, M.; Bisquert, J., *J. Phys. Chem. Lett.* **2015,** 6, 1408-1413.
8. Cai, F.; Yang, L.; Yan, Y.; Zhang, J.; Qin, F.; Liu, D.; Cheng, Y.-B.; Zhou, Y.; Wang, T., *J. Mater. Chem. A* **2017,** 5, 9402-9411.
9. Wojciechowski, K., et al., *ACS Nano* **2014,** 8, 12701-12709.
10. Peng, J., et al., *Energy Environ. Sci.* **2017,** 10, 1792-1800.
11. Zhang, P., et al., *Adv. Mater.* **2018,** 30, 1703737.
12. Yang, J.; Siempelkamp, B. D.; Mosconi, E.; De Angelis, F.; Kelly, T. L., *Chem. Mater.* **2015,** 27, 4229-4236.
13. Zhang, J.; Tan, C. H.; Du, T.; Morbidoni, M.; Lin, C.-T.; Xu, S.; Durrant, J. R.; McLachlan, M. A., *Sci. Bull.* **2018**.
14. Tress, W.; Marinova, N.; Moehl, T.; Zakeeruddin, S. M.; Nazeeruddin, M. K.; Gratzel, M., *Energy Environ. Sci.* **2015,** 8, 995-1004.
15. Shi, J.; Xu, X.; Li, D.; Meng, Q., *Small* **2015,** 11, 2472-2486.
16. Correa Baena, J. P., et al., *Energy Environ. Sci.* **2015,** 8, 2928-2934.
17. Saliba, M., et al., *Energy Environ. Sci.* **2016,** 9, 1989-1997.
18. Du, Y. y., et al., *Phys. Chem. Chem. Phys.* **2017,** 19, 13679-13686.
19. Xie, J., et al., *ACS Nano* **2017,** 11, 9176-9182.
20. Godinho, K. G.; Walsh, A.; Watson, G. W., *J. Phys. Chem. C* **2009,** 113, 439-448.
21. Henrich, V. E.; Cox, P. A., *The Surface Science of Metal Oxides*. Cambridge University Press: 1996.
22. Haering, R. R.; Adams, E. N., *Phys. Rev.* **1960,** 117, 451-454.
23. Baumann, A.; Väth, S.; Rieder, P.; Heiber, M. C.; Tvingstedt, K.; Dyakonov, V., *J. Phys. Chem. Lett.* **2015,** 6, 2350-2354.
24. Yinghong, H., et al., *Adv. Energy Mater.* **2018,** 8, 1703057.

25. Graupner, W.; Leditzky, G.; Leising, G.; Scherf, U., *Phys. Rev. B* **1996,** 54, 7610-7613.
26. Garlick, G. F. J.; Gibson, A. F., *Proc. Phys. Soc.* **1948,** 60, 574.
27. Docampo, P.; Guldin, S.; Steiner, U.; Snaith, H. J., *J. Phys. Chem. Lett.* **2013,** 4, 698-703.
28. Mosconi, E.; Meggiolaro, D.; Snaith, H. J.; Stranks, S. D.; De Angelis, F., *Energy Environ. Sci.* **2016,** 9, 3180-3187.
29. Trost, S.; Behrendt, A.; Becker, T.; Polywka, A.; Görrn, P.; Riedl, T., *Adv. Energy Mater.* **2015,** 5, 1500277.
30. Tress, W., *Adv. Energy Mater.* **2017,** 7, 1602358.

4 Charge Transport Limitations in Perovskite Solar Cells: The Effect of Charge Extraction Layers

This chapter is based on the following publication:

Irene Grill, Meltem F. Aygüler, Thomas Bein, Pablo Docampo, Nicolai F. Hartmann, Matthias Handloser, and Achim Hartschuh, *ACS Applied Materials and Interfaces*, 2017, 9, 37655-37661

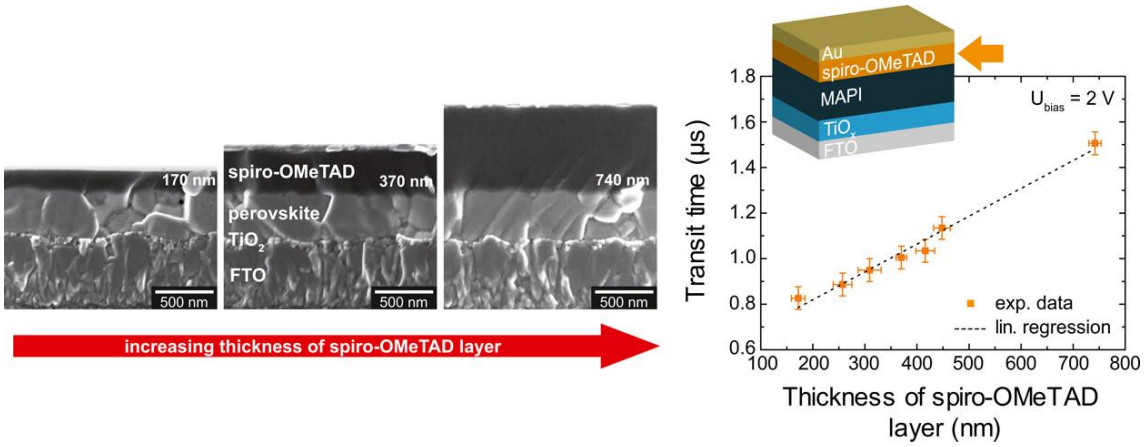

Keywords

Charge carrier mobility, charge extraction layer, hybrid perovskites, photocurrent, solar cells, thin films

4.1 Introduction

Hybrid organometal halide perovskites, a class of materials revealing outstanding optoelectronic properties including large absorption coefficients[1] and easily tunable band gaps[2], have undergone a rapid development[1, 3] toward particularly promising candidates for integration into photovoltaic devices.[4-5] Facile solution processing at low temperatures and the use of cheap and abundant precursor compounds[6-7] combined with power conversion efficiencies (PCEs) surpassing 21%[8] make organic−inorganic perovskites competitive with modern technologies, for example, copper indium gallium selenide or silicon.[9] Among a variety of possible material combinations and device architectures,[10-11] the state-of-the-art layout for planar n−i−p perovskite solar cells comprises the small organic molecule spiro-OMeTAD as the hole transporter and compact TiO_x as the hole-blocking layer.[12] However, these charge extraction materials can introduce some challenging issues to the stacked system. Spiro-OMeTAD, for instance, is known to be unstable and suffers from degradation processes[13-14], whereas TiO_x has been suggested to contribute to the hysteretic $J-V$ behavior.[15-16] Thus, the examination of the physical processes determining and limiting the charge transport properties is essential to balance material suitability (in terms of stability or production costs) and optoelectronic performance, both being key aspects on the way toward further development of high-efficiency solar cells.

In this work, we present a detailed study of the charge carrier mobilities, playing an important role in charge carrier transport properties in devices in general, in both perovskite thin films and stacked solar cells based on methylammonium lead triiodide (MAPI). From time-of-flight (ToF) photocurrent measurements, we determine mobilities of approximately 6 cm^2/Vs for electrons and holes in MAPI films derived from a one-step deposition approach, whereas we extract mobilities being decreased by 3 orders of magnitude. By tuning the thicknesses of the hole-transporting material (HTM) and of the electron-transporting material (ETM), we find that the transport time of photoinduced charge carriers under a constant external bias does not reflect the transport characteristics of the MAPI film but is mainly determined by the charge-selective layers.

4.2 Results and Discussion

Pristine MAPI films and thin MAPI absorber layers incorporated in photovoltaic devices were derived from a previously published synthesis protocol describing a fast deposition−crystallization (FDC) procedure[17] (see Experimental Section for further details). Scanning electron micrographs of FDC-derived MAPI (Figure 4.1A) grown on fluorine-doped tin

oxide (FTO)-coated glass substrates confirm a high surface coverage of large crystals with few grain boundaries and without pinholes, resulting in visually smooth films.

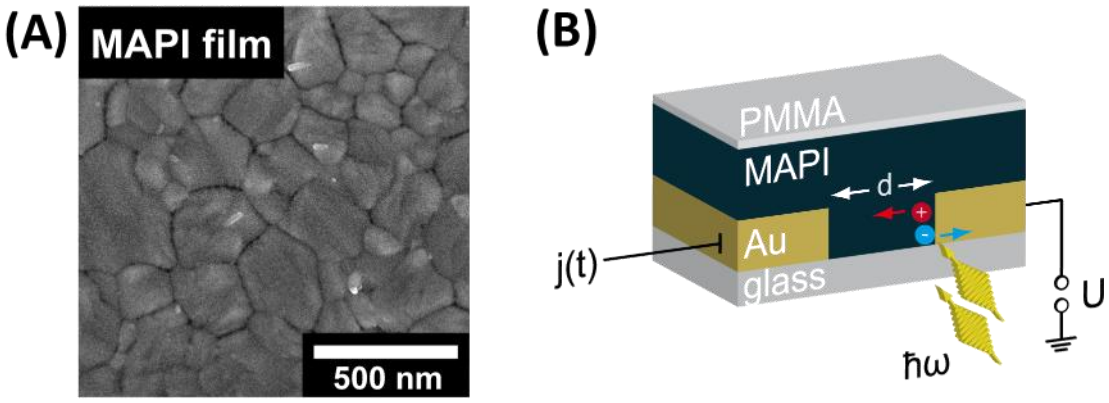

Figure 4.1 Schematic illustration of the employed sample layout and the experimental setup. (A) SEM micrograph showing a top view of the investigated MAPI thin film. (B) Schematic of the laterally contacted perovskite thin film with varying spacings d between the electrodes.

To identify the absorber material-related properties affecting the charge transport in perovskite-based solar cell devices, we first focused on charge carrier mobilities in the pure $CH_3NH_3PbI_3$ film. For this purpose, the MAPI thin film was deposited on top of laterally arranged metallic contacts with an electrode spacing d in the range of several micrometers, as shown in Figure 4.1B. To protect the moisture-sensitive perovskite from degradation in air, the samples were topcoated with a thin layer of poly(methyl methacrylate) (PMMA), thus permitting experiments under ambient conditions. This architecture allows for photocurrent measurements at different charge carrier travel distances through the film via the ToF measurement technique.

In brief, charge carriers are generated in the perovskite layer upon photoexcitation provided by a pulsed laser. The created charge carriers are separated by an applied direct current (dc) voltage and start moving toward the corresponding electrodes, thus creating a current, which is recorded with an oscilloscope. Because the charge carriers are locally created near one electrode, the polarity of the applied voltage determines whether the contribution of electrons or holes to the photocurrent extracted at the opposite electrode is observed. Further experimental details can be found in Experimental Section. Figure 4.2A depicts the obtained timeresolved photocurrent traces for different electrode distances after pulsed excitation at 540 nm and a pulse duration of 7 ns. Because ionic migration within the perovskite film is anticipated and can affect the current flow, the dc field at 5 kV/cm was applied only for a short measurement period of single seconds to mitigate this influence. Because the observable influence of ion migration in electrical

measurements, that is, photocurrent transients, is known to occur in the timeframe of several minutes[18-20], we do not expect this to affect the investigated system significantly.

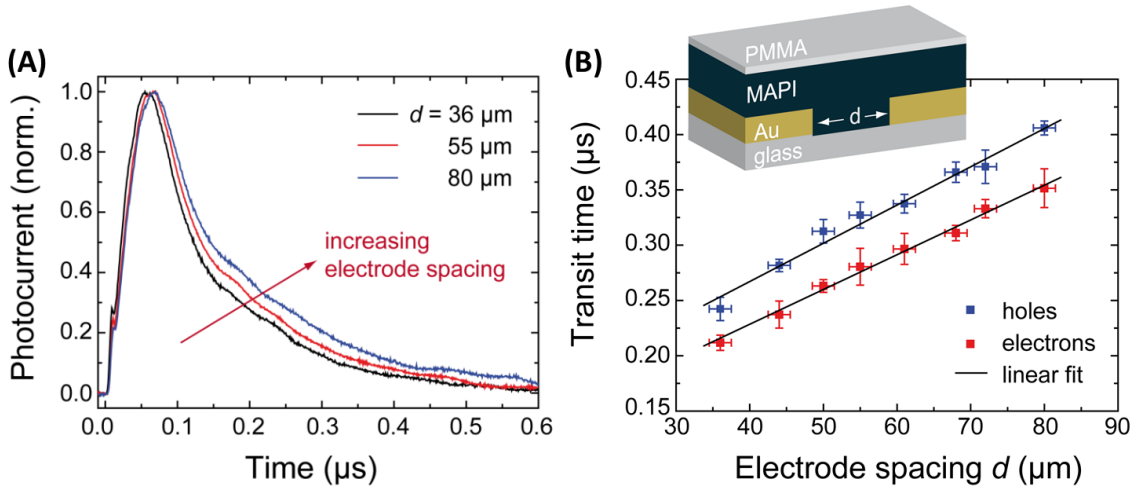

Figure 4.2 Extraction of the charge carrier mobility in the perovskite layer from photocurrent experiments in the lateral configuration. (A) Timeresolved photocurrent transients for three different electrode spacings obtained upon focused illumination close to one contact under dc biasing at 5 kV/cm. (B) Extracted transit times for holes and electrons as a function of electrode spacing. t_{tr} scales linearly with the corresponding electrode distance, allowing for the determination of μ and resulting in a value of 5.8 ± 0.3 cm^2/Vs for holes and 6.3 ± 0.2 cm^2/Vs for electrons.

The shapes of the $j-t$ profiles seen in Figure 4.2A indicate dispersive transport which could follow from a hopping behaviour of charge carriers. For this reason, we employed the analysis procedure introduced by Scher and Montroll[21] which has been applied to dispersive transport in a number of different materials including amorphous silicon and organic materials.[22] In general, dispersive transport is understood to result from spatially varying hopping rates due to energetic heterogeneities caused by trapped space charges. For perovskite systems, detailed studies by other groups have shown that transport is based on a hopping mechanism at room temperature, whereas it becomes band-like at low temperatures.[23-25]

The aforementioned procedure determines two linear fit functions for the plateau and the decay of the double logarithmic $j-t$ profile, whereas the transit time t_{tr} is defined by the point where they intersect (illustrated in Figure 4.3). To enhance the reproducibility of the determination of t_{tr}, a fit routine was programmed based on the iterative modeling of the slopes of pre- and posttransit linear functions close to the point of interest in the transient. According to the expression

$$\mu = \frac{d}{E \cdot t_{tr}} \tag{4.1}$$

with *d* being the interelectrode distance and *E* being the applied electric field, the average charge carrier mobility is obtained by linearly fitting the curve relating the transit time with the electrode spacing (Figure 4.2B). The linear dependence of the transit time t_{tr} on the electrode spacing *d* is visible in Figure 4.2A, B, reflecting the respective distance the carriers need to travel to the distal electrode after being created by focused laser excitation at the other electrode. As described by the model in eq 4.1, the slope of the linear regression allows for the determination of the charge carrier mobility in the MAPI film and results in $\mu_{MAPI,h^+} = 5.8 \pm 0.3$ cm^2/Vs and $\mu_{MAPI,e^-} = 6.3 \pm 0.2$ cm^2/Vs. The applicability of the mobility equation is confirmed by applying different bias voltages for a fixed gap size. The corresponding experimental data can be found in Figure 4.4.

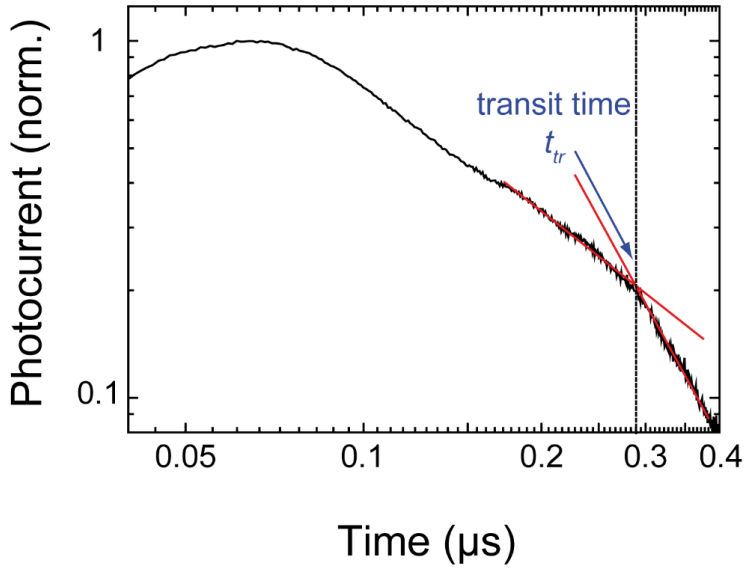

Figure 4.3 Fitting routine employed to extract t_{tr}.

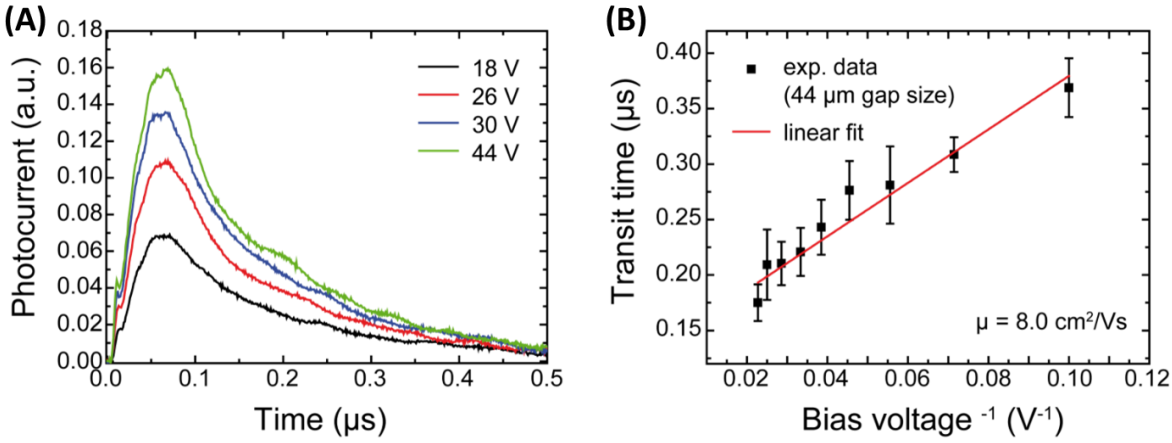

Figure 4.4 Voltage series for lateral devices as proof for the applicability of the mobility equation. (A) Representative transients for different applied bias voltages. (B) Extracted transit times as function of inverse applied bias voltage.

In the literature, different charge carrier mobilities have been reported for MAPI ranging from 3 cm^2/Vs to several tens of cm^2/Vs[26-29] using contactless measurement techniques including time-resolved microwave conductivity and terahertz spectroscopy. For contacted MAPI films on the other hand, field-effect transistor and Hall mobility measurements provide lower values between 0.5 and 8 cm^2/Vs.[30-32] The charge carrier mobilities obtained here for contacted films are well within the range of these values. In contrast to the contactless techniques mentioned above, which probe a rather local mobility, we determine the mobilities in lateral direction over several micrometers, where the influence of grain boundaries and defects, that is, potential trapping sites, becomes significant. To our knowledge, none of the optimized solution-processing techniques available at present[6, 17, 20] permit film thicknesses exceeding 300-500 nm; thus, the thickness dependence of the material cannot be studied in the vertical direction in a significant range.

To gain further insights into the transport processes of photoinduced charge carriers in working solar cell devices, we complemented our studies by investigating thin-film stacks incorporating the previously analyzed organolead halide perovskite material. With the MAPI film being sandwiched between spiro-OMeTAD and TiO_x as the hole transport layer (HTL) and the electron transport layer (ETL), respectively, and contact layers (gold and FTO), the illumination of the perovskite occurs from the transparent FTO side. A detailed description of the complete sample preparation procedure can be found in the Experimental Section.

In the following experiments, we focused on the effects of the charge extraction layers on the transit time of charge carriers for constant thickness of the absorber material while varying the thickness of the charge extraction layer. Cross-sectional scanning electron microscopy (SEM)

images of photovoltaic devices confirm the successful tuning of the thickness of the HTL spiro-OMeTAD (Figure 4.5A) ranging from 170 to 740 nm at constant TiO_x and MAPI thickness (70 and 360 nm, respectively). We note that the MAPI residues visible on the HTM layer (see, e.g., the second cross section in Figure 4.5A) result from cutting the solar cell shortly before performing the SEM measurement. These residues attach to the cross section and are not induced by a nonuniform deposition of the organic spiro-OMeTAD layer on the absorber material which could occur if the MAPI surface would be rough. Moreover, the MAPI film thickness seen in the SEM cross sections corresponds to the typical values deduced using atomic force microscopes or profilometers.[33-34]

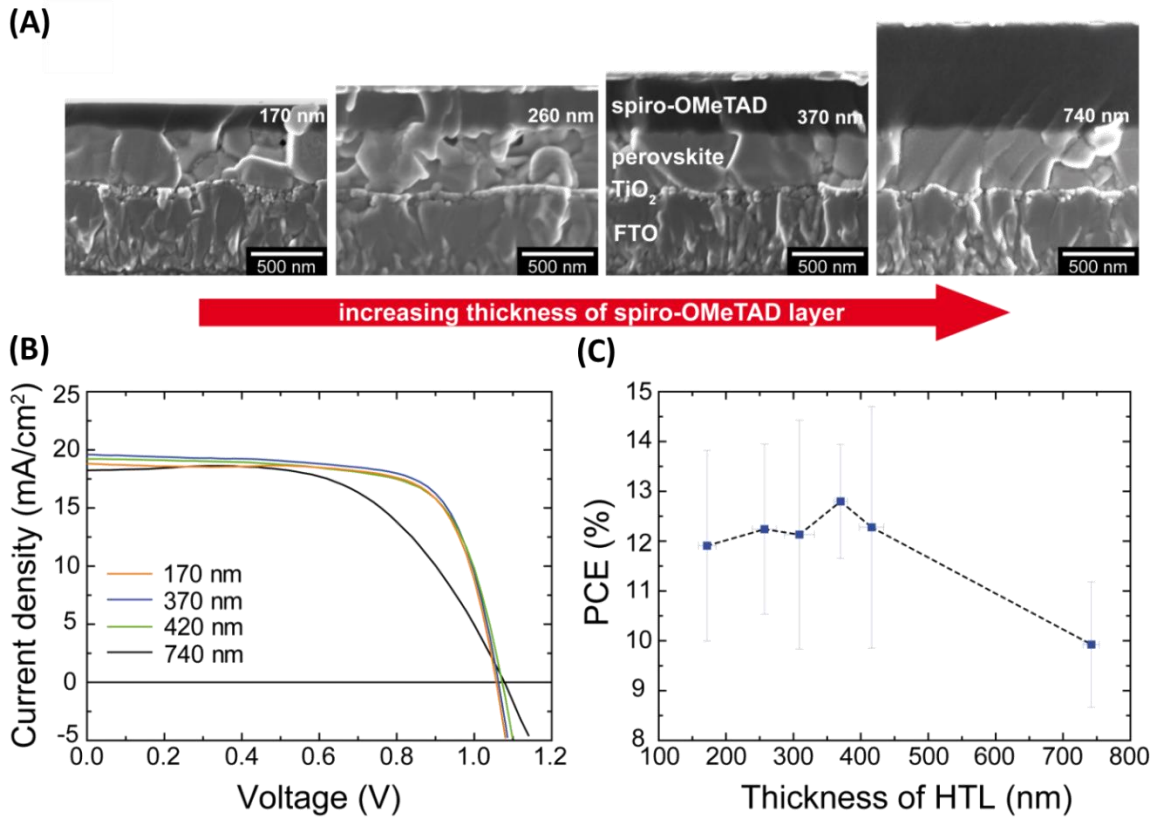

Figure 4.5 (A) Cross-sectional views of the stacks with varying layer thicknesses of the hole transporter spiro-OMeTAD. (B) *J*–*V* performance of working devices with different thicknesses of the HTL under simulated AM 1.5G illumination. (C) Statistical analysis of corresponding PCEs from more than 120 individual photovoltaic devices.

J–*V* analysis (Figure 4.5B) of this type of cells under simulated AM 1.5G illumination confirms proper operation characteristics with a typical deviation of ±2%. Furthermore, PCE statistics from more than a total of 120 solar cells indicate that the conversion of incident light to current reaches the best average performance value of 12.8 ± 1.14% for a HTL thickness of 370 nm (Figure 4.5C).

Comparable results have been obtained in a similar HTM study performed by Marinova et al.[35] where the authors observe the best $J-V$ performance for a spiro-OMeTAD thickness between 200 and 400 nm.

Equivalent measurements on photovoltaic devices with varying thicknesses of the ETL TiO_x as well as the corresponding cross sections of the samples and additional external quantum efficiency (EQE) data (highlighting that there is no significant contribution of the spiro-OMeTAD layer to the overall photocurrent) can be found in Figure 4.6 and Figure 4.7, respectively.

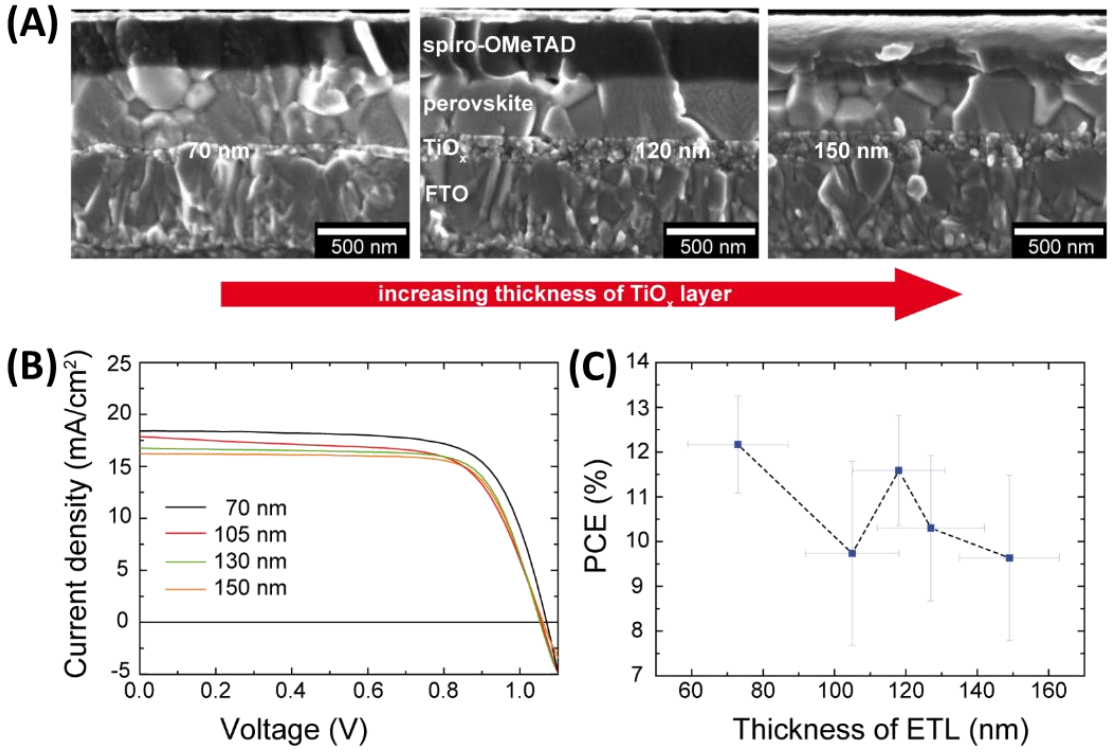

Figure 4.6 (A) Cross-sectional views of stacked solar cells with varying thickness of the ETL, TiO_x. (B) *J-V* performance data of photovoltaic devices with different thicknesses of the ETL under simulated AM 1.5G illumination. (C) Statistical analysis of corresponding PCEs from a total number of more than 100 individual solar cells.

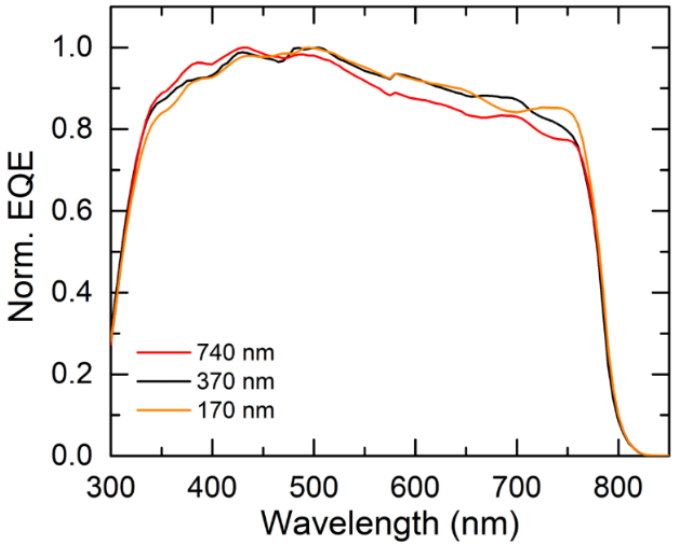

Figure 4.7 EQE curves for full devices at different spiro-OMeTAD thicknesses, showing that there is no significant contribution of the spiro-OMeTAD layer to the overall photocurrent. Small changes in the curves are due to the sample-to-sample variation.

We subsequently conducted photocurrent measurements on the stacked devices with varying thickness of HTL or ETL. For this purpose, the samples were illuminated from the transparent FTO side using an aperture mask with an active area of approximately 3 × 3 mm^2, identical with the illuminated area in the cell performance experiments. Figure 4.8A illustrates the $j-t$ profiles for the stacked devices with different spiro-OMeTAD layer thicknesses. The transit time was extracted by employing the same fitting routine which was used for the transients in the lateral configuration. To verify the applicability of eq 4.1 to the obtained data, the transit times at different applied bias voltages were plotted, as shown in Figure 4.8B. We note here that the hole transporter is not expected to substantially screen the electric field. Here, the oxidation of spiro-OMeTAD through the addition of LiTFSI, typically referred to as "Li doping", does not generate free carriers. Instead, the increased conductivity and mobility in spiro are attributed to the smoothing of the potential landscape which enhances the probability of intermolecular charge transfer.[36]

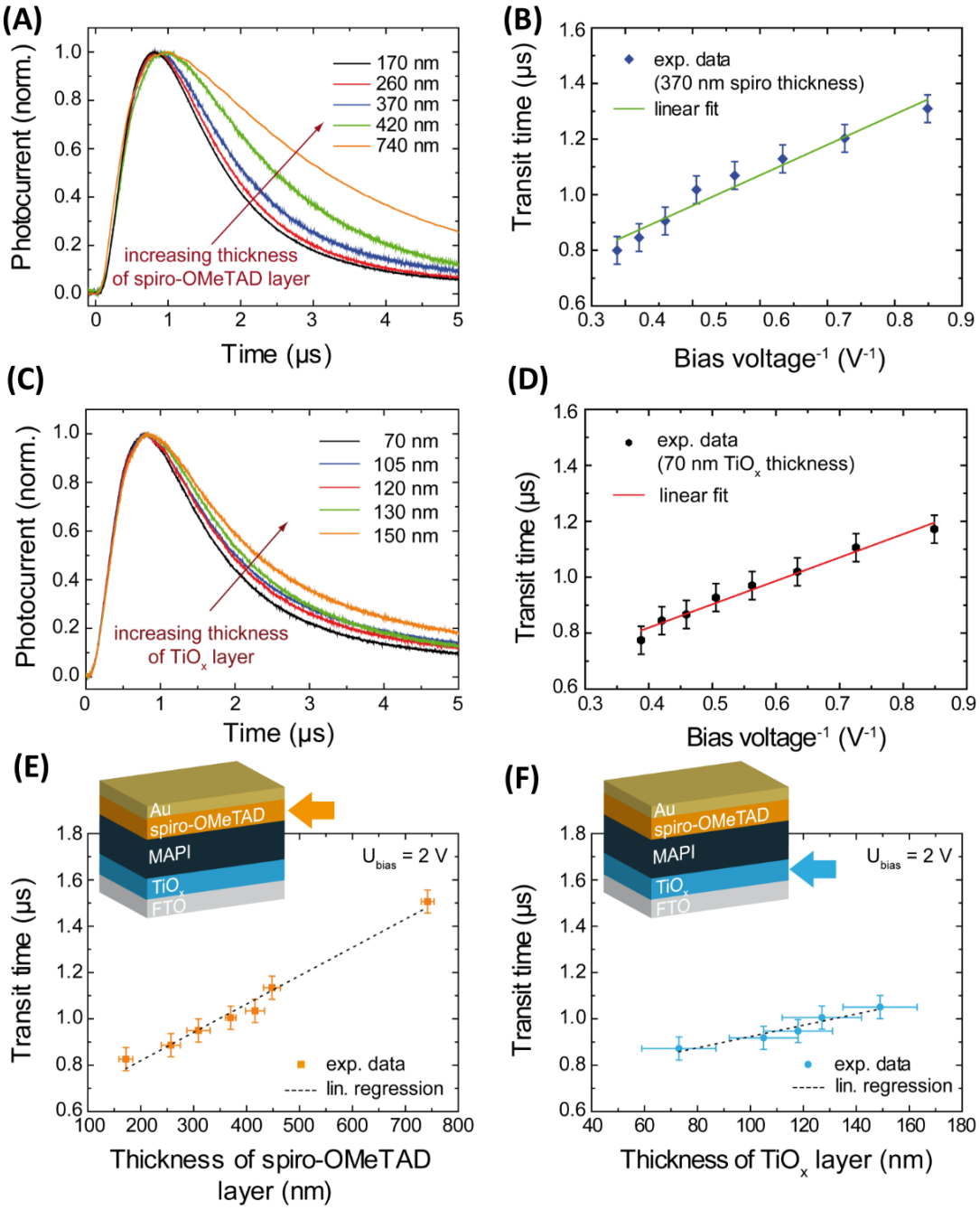

Figure 4.8 (A, C) Representative transients of photovoltaic devices (as shown in Figure 4.5) with varying thicknesses of the HTM spiro-OMeTAD and the ETM TiO_x, respectively. (B, D) Extracted transit times as a function of reciprocal applied bias voltage (values corrected for a fixed built-in voltage of 0.022 V) for a defined thickness of the HTL and ETL, respectively. (E) Transit times determined from the transients shown in (A) vs corresponding spiro-OMeTAD thicknesses. (F) Effect of the ETL (TiO_x) thickness on the transit of charge carriers across the stack.

From the slope of the linear regression relating t_{tr} and U_{bias} (values corrected for a fixed built-in voltage of 0.022 V as determined in ref 37) in Figure 4.8B, we derive a mobility of $\mu = (6.2 \pm 0.4) \times 10^{-3}$ cm^2/Vs (assuming $d = d_{ETL} + d_{MAPI} + d_{HTL}$). Several ToF experiments on perovskite-based solar cells have already been performed, resulting in a variety of obtained values for charge carrier mobilities, ranging from 4.6×10^{-5} and 5.4×10^{-4} cm^2/Vs[25, 38] to 0.06 and 1.4 cm^2/Vs.[37] This variety can most probably be assigned to different employed sample architectures as it is the case in refs 25 and 38 where inverted solar cell devices were investigated with different charge extraction materials (PEDOT:PSS and PCBM). Furthermore, the fabrication procedure for these absorber layers is based on either a two-step process,[25, 38] which results in smaller crystallites and affects the charge transport processes, or a one-step process employing different synthesis conditions such as varying antisolvents or annealing conditions.[37] The evaporation of differing metallic contacts (Al[25, 38] or Ag[37] compared to Au in our study) may also contribute to these varying mobility values as well as the definition of *d*. In some reports, *d* was taken as the thickness of the active absorber layer only, whereas in the present analysis, we considered transport through all layers up to the contact which consequently results in an increase in the respective charge carrier mobility by about a factor of 4.6.

As seen in Figure 4.8, the transport of charge carriers is substantially influenced by the thickness of the HTL, which is reflected in larger t_{tr} values starting from 0.82 up to 1.51 µs for increased travel distances, ranging from 170 to 740 nm (Figure 4.8E). Additional ToF experiments on devices without a HTL and devices incorporating a very thin layer of MAPI can be seen in Figure 4.9. A similar effect is observed for increasing the ETL thickness (Figure 4.8F), where the transit time increases from 0.87 to 1.05 µs with thicknesses ranging from 70 to 150 nm. We note that the growth of the ETL on the rather rough FTO surface consequently leads to some variations in the thickness (Figure 4.6A), resulting in large error bars in the chart. Furthermore, the chemical fabrication process employed for the samples in these specific experiments does not allow the creation of uniform films below a certain thickness of approximately 60−70 nm; thus, our measurements include samples with ETL thickness exclusively above the minimal obtainable thickness. On the other hand, the minimum thickness of the spiro-OMeTAD layer is limited by the formation of pinholes to about 170 nm at which a reduction of the PCE is observed.

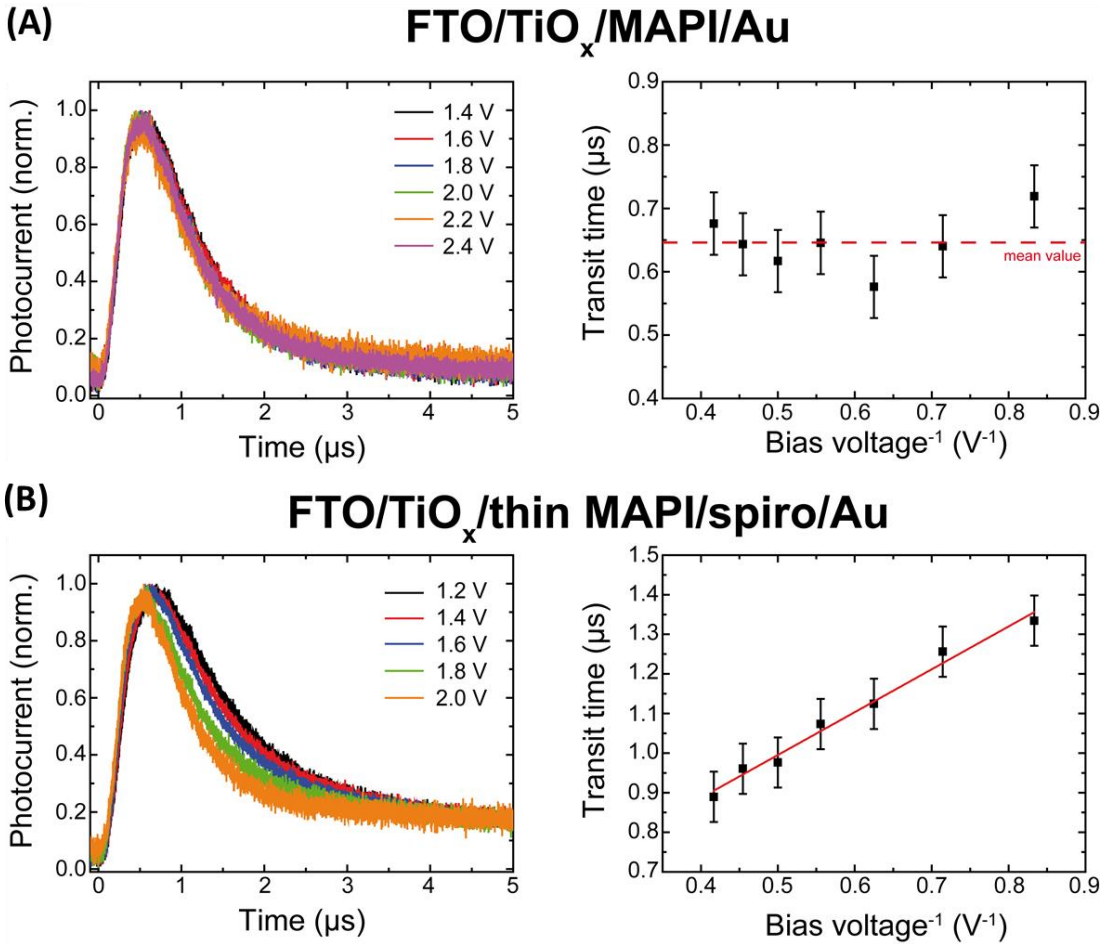

Figure 4.9 ToF results for two extreme cases of solar cell devices. (A) Photocurrent curves obtained for a device without the HTL spiro-OMeTAD and the respective transit times. (B) *j-t* profiles for a device with a very thin MAPI layer (approx. 100 nm) and 370 nm of spiro-OMeTAD and corresponding transit times, showing nearly the same transit time of about 0.95 µs at 2 V when in orporating a full-sized MAPI layer of 350 nm as shown in Figure 4.5.

We find similar slopes for the HTL and the ETL of 1.22 ± 0.07 and 2.43 ± 0.36 nm/ns, respectively. Additionally, the calculated mobility values as a function of HTL and ETL thicknesses are consistent, assuming *d* as the sum of the thicknesses of all layers, and show only minor variations (Figure 4.10).

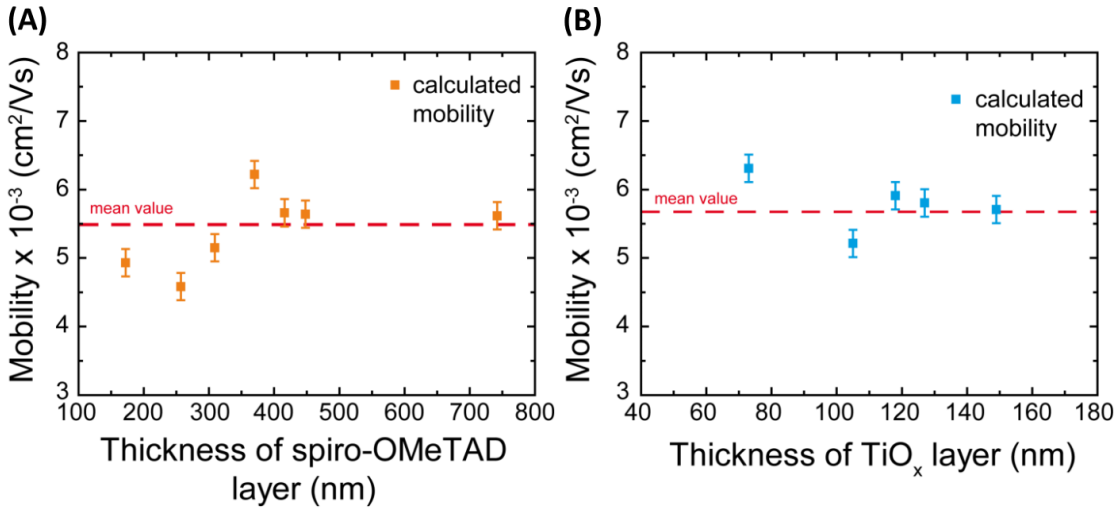

Figure 4.10 Calculated charge carrier mobilities in stacked devices for varying thicknesses of (A) spiro-OMeTAD and (B) TiO_x. The values were determined from the linear function relating the transit time and the applied bias voltage (see Figure 4.8B and D).

On the basis of the charge carrier mobility values obtained from the experiments on laterally contacted MAPI, the average drift velocity v_d of holes through the absorber layer is calculated according to the expression

$$v_d = \mu_{MAPI,h^+} \cdot E \tag{4.2}$$

and results in 290 nm/ns. With the thickness of MAPI (approximately 360 nm) in the full solar cell device, the contribution of the perovskite absorber layer to the overall transit time of the device can be estimated to be ~1 ns. This number represents an upper limit because it can be expected that in the vertical solar cell architecture, the charges will have to pass a smaller number of grain boundaries than in the lateral measurements presented in Figure 4.2. Clearly, the estimated transit time is much smaller than the effective transit times observed for the HTL and the ETL. From our observations in the ToF experiments performed on the devices, we suggest that the effective charge carrier transit times in perovskite solar cells are mainly affected by the thickness of spiro-OMeTAD and, to a lesser extent, by the thinner TiO_x layer. This also leads to a reduction of the PCE for thicker layers and to pinholes and shunting for thinner spiro-OMeTAD layers, resulting in an optimum thickness of around 370 nm.

Consequently, the measurements on the contacted film establish that the absorber layer and its properties could be excluded from affecting the transport of photogenerated charges in working devices. This highlights that rather the thickness of the extraction layers, in particular of the HTL, is a major limiting factor for charge transport. Recently published investigations already

demonstrate different approaches to replace the commonly employed material spiro-OMeTAD by other organic or inorganic hole transporters such as EDOT-OMeTPA[39] or graphene[40] and TiO_x by tin dioxide.[41]

4.3 Conclusions

In this study, we investigated the mobilities of light-induced charge carriers in both individually contacted MAPI thin films and photovoltaic stacks based on this type of hybrid perovskite. Employing the ToF photocurrent technique, we observe charge carrier mobilities of 5.8 ± 0.3 cm^2/Vs for holes and 6.3 ± 0.2 cm^2/Vs for electrons in individual perovskite films in lateral dimensions. Compared to the mobilities determined for the n− i−p architecture consisting of FTO/TiO_x/MAPI/spiro-OMeTAD/Au and resulting in values decreased by 3 orders of magnitude, the photoactive perovskite layer can clearly be excluded from being a charge transport-limiting factor in the device. Complementary ToF experiments on solar cells with varying spiro-OMeTAD thicknesses demonstrate a significant increase of the transit time of charge carriers through the device stack with increasing extraction layer thickness. By tuning the TiO_x thickness, we observe a similar effect on the transit times. From this, we conclude that mainly the thickness of spiro-OMeTAD contributes substantially to the transit time and to the mobility in the stacked system. Hence, the HTL represents a major transport-limiting factor in the working device that should be considered in efforts aimed at further device and interface optimization.

4.4 Experimental Section

4.4.1 Perovskite Thin Film Synthesis

The synthesis procedure for methylammonium lead triiodide thin films is based on a method recently published by Xiao et al.[17] A solution ontaining PbI_2 (1.25 M, TCI 98%) and methylammonium iodide (1.25 M, Dyesol) in a 4:1 mixture of DMF and DMSO, respectively, was spin-coated onto the substrate at 1000 rpm for 10 s followed by 5000 rpm for 30 s. After 7 s of the second spinning step, 500 µL of anhydrous chlorobenzene (Sigma) were added on top of the substrate. Finally, the substrate was annealed at 40 °C for 40 min and 100 °C for 10 min. The obtained perovskite films revealed an average thickness of 350 nm, estimated via SEM cross-sections.

4.4.2 Laterally Arranged Gold Contacts on Glass

Prior to all subsequent optical lithography steps, glass sheets were cleaned with a 2% Hellmanex solution and rinsed with deionized water. Afterwards the substrates were sonicated for 5 min in acetone and later with 2-propanol and exposed to oxygen plasma for 10 min to ensure the removal of surface residues and subsequent adhesion of the metallic contacts on glass. The structures were created via microstencil lithography by depositing a 30 nm thick layer of gold through a microscale shadow mask via thermal evaporation under vacuum (10^{-7} mbar). Finally, the coated glass sheets with inter-electrode distances between 36 and 80 µm were cleaned with 2-propanol. Deposition of the perovskite thin films was done according to the fabrication protocol mentioned above. Additionally, the films were coated with a thin layer of poly(methyl methacrylate) (PMMA) by spincoating 50 mg/mL PMMA in anhydrous chlorobenzene in order to avoid degradation through ambient moisture.

4.4.3 Solar Cell Fabrication

Fluorine doped tin oxide (FTO) coated glass substrates (7 Ω, Hartford Glass) were patterned using zinc powder and 3 M HCl. Then the sheets were successively cleaned with deionized water, 2% Hellmanex solution, then once again with deionized water, acetone and ethanol. Oxygen plasma treatment for 5 min before applying the blocking layer aided in the removal of organic residues on the surface.

The substrates were then covered with a sol-gel derived TiO_x layer by spincoating the precursor solution (see below), annealing at 150 °C (10 min) and calcining at 500 °C (45 min) in air.[12] For the sol-gel approach a solution of hydrochloric acid in 2-propanol (typically 35 µL of 2 M HCl and 2.5 mL of 2-propanol) was added dropwise to a solution of titanium isopropoxide in anhydrous 2-propanol (367.5 µL titanium isopropoxide in 2.5 mL of 2-propanol) under vigorous stirring. Next, the solution was filtered with a 0.25 µm syringe filter and the remaining clear TiO_x solution was spin-coated onto the FTO substrates at 2000 rpm for 45 s.

To obtain different thicknesses of the blocking layer, TiO_x was spin-coated layer by layer. After deposition of the TiO_x solution at 2000 rpm or 3000 rpm for 45 s, the substrates were annealed at 150 °C and the next layer was spin-coated using the same settings. This procedure was repeated several times (see Table 4.1) and the resulting thicknesses were determined via SEM cross-sections. SEM images were recorded with a FEI Helios G3 UC microscope.

Table 4.1 Preparation parameters for different TiO_x thicknesses in solar cells.

Spin speed (rpm)	Number of layers	Thickness of TiO_x layer (nm)
2000	1	70 ± 14
2000	2	120 ± 13
2000	3	150 ± 14
3000	2	105 ± 13
3000	3	130 ± 15

After deposition of the hybrid perovskite film following the aforementioned synthesis procedure and a short cooling period to room temperature, a thin layer of spiro-OMeTAD serving as hole transporting material was spin-coated at different speeds to tune the layer thickness (see Table 4.2). For this purpose, a 100 mg/mL solution of spiro-OMeTAD in anhydrous chlorobenzene was prepared and filtered. Oxidation of the material was performed by adding 10 µL of 4-tert-butylpyridine (Sigma 96%) and 30 µL of a 170 mg/mL lithium bistrifluoromethanesulfonimidate (Sigma 99.95%) solution in anhydrous acetonitrile (Sigma) to 1 mL of spiro-OMeTAD solution. The doped solution was then spin-coated on the coated substrate, which was stored in a desiccator at approximately 25% relative humidity to allow for oxidation of spiro-OMeTAD. Finally, 40 nm thick top gold electrodes were deposited by thermal evaporation of gold under vacuum ($>5 \cdot 10^{-6}$ mbar).

Table 4.2 Preparation parameters for different spiro-OMeTAD thicknesses in solar ells.

Spin speed (rpm)	Duration (s)	Thickness of spiro-OMeTAD layer (nm)
500	40	740 ± 12
2000	5	
1000	40	420 ± 18
2000	5	
1500	40	370 ± 10
2000	5	
2000	45	300 ± 22
3000	45	260 ± 18
5000	45	170 ± 13

4.4.4 Solar Cell Characterization

J -V measurements were carried out with a Keithley 2400 source meter under AM1.5G simulated sunlight with an incident power of ca. 100 mW/m^2 (Newport Oriel Sol2A), corrected for the proper light intensity using a Fraunhofer ISE certified silicon cell. All photovoltaic devices were measured under ambient conditions by pre-biasing at 1.5 V for 5 seconds under illumination, before scanning from 1.5 to 0 V and back at a scan rate of 0.4 V/s. The illuminated square area of the solar ells was about 0.0831 cm^2, defined with a metallic aperture mask.

4.4.5 ToF Measurements

Charge carrier mobilities in laterally contacted thin films were determined via ToF measurements (Figure 4.11). The films were illuminated from the semitransparent glass/gold bottom side by employing pulsed laser excitation at 540 nm and a pulse width of 7 ns. To extract the photogenerated charges, a constant dc field is applied at the electrodes solely for the measurement period of approximately 1 s to prevent ionic migration within the perovskite.[18-19] The created current is recorded as a function of time, resulting in ToF transients shown in Figure 4.2A. Charge carrier mobilities in stacked solar cell devices were extracted from photocurrent measurements employing the same experimental setup by illuminating the samples from the transparent glass side. For all solar cells, a full data set comprising photocurrent transients at bias voltages between 1.2 and 3.0 V was recorded in steps of 200 mV to confirm the applicability of eq 4.1 to the determined transit times (Figure 4.8B and D).

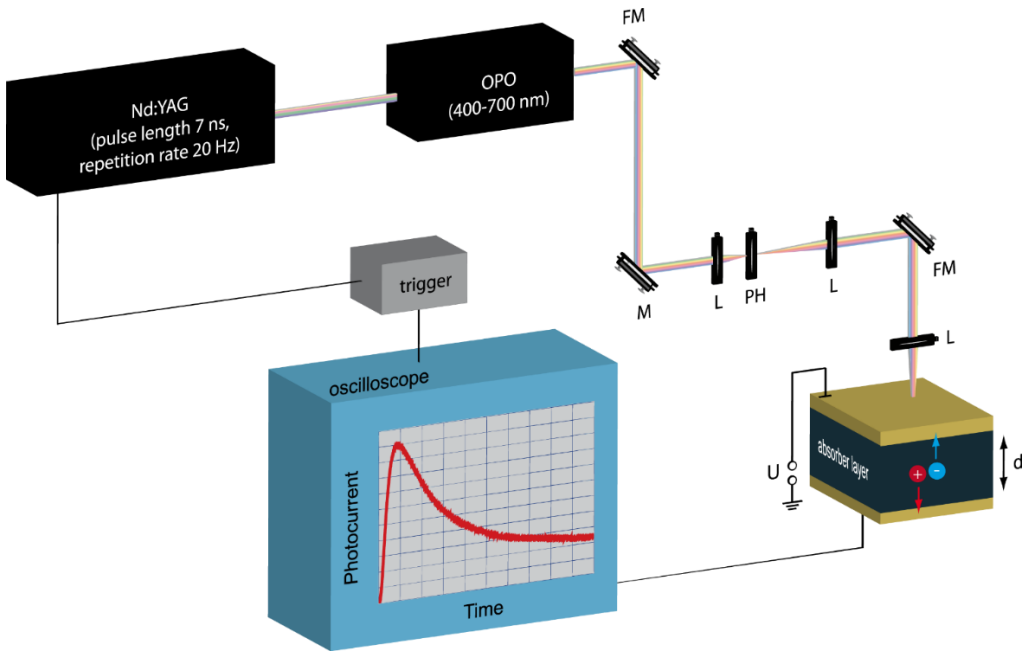

Figure 4.11 Scheme of the experimental setup employed for ToF studies.

4.5 References

1. Park, N. G., *Mater. Today* **2015,** 18, 65.
2. Sadhanala, A., et al., *J. Phys. Chem. Lett.* **2014,** 5, 2501-2505.
3. Kojima, A.; Teshima, K.; Shirai, Y.; Miyasaka, T., *J. Am. Chem. Soc.* **2009,** 131, 6050-6051.
4. Löper, P., et al., *Phys. Chem. Chem. Phys.* **2015,** 17, 1619.
5. Werner, J.; Weng, C. H.; Walter, A.; Fesquet, L.; Seif, J. P.; De Wolf, S.; Niesen, B.; Ballif, C., *J. Phys. Chem. Lett.* **2016,** 7, 161.
6. Docampo, P., et al., *Adv. Energy Mater.* **2014,** 4, 1400355.
7. Huang, L.; Hu, Z.; Xu, J.; Zhang, K.; Zhang, J.; Zhu, Y., *Sol. Energy Mater. Sol. Cells* **2015,** 141, 377.
8. Saliba, M., et al., *Energy Environ. Sci.* **2016,** 9, 1989-1997.
9. Green, M. A.; Emery, K.; Hishikawa, Y.; Warta, W.; Dunlop, E. D., *Prog. Photovolt.: Res. Appl.* **2016,** 24, 905.
10. Zhou, H., et al., *Science* **2014,** 345, 542-546.
11. Mali, S. S.; Hong, C. K., *Nanoscale* **2016,** 8, 10528.
12. Ball, J. M.; Lee, M. M.; Hey, A.; Snaith, H. J., *Energy Environ. Sci.* **2013,** 6, 1739.
13. Sanchez, R. S.; Mas-Marza, E., *Sol. Energy Mater. Sol. Cells* **2016,** 158, 189.
14. Cacovich, S.; Divitini, G.; Ireland, C.; Matteocci, F.; Di Carlo, A.; Ducati, C., *ChemSusChem* **2016,** 9, 2673.
15. Kim, H.-S.; Park, N.-G., *J. Phys. Chem. Lett.* **2014,** 5, 2927-2934.
16. Jena, A. K.; Chen, H. W.; Kogo, A.; Sanehira, Y.; Ikegami, M.; Miyasaka, T., *ACS Appl. Mater. Interfaces* **2015,** 7, 9817.
17. Xiao, M., et al., *Angew. Chem., Int. Ed.* **2014,** 53, 9898.
18. Eames, C.; Frost, J. M.; Barnes, P. R. F.; O'Regan, B. C.; Walsh, A.; Islam, M. S., *Nat. Commun.* **2015,** 6, 7497.
19. Tress, W.; Marinova, N.; Moehl, T.; Zakeeruddin, S. M.; Nazeeruddin, M. K.; Gratzel, M., *Energy Environ. Sci.* **2015,** 8, 995-1004.
20. Zhang, Y., et al., *Mater. Horiz.* **2015,** 2, 315.
21. Scher, H.; Montroll, E. W., *Phys. Rev. B: Solid State* **1975,** 12, 2455.
22. Fuhs, W.; Milleville, M.; Stuke, J., *Phys. Status Solidi B* **1978,** 89, 495.
23. Savenije, T. J., et al., *J. Phys. Chem. Lett.* **2014,** 5, 2189.
24. Milot, R. L.; Eperon, G. E.; Snaith, H. J.; Johnston, M. B.; Herz, L. M., *Adv. Funct. Mater.* **2015,** 25, 6218.

25. Peng, J.; Sun, Y.; Chen, Y.; Yao, Y.; Liang, Z., *ACS Energy Lett.* **2016,** 1, 1000.
26. Ponseca, C. S., et al., *J. Am. Chem. Soc.* **2014,** 136, 5189.
27. Wehrenfennig, C.; Eperon, G. E.; Johnston, M. B.; Snaith, H. J.; Herz, L. M., *Adv. Mater.* **2014,** 26, 1584-1589.
28. Hutter, E. M.; Eperon, G. E.; Stranks, S. D.; Savenije, T. J., *J. Phys. Chem. Lett.* **2015,** 6, 3082.
29. Karakus, M.; Jensen, S. A.; D'Angelo, F.; Turchinovich, D.; Bonn, M.; Cánovas, E., *J. Phys. Chem. Lett.* **2015,** 6, 4991.
30. Mei, Y.; Zhang, C.; Vardeny, Z. V.; Jurchescu, O. D., *MRS Commun.* **2015,** 5, 297.
31. Chen, Y., et al., *Nat. Commun.* **2016,** 7, 12253.
32. Senanayak, S. P., et al., *Sci. Adv.* **2017,** 3, e1601935.
33. Liu, D.; Gangishetty, M. K.; Kelly, T. L., *J. Mater. Chem. A* **2014,** 2, 19873.
34. Wang, K.; Liu, C.; Du, P.; Chen, L.; Zhu, J.; Karim, A.; Gong, X., *Org. Electron.* **2015,** 21, 19.
35. Marinova, N.; Tress, W.; Humphry-Baker, R.; Dar, M. I.; Bojinov, V.; Zakeeruddin, S. M.; Nazeeruddin, M. K.; Grätzel, M., *ACS Nano* **2015,** 9, 4200.
36. Abate, A., et al., *Phys. Chem. Chem. Phys.* **2013,** 15, 2572.
37. Maynard, B.; Long, Q.; Schiff, E. A.; Yang, M.; Zhu, K.; Kottokkaran, R.; Abbas, H.; Dalal, V. L., *Appl. Phys. Lett.* **2016,** 108, 173505.
38. Chen, Y.; Peng, J.; Su, D.; Chen, X.; Liang, Z., *ACS Appl. Mater. Interfaces* **2015,** 7, 4471.
39. Petrus, M. L.; Bein, T.; Dingemans, T. J.; Docampo, P., *J. Mater. Chem. A* **2015,** 3, 12159.
40. Agresti, A.; Pescetelli, S.; Taheri, B.; Del Rio Castillo, A. E.; Cinà, L.; Bonaccorso, F.; Di Carlo, A., *ChemSusChem* **2016,** 9, 2609.
41. Murugadoss, G.; Kanda, H.; Tanaka, S.; Nishino, H.; Ito, S.; Imahori, H.; Umeyama, T., *J. Power Sources* **2016,** 307, 891.

5 Light-Emitting Electrochemical Cells based on Hybrid Perovskite Nanoparticles

This chapter is based on the following publication:

Meltem F. Aygüler,* Michael D. Weber,* Bianka M. D. Puscher, Dana D. Medina, Pablo Docampo and Rubén D. Costa, *Journal of Physical Chemistry C*, 2015, 119, 21047-21054

* These authors contributed equally to this work.

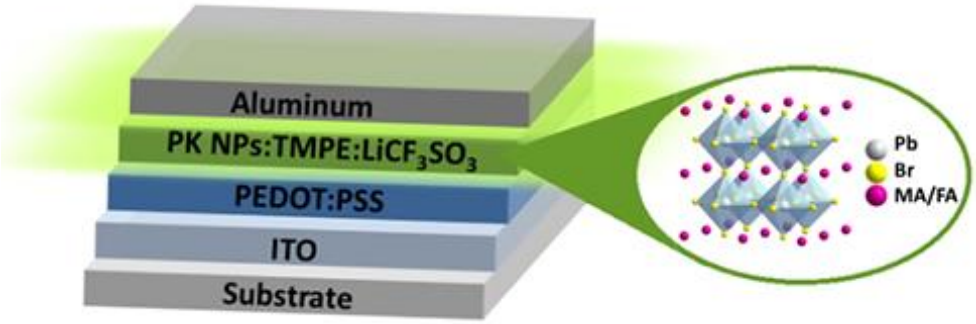

Keywords

Perovskite nanoparticles, formamidinium, methylammonium, lead bromide, light-emitting electrochemical cells

5.1 Introduction

Light-emitting electrochemical cells (LECs) have recently emerged as a potential alternative to organic light-emitting diodes (OLEDs) due to the use of air-stable injection layers and/or electrodes, as well as its simple device architecture consisting of a single layer sandwiched between two electrodes, for example, indium tin-oxide (ITO) and aluminum.[1-4] In addition, they can operate at very low voltages, yielding highly efficient devices, which can be easily fabricated under ambient conditions on any kind of substrate.[3]

In LECs, the active layer typically consists of either a mixture of a light-emitting polymer, an ion conducting polymer and an inorganic salt or only one ionic transition-metal complex (iTMC).[1-3] However, other luminescent materials can also be easily incorporated.[5-8] For instance, Bader *et al.* reported on yellow and orange LECs incorporating a blend of CdSe/ZnS quantum dots (QDs), a PF/PPV copolymer-poly[(9,9-dioctyl-2,7-divinylene-fluorenylene)-alt-co-{2-meth-oxy-5-(2-ethyl-hexyloxy)-1,4 phenylene}], and the polymerizable ionic liquid allyltrioctylammonium allylsulfonate (ATOAAS) as the source of counter ions.[7] Recently, Qian *et al.* expanded this concept to include blue, green, red, and white, conventional and flexible QD-LECs.[8]

The major limitation of inorganic QDs in lighting applications is the significant reduction of the photoluminescence quantum yields (PLQYs) after ligand exchange, a step that is necessary for their application in devices.[8] Additionally, all the developed QDs exhibit significant sub-bandgap defects, which effectively limit the maximum device performance achievable.[9] This issue is, however, not present in the newly developed organic-inorganic metal halide perovskites, where grain boundaries and surface defects do not generate deep trap states within the bandgap.[10-11] For this reason, the application of these materials in lighting applications is expected to enable the fabrication of highly efficient and low-cost devices.

Previously, electroluminescence (EL) from perovskite films was only achieved by using either low temperatures (77-110 K) or by introducing light-emitting organic compounds into the crystal lattice.[12-15] EL from bulk films at room temperature was recently achieved by Tan *et al.*[16] and Kim *et al.*[17] while Schmidt *et al.*[18] reported on the first synthesis of methylammonium lead bromide ($MAPbBr_3$) perovskite nanoparticles (NPs), showing the possibility to use them as light-emitting materials in OLEDs. This result represents an important contribution to the field, since the preparation of perovskite NPs is the first step to facilitate their implementation in new thin film device architectures by blending them with other electroactive materials.

Here, we highlight two major aspects of our current work. First, we have expanded the fundamental knowledge regarding the synthesis of new hybrid metal halide perovskite NPs, showing that the photophysical features of this novel material can be tuned by exchanging the organic cation group to formamidinium (FA). Second, we have fabricated the first $MAPbBr_3$- and $FAPbBr_3$-based LECs featuring a luminance of around 1–2 cd/m^2 at low driving currents by developing a deposition protocol based on spray-coating, bringing this technology closer to large-scale applications.

5.2 Synthesis and Characterization of Hybrid Lead Halide Nanoparticles

Both $MAPbBr_3$ and $FAPbBr_3$ NPs were prepared through the addition of octylammonium bromide in a warm solution of oleic acid in octadecene followed by lead bromide ($PbBr_2$) and either MABr or FABr.[18] Here, we have found that the dropwise addition of the solution containing the organic cation is crucial to obtain pure compounds. Additionally, we have employed THF as the precipitating agent in order to compatibilize the NP solution with the electrolyte solution, necessary for device deposition. This procedure results in a yellow-orange colloidal solution of highly crystalline perovskite NPs – see Experimental Section for more details. The addition of a long chain alkyl ammonium cation was essential to limit the perovskite crystal growth, as reactions prepared without this capping agent resulted in micron-sized crystals.[18]

Both synthesis protocols yielded highly crystalline perovskite NPs, which were characterized by powder X-ray diffraction (PXRD) in order to ascertain their crystal structure (Figure 5.1). The observed diffraction patterns obtained at room temperature correspond to the cubic crystal phase with lattice constants of 5.939(2) and 6.000(2) Å (both of a space group Pm-3m) for $MAPbBr_3$ and $FAPbBr_3$ NPs, respectively; consistent with previous reports[18-20]. The size of the NPs was characterized by transmission electron microscopy (TEM). TEM images showed that the size distribution is not homogeneous since there are big aggregates as well as small-sized NPs (<10 nm) for both compositions as seen in Figure 5.2.

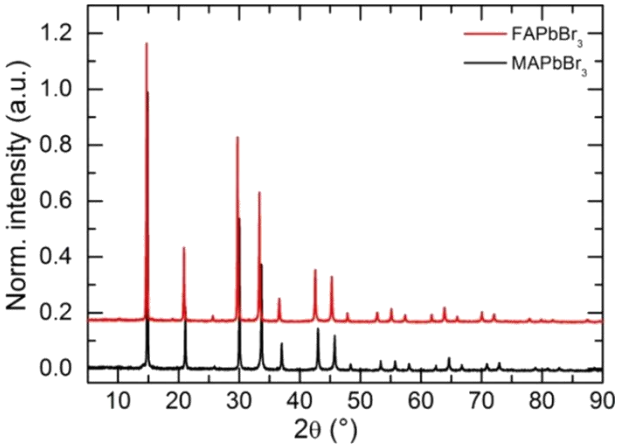

Figure 5.1 PXRD pattern of both $MAPbBr_3$ (black) and $FAPbBr_3$ (red) NPs.

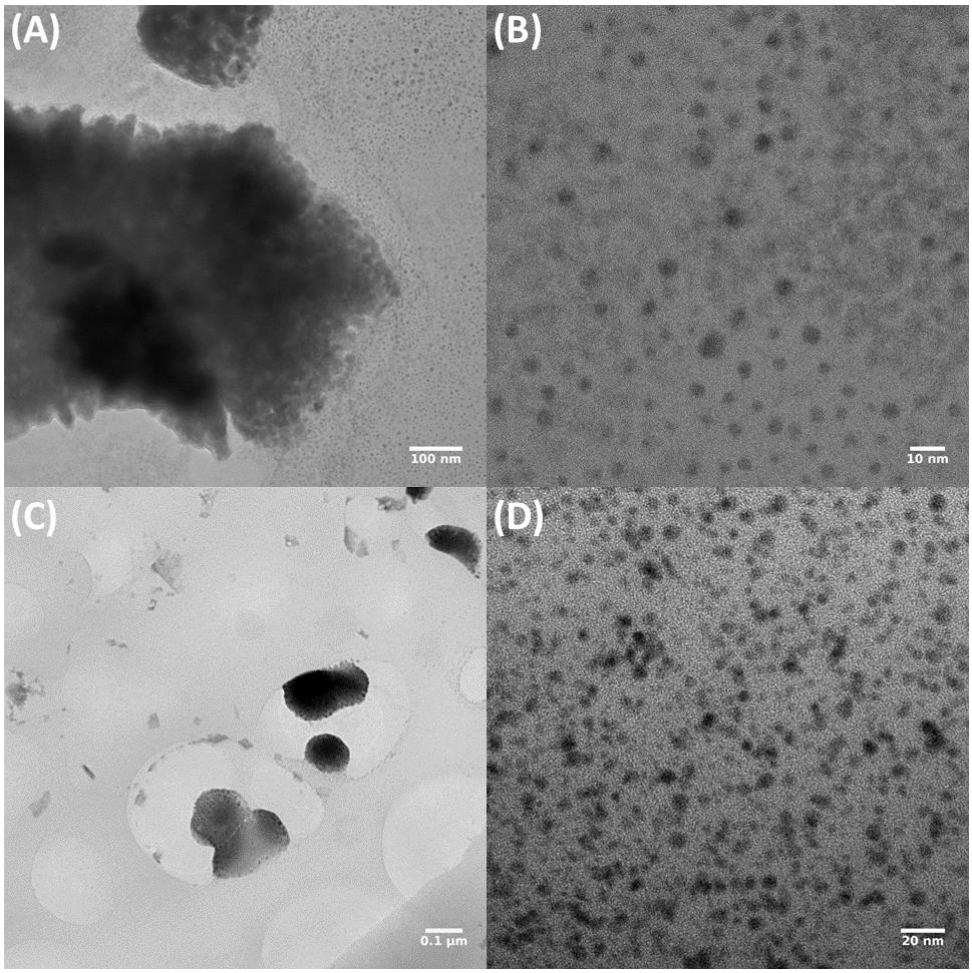

Figure 5.2 TEM images of (A, B) $MAPbBr_3$ and (C, D) $FAPbBr_3$ NPs at different scale bars.

The photophysical features of $MAPbBr_3$ and $FAPbBr_3$ NPs were investigated by steady-state absorption and photoluminescence (PL) spectroscopy in solution, Figure 5.3. In particular, the

absorption spectra of the $FAPbBr_3$ colloidal solutions exhibit a narrow band at 542 nm, which is 13 nm red-shifted compared to that of $MAPbBr_3$ suspensions, Figure 5.3A. This is attributed mainly to the reduction of the optical band gap of $FAPbBr_3$ NPs due to the larger unit cell.[21] Indeed, the optical band gaps of $MAPbBr_3$ and $FAPbBr_3$ NPs were found to be 2.24 eV and 2.14 eV as estimated by Tauc plots, Figure 5.3C and D. More interesting is, however, the direct comparison of the PL features between both types of perovskite NPs – Figure 5.3B. Both materials exhibit a near band edge emission with a narrow full width at the half-maximum (FWHM) of approximately 19 nm. This corresponds to features noted for bulk-like films,[19] indicating the high quality and crystallinity of the prepared NPs. The exchange of MA to FA results in a red-shifted emission spectrum, that is, going from 532 to 545 nm for $MAPbBr_3$ and $FAPbBr_3$ NPs, respectively.

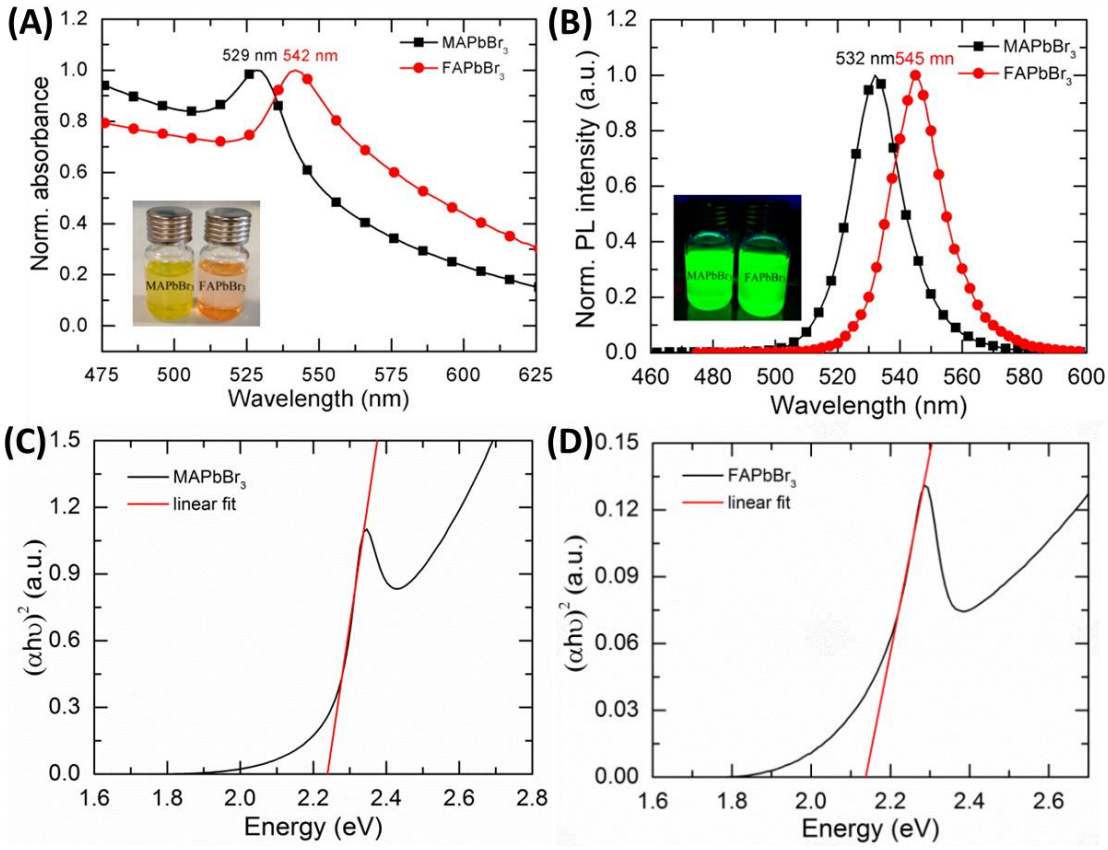

Figure 5.3 (A) Normalized absorption and (B) PL spectra at 403 nm excitation wavelength and ~0.3 μJ/cm^2 pump fluence of $MAPbBr_3$ (black squares) and $FAPbBr_3$ (red circles) NPs in THF. Photographs of the solutions in THF are shown under (A) ambient light and (B) 365 nm excitation. Tauc plots of (C) $MAPbBr_3$ and (D) $FAPbBr_3$ NPs.

In order to further examine the differences in their photophysical behavior, the NPs were characterized in solution *via* time-resolved PL – Figure 5.4. The obtained data was fit by a simple bimolecular recombination model:[10, 22-23]

$$f(t) = \frac{1}{a + bt}$$

where *a* is related to the charge density at $t = 0$, and *b* is the recombination parameter. The fittings suggest that the decay of the PL arises from bimolecular recombination of free charges, similar to that observed in perovskite films.[10] Since both NP solutions absorbed light similarly at the excitation wavelength, and assuming that early time charge generation is similar for both materials, we can directly compare the fitted recombination parameters. The radiative bimolecular recombination rate of $FAPbBr_3$ NPs is approximately six times slower than $MAPbBr_3$ NPs – Figure 5.4. While slow recombination dynamics are beneficial for solar cell operation,[19] the opposite is true for light emitting devices since a reduction of the PL quantum yield (PLQY) is expected. To confirm this, the PLQYs in solution were determined with an integrating sphere. In line with the bimolecular recombination rate results, $MAPbBr_3$ and $FAPbBr_3$ NPs exhibited PLQYs of approximately 15% and 5%, respectively. It is important to point out that, similar to that noted by other groups,[18] the accuracy of the PLQYs is subjected to, the intrinsic scattering process of the suspensions, and the self-absorption due to the very small Stokes shift.

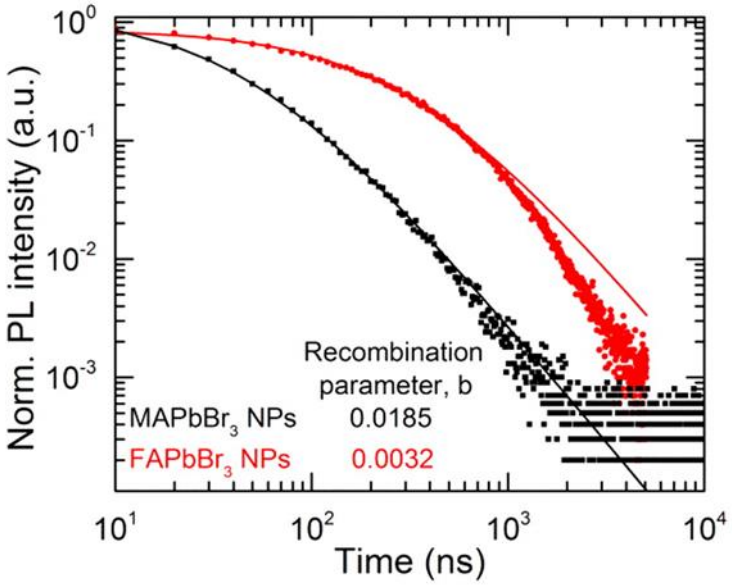

Figure 5.4 Time-resolved PL decay for $MAPbBr_3$ (black squares) and $FAPbBr_3$ (red circles). Solid lines in time-resolved PL decay curves are fits to the data with a simple bimolecular recombination model.

5.3 Fabrication of LECs based on Perovskite NPs

As a final step, we took advantage of the excellent stability of the perovskite NPs in solution to prepare the first perovskite-based LEC devices. To this end, an electrolyte matrix comprised of $LiCF_3SO_3$ and trimethylolpropane ethoxylate (TMPE) was added to the colloidal suspensions of the perovskite NPs and immediately filtered. The mixture of NPs and electrolyte matrix was spray-coated onto an ITO substrate which was modified by a 100 nm thickness of poly(3,4-ethylenedioxythiophene) polystyrene sulfonate (PEDOT:PSS). In this work, active layers with two different thicknesses of approximately 100-120 and 50-70 nm were prepared. To finalize the devices, aluminum was evaporated as a top cathode with a thickness of 90 nm – see Experimental Section for more details.

One of the most difficult challenges when utilizing easily up-scalable techniques like spray-coating is the achievement of smooth and homogeneous films without degradation of the active material during film preparation.[24-25] To ensure this, the morphological and spectroscopic features of the active layers were examined by means of alpha-step profilometry and atomic force microscopy (AFM), as well as steady-state spectroscopy, respectively. AFM confirms that the films show an homogenous coverage with no particular aggregation or phase separation features and all give a similar root-mean-square (RMS) roughness of around 5-14 nm – Figure 5.5A. Furthermore, it was found that the addition of the matrix does not impact the PL emission maxima (Figure 5.5B and C) nor the PL decay dynamics (Figure 5.5D and E) compared to bare NPs films.

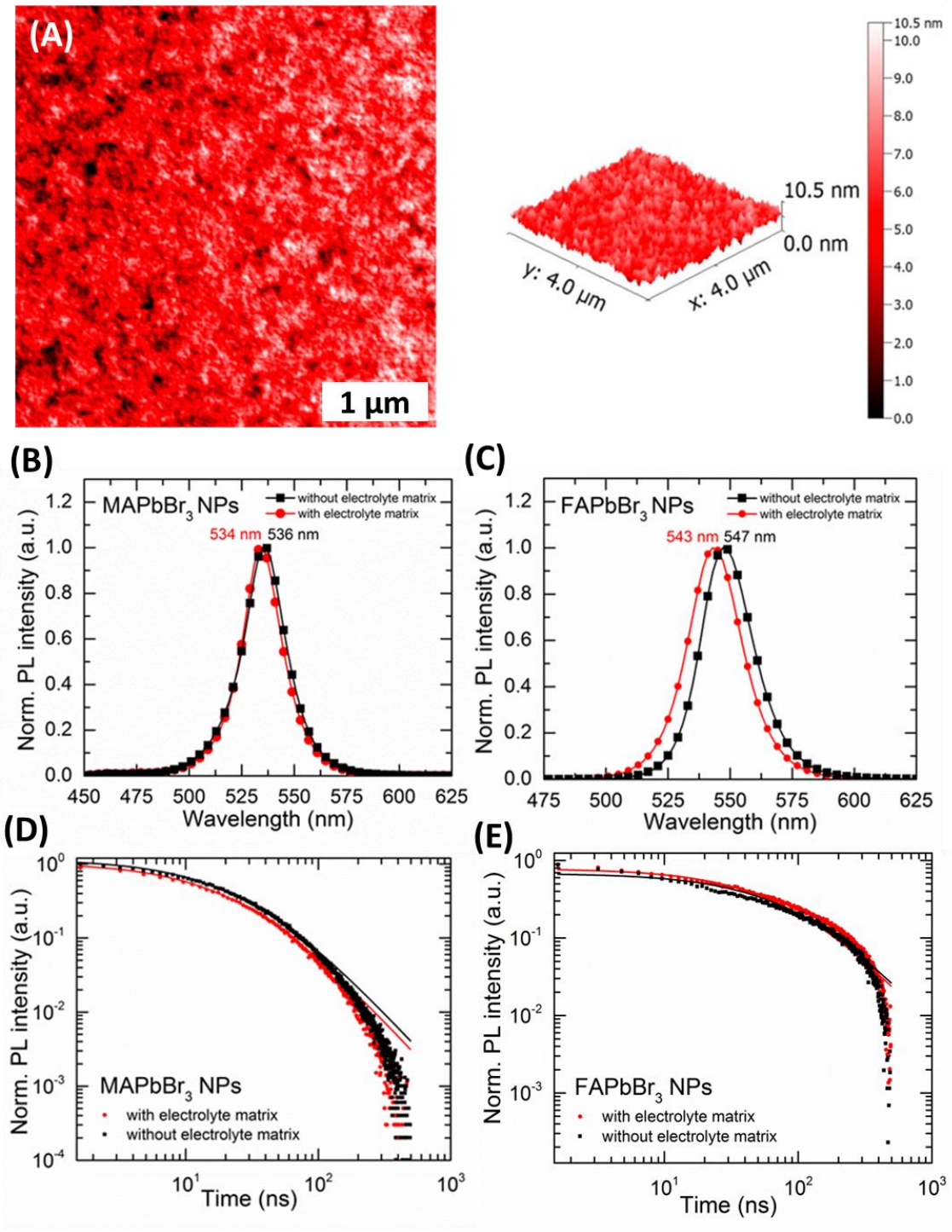

Figure 5.5 (A) AFM top view image and 3D profile of perovskite NPs films used for device fabrication. Normalized PL spectra of (B) $MAPbBr_3$ and (C) $FAPbBr_3$ NPs films with (red circles) and without (black squares) electrolyte matrix. Time resolved PL of films of (D) $MAPbBr_3$ and (E) $FAPbBr_3$ NPs with (red circles) and without (black squares) electrolyte matrix. Solid lines in time resolved PL decay curves are fits to the data with a simple bimolecular recombination model.

5.4 Characterization of LECs based on Perovskite NPs

Figure 5.6 depicts the luminance-current density versus applied voltage (LIV) of the perovskite-based LECs. The LIV features of devices, which do not incorporate an electrolyte matrix, show an injection voltage of around 15-16 V independently of the type of perovskite NPs, but no luminance was detected, even when constant and pulsed voltage and/or current driving schemes or current LIVs were applied. Upon the addition of the electrolyte matrix, the devices feature injection voltages of around 11-12 V (at $J > 0.1$ mA/cm^2) and maximum brightness of 1.3 cd/m^2 and 1 cd/m^2 for $MAPbBr_3$ and $FAPbBr_3$ NPs, respectively. In a qualitative way, this finding clearly demonstrates the relevant role of the electrolyte matrix in the device behavior.

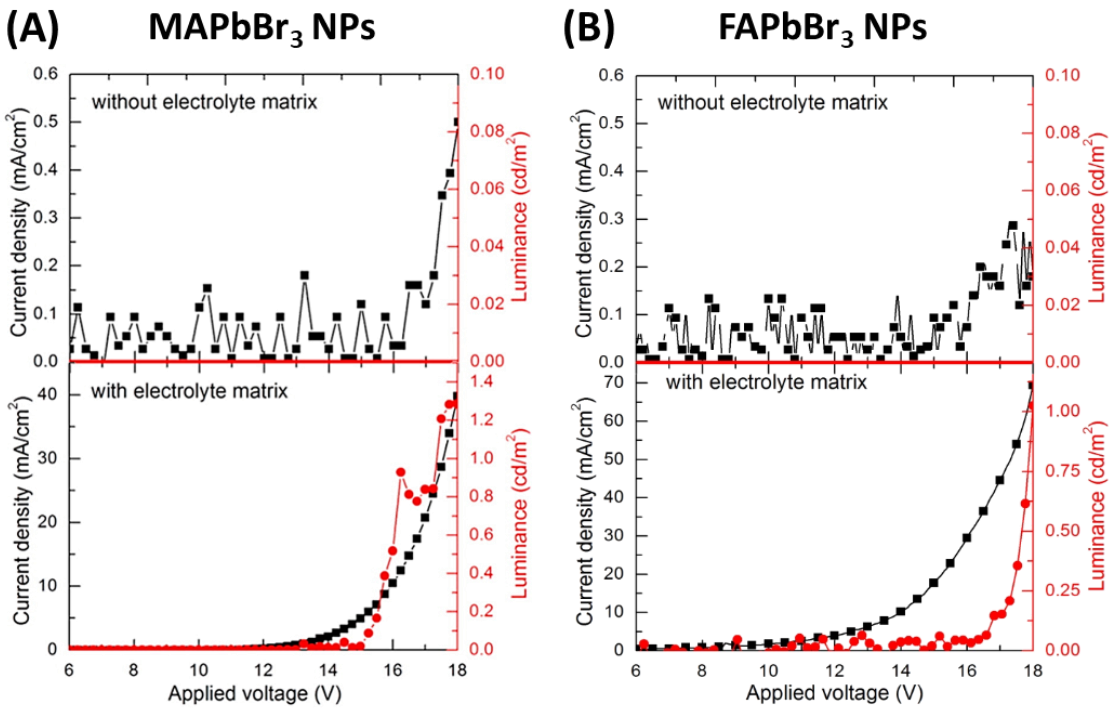

Figure 5.6 Luminance (red circles) - current density (black squares) vs applied voltage of ITO/PEDOT:PSS (100 nm)/Perovskite NPs without electrolyte matrix (50–70 nm) and with electrolyte matrix (100–120 nm)/Al (90 nm) devices based on (A) $MAPbBr_3$ and (B) $FAPbBr_3$ NPs.

The electroluminescence (EL) spectra of both perovskite NPs based LECs are shown in Figure 5.7. In general, 3D plots of the EL during the LIV assays show no change in both the shape and the maximum upon increasing the applied bias. In particular, the EL spectra of $MAPbBr_3$ and $FAPbBr_3$ NPs based devices are centered at 550 and 560 nm – Figure 5.7B. This represents a red-shift of 20-30 nm compared to the PL spectra of the active layer – Figure 5.3B and Figure 5.7B.

This finding has been typically observed in LECs and it is ascribed to the stabilization of the excited state due to polarization under the applied high electric field during operating conditions.[26]

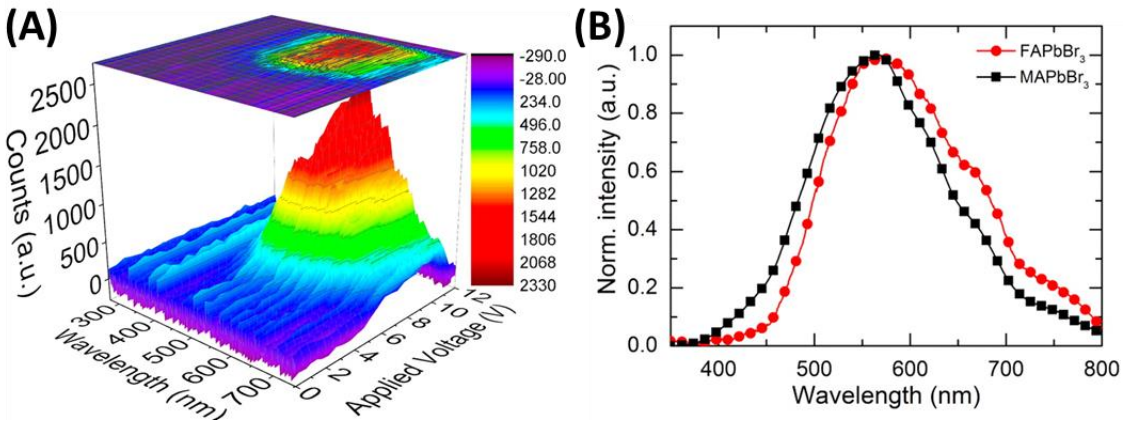

Figure 5.7 (A) 3D plot showing the EL spectra at different applied voltages during the LIV experiments of ITO/PEDOT:PSS/$FAPbBr_3$ NPs-electrolyte matrix (60–70 nm)/Al devices and (B) normalized EL spectra of ITO/PEDOT:PSS/perovskite NP-electrolyte matrix (60–70 nm)/Al devices at 10 V.

The benefit of blending perovskite NPs with an ionic-based polyelectrolyte is clearly highlighted by both the strong reduction of the injection voltage and the stable EL features. Thus, we can postulate that perovskite NP-based devices show a common LEC behavior.[1-4] For instance, upon application of a traditional constant voltage driving scheme, Figure 5.8A and C, the current density increases followed by a slow increase of the luminance, reaching values of 14 and 10 mA/cm^2 and 2 and 0.25 cd/m^2 for $MAPbBr_3$- and $FAPbBr_3$-based devices. This behavior is ascribed to the slow redistribution of the mobile ions at the electrode interface together with a fast growth of the p- and n-doped regions,[27-31] limiting the device performance. Recently, the application of a pulsed current driving scheme has been proposed to prevent the fast growth of the doped regions, while ensuring enough charge injection to provide an instantaneous emission.[1-2, 32] In line with previous studies, upon application of a pulsed current scheme, initial high voltages were required to maintain the desired current density as the redistribution of ions has not been realized yet – see inset graphs in Figure 5.8B and D. This allows both charge injection and a very slow redistribution of the mobile ions at the electrode interface. As such, the luminance is almost instantaneous and the average voltage decreases over the first minutes and remains constant, reaching maximum luminances of 1.8 and 0.8 cd/m^2 and efficiencies of 0.013 and 0.005 cd/A, as well as lifetimes of several hours for devices with $MAPbBr_3$ and $FAPbBr_3$ NPs, respectively. Since the average voltage profile remains practically constant, the reason for the loss in luminance might be ascribed to the intrinsic device operating mechanism.[27-31] It is important to point out that,

in good agreement with the PL features of the NPs, the $MAPbBr_3$ NP-based devices outperform $FAPbBr_3$ NP-based ones.

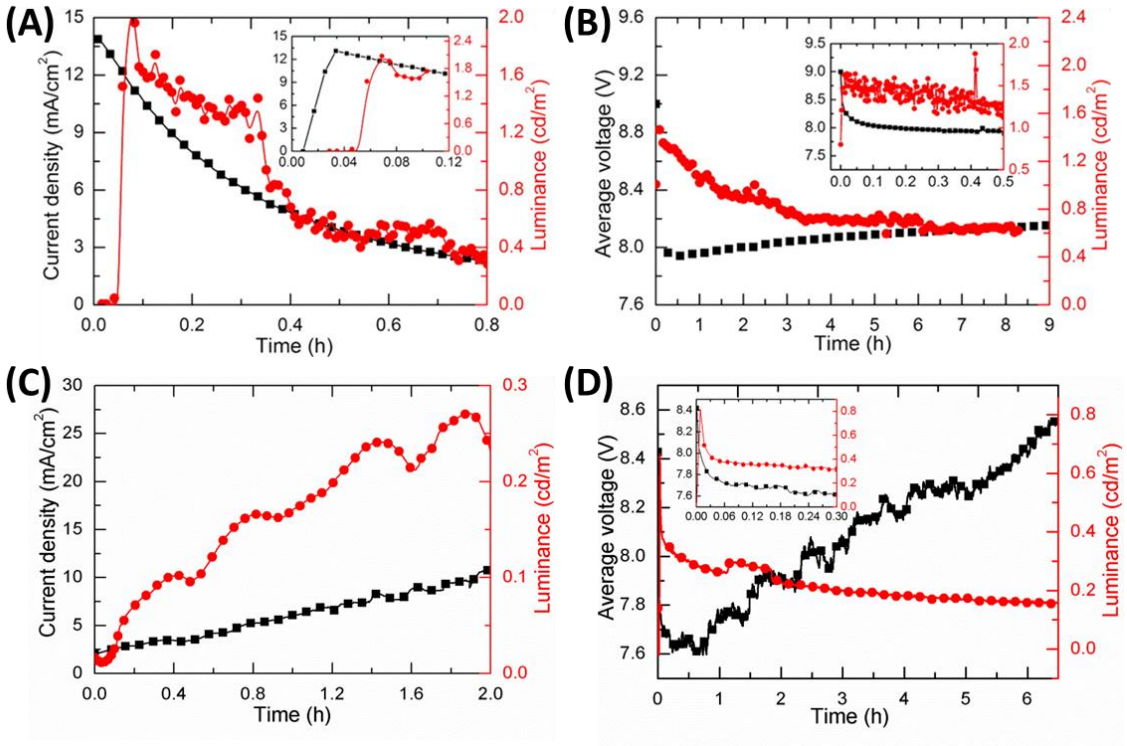

Figure 5.8 (A) Current density-luminance versus time of ITO/PEDOT:PSS/$MAPbBr_3$ NP-electrolyte matrix (100–120 nm)/Al driven by constant voltage of 14 V and (B) average voltage-luminance vs time of the same device driven by a pulsed current using a block wave at a frequency of 1 kHz with a duty cycle of 50% and an average current density of 13 mA/cm^2. (C) Current density-luminance versus time of ITO/PEDOT:PSS/$FAPbBr_3$ NP electrolyte matrix (100-120 nm)/Al driven at 16 V and (D) average voltage-luminance versus time of ITO/PEDOT:PSS/$FAPbBr_3$ NP-electrolyte matrix (100-120 nm)/Al driven at pulsed 1 kHz current of 15 mA/cm^2 .

Finally, we have also evaluated the air stability of the devices stored under ambient conditions for a period of two months. Surprisingly, both the device and the PL features do not seem to be significantly affected as shown in Figure 5.9. In particular, the shape and maximum of the EL spectra remain unaltered, while the two month old devices show slightly reduced luminance and efficiency levels when compared to fresh devices. This is quite likely to the result of unbalanced electron-hole recombination due to an increased leakage current caused by the degradation of the active layer and accumulation of moisture over time when stored under ambient conditions.

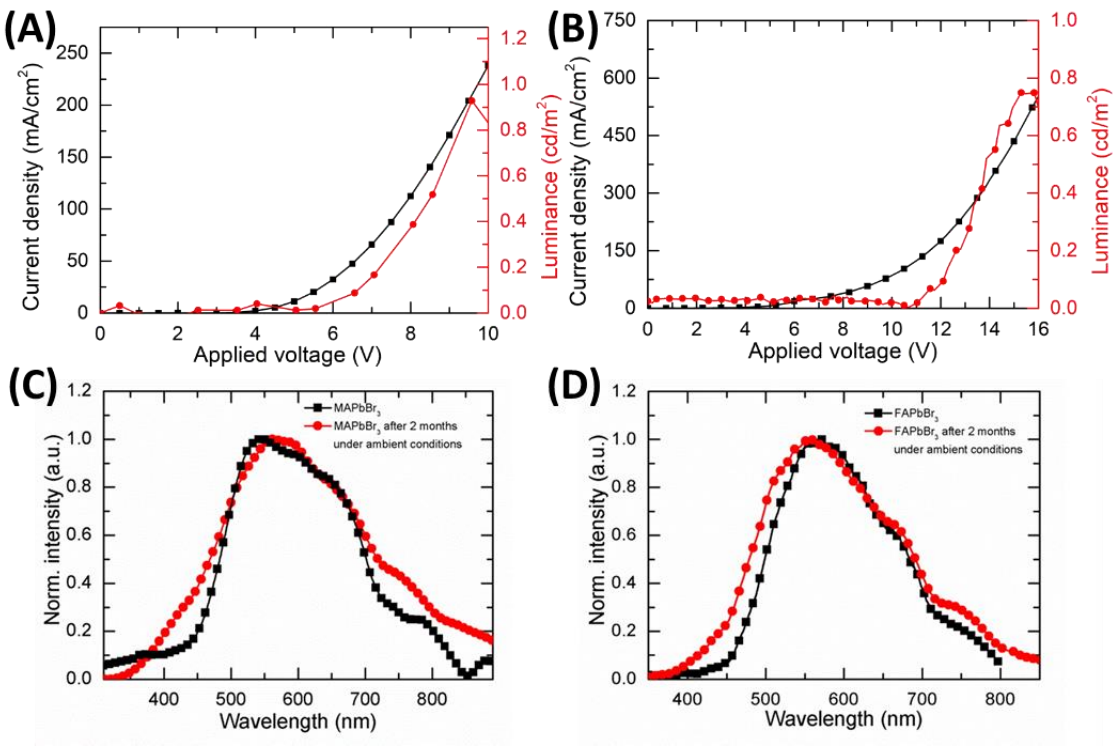

Figure 5.9 (A) Luminance–current density versus applied voltage plot of ITO/PEDOT:PSS/$FAPbBr_3$ NP-electrolyte matrix (60–70 nm)/Al for fresh device and (B) the same device kept under ambient conditions for two months. Electroluminescence spectra of both fresh and two month old (C) $MAPbBr_3$- and (D) $FAPbBr_3$-based devices obtained at the maximum luminance level of their respective LIV assays.

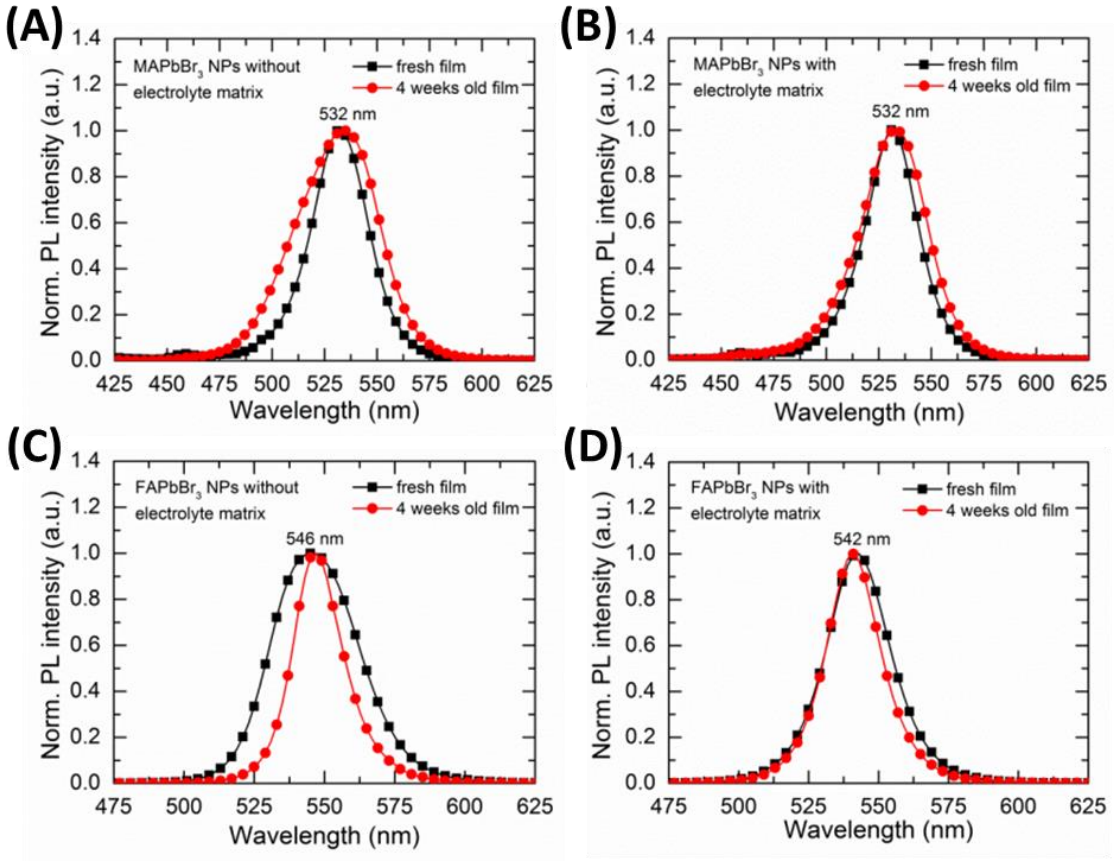

Figure 5.10 PL spectra of (A, B) $MAPbBr_3$ and (C, D) $FAPbBr_3$ films as deposited and aged under ambient conditions. (A, C) show the spectra of nanoparticles without the electrolyte matrix and (B, D) with the inclusion of this element deposited on a glass slide.

5.5 Conclusion

In this work, we have demonstrated the implementation of perovskite NPs into light-emitting electrochemical cells for the first time. We have synthesized hybrid perovskite NPs with two different organic cations, which were then incorporated into the final device via an up-scalable spray-coating technique. Exchanging the organic cation from MA to FA resulted in a 13 nm red-shift of both the emission and the absorption spectra. Our results show that FA-based NPs in solution exhibit a six times slower radiative recombination rate, which leads to a poorer PLQY and, in turn, to a lower device performance. Additionally, we have investigated the origin of photoluminescence in these materials. We conclude that PL arises from bimolecular recombination of electrons in the conduction band and holes in the valence band. Moreover, devices prepared with the electrolyte matrix showed stable yellowish green luminance at low driving currents while those without this component did not show any EL features. Finally, we

have demonstrated the stability of these devices and films stored under ambient conditions for over two months. Overall, this study opens up a new route to study organic–inorganic metal halide perovskite NPs and, additionally, opens a new avenue of research into the emerging field of LECs.

5.6 Experimental Section

5.6.1 Synthesis of Precursors

Methylammonium bromide (MABr) was prepared by following a published procedure.[19] In short, 24 mL of methylamine solution (33 wt % in ethanol) was diluted with 100 mL of absolute ethanol in a 250 mL round-bottom flask. Under constant stirring, 8 mL of an aqueous solution of hydrobromic acid (HBr, 48 wt %) was added to the flask. After stirring for 1 h at room temperature, the solvent was evaporated. The obtained white solid was washed with dry diethyl ether and finally recrystallized from ethanol.

Formamidinium bromide (FABr) was synthesized following a known procedure.[19] Formamidinium acetate was dissolved in a double molar excess of aqueous HBr (48 wt %), and the mixture was stirred at 50 °C for 60 min. The solvent and remaining HBr were removed by rotary evaporation. Slightly yellow powder was washed with dry diethyl ether. Lastly, recrystallization from ethanol led to the white crystalline product.

Octylamine (24.79 mL, 0.15 mol) was added to 200 mL of absolute ethanol in a 500 mL round-bottom flask. HBr (5 M, 30 mL, 0.15 mol) was added to the solution under constant stirring. After a reaction time of 1 h at room temperature, the solvent was removed by rotary evaporation. The product was washed with diethyl ether until the powder became white. Then, octylammonium bromide was recrystallized from 2-propanol.

5.6.2 Synthesis of Nanoparticles and Characterization Details

5.6.2.1 Synthesis of $MAPbBr_3$ Nanoparticles

A solution of oleic acid (850 mg, 3 mmol) in 20 mL of octadecene was stirred and heated at 80 °C in a 100 mL round-bottom flask under a N_2 atmosphere. Then, a capping agent, octylammonium bromide (126 mg, 0.6 mmol) was added to the flask, and the solution became cloudy. Lead(II) bromide (367 mg, 1 mmol dissolved in 1 mL of anhydrous DMF at 70 °C) was added to the reaction vessel and a clear and colorless solution was formed. Subsequent and dropwise addition of methylammonium bromide (44 mg, 0.4 mmol dissolved in 1 mL of anhydrous DMF) produced a yellow dispersion. Lastly, nanoparticles were immediately precipitated by the addition of

anhydrous THF (25 mL). The suspension was centrifuged at 7000 rpm for 10 min. The NPs' sedimentation and the solution were removed. Subsequently, the NPs were redispersed in THF and centrifuged three more times in order to remove the remaining oleic acid and octadecene. NPs were dried in air to obtain an orange powder and finally placed into a vial and were redispersed in anhydrous THF.

5.6.2.2 Synthesis of $FAPbBr_3$ Nanoparticles

A solution of oleic acid (170 mg, 0.6 mmol) in 4 mL of octadecene was stirred and heated at 80 °C in a 20 mL vial in air. Then, the capping agent, octylammonium bromide (25.2 mg, 0.12 mmol), was added to the vial and the solution became cloudy. Lead(II) bromide (73.4 mg, 0.08 mmol dissolved in 200 μL of anhydrous DMF at 70 °C) was added to the reaction vessel and a clear and colorless solution was formed. Subsequent and dropwise addition of formamidinium bromide (10 mg, 0.08 mmol dissolved in 200 μL of anhydrous DMF) produced a yellow dispersion. Lastly, nanoparticles were immediately precipitated by the addition of anhydrous THF (15 mL). The suspension was centrifuged at 7000 rpm for 10 min. The NPs sedimentation and the solution were removed. Subsequently, the NPs were redispersed in THF and centrifuged three more times in order to remove the remaining oleic acid and octadecene. Nanoparticles were dried in air to obtain orange powder and finally placed into a vial and were redispersed in anhydrous THF.

5.6.2.3 Characterization Details

The powder XRD measurements were performed on a Huber Imaging Plate Guinier Diffractometer G670 (Cu Kα1 radiation). Steady-state absorption spectra were measured with a Lambda 1050 UV/vis spectrophotometer (PerkinElmer) using an integrating sphere. Steady state efficiency and time-resolved PL measurements were performed with a Fluotime 300 spectrofluorometer (Picoquant GmbH). The excitation wavelength was fixed at 405 nm. The emission for time-resolved measurements was monitored at the maximum intensity of the steady state photo emission. ^{1}H NMR spectra were acquired at 25.8 °C using a Bruker Avance III HD spectrometer with a 400 MHz magnet (9.4 T). The chemical shifts are reported in ppm relative to tetramethylsilane (TMS). TEM measurements were performed with a JEM-2011 (JEOL) equipped with LaB_6 operated at 200 kV and EDS (EDAX) detector. The PLQYs were measured using a Fluoromax-4 photometer with a quanta-phi integrating sphere upon excitation of 400 nm. The films were prepared onto quartz slides. The samples were excited with Fluotime 300 Spectrofluorometer (Picoquant GmbH) with a diode laser at 405 nm with 800 ps pulse length and at different excitation fluences. AFM characterization was performed under ambient conditions

using SPM Nanoscope Illa multimode working in tapping mode with a HQ:NSC15/AL BS tip (μMasch) at a working frequency of ~325 kHz.

5.6.3 Device Fabrication and Chracterization Details

All materials were purchased from Sigma-Aldrich and used as received. The devices were prepared as follows. Indium tin oxide (ITO) coated glass plates were patterned by conventional photolithography (Naranjo Substrates). The substrates were cleaned by using sequential ultrasonic baths in detergent, water, and 2-propanol solvents. After drying, the substrates were placed in a UV–ozone cleaner (Jelight 42–220) for 10 min. A poly(3,4-ethylenedioxythiophene): poly(styrenesulfonate) (PEDOT:PSS) layer was doctor-bladed onto the ITO-glass substrate to flatten the transparent conducting electrode, which increased the device preparation yield (400 μm substrate distance and a speed of 10 mm/s). The luminescent layer comprised perovskite NPs and the polyelectrolyte matrix, $LiCF_3SO_3$, and trimethylolpropane ethoxylate (TMPE) with a mass ratio of 0.3:1 dissolved in THF, respectively. The electrolyte mixture was prepared via stirring for 5 h, followed by ultrasonication for 20 min after the perovskite NPs were added (1–2 mg/mL). We found this mixture as the most appropriate for spray-coating. Higher amounts tend to quickly agglomerate, hampering the deposition procedure. Finally, the solution was filtered using polytetrafluorethylene membrane filters with a pore size of 0.45 μm. The process was repeated until an orange stable suspension was achieved. The active layer was prepared via spray-pyrolysis–i.e., Ar flow at 1.5 atm and 90 °C. These conditions resulted in homogeneous thin films with a thickness ranging from 60 to 120 nm and a roughness of less than 5%, having no apparent optical defects. The latter was determined using a Bruker "DektakxT" profilometer. Once the active layer was deposited, the samples were transferred into an inert atmosphere glovebox (<0.1 ppm of O_2 and H_2O, Innovative Technology). The aluminum cathode electrode (90 nm) was thermally evaporated using a shadow mask under high vacuum ($<1 \times 10^{-6}$ mbar) using an Angstrom Covap evaporator integrated into the inert atmosphere glovebox. Time dependence of luminance, voltage, and current was measured by applying constant and pulsed voltage and current by monitoring the desired parameters simultaneously through an Avantes spectrophotometer (Avaspec-ULS2048LTEC) calibrated with a white LED in conjunction with a Newport (1916-c) optical power meter equipped with a calibrated silicon diode and Botest OLT OLED Lifetime-Test System. The electroluminescence spectrum was recorded using the above-mentioned spectrophotometer.

5.7 References

1. Costa, R. D.; Orti, E.; Bolink, H. J.; Monti, F.; Accorsi, G.; Armaroli, N., *Angew. Chem. Int. Ed.* **2012,** 51, 8178-8211.
2. Meier, S. B.; Tordera, D.; Pertegás, A.; Roldán-Carmona, C.; Ortí, E.; Bolink, H. J., *Materials Today* **2014,** 17, 217-223.
3. Sandström, A.; Asadpoordarvish, A.; Enevold, J.; Edman, L., *Adv. Mater.* **2014,** 26, 4974-4974.
4. YU ZhiBin, L. L., GAO HuiEr, PEI QiBing, *Sci. China Chem.* **2013,** 56, 1075-1086.
5. Tang, S.; Tan, W.-Y.; Zhu, X.-H.; Edman, L., *Chem. Commun.* **2013,** 49, 4926-4928.
6. Pertegás, A.; Tordera, D.; Serrano-Pérez, J. J.; Ortí, E.; Bolink, H. J., *J. Am. Chem. Soc.* **2013,** 135, 18008-18011.
7. Bader, A. J. N.; Ilkevich, A. A.; Kosilkin, I. V.; Leger, J. M., *Nano Lett.* **2011,** 11, 461-465.
8. Qian, G.; Lin, Y.; Wantz, G.; Davis, A. R.; Carter, K. R.; Watkins, J. J., *Adv. Funct. Mater.* **2014,** 24, 4484-4490.
9. Nozik, A. J., *Phy. E* **2002,** 14, 115-120.
10. Deschler, F., et al., *J. Phys. Chem. Lett.* **2014,** 5, 1421-1426.
11. Stamplecoskie, K. G.; Manser, J. S.; Kamat, P. V., *Energy Environ. Sci.* **2015**.
12. Era, M.; Morimoto, S.; Tsutsui, T.; Saito, S., *Appl. Phys. Lett.* **1994,** 65, 676-678.
13. Chondroudis, K.; Mitzi, D. B., *Chem. Mater.* **1999,** 11, 3028-3030.
14. Hattori, T.; Taira, T.; Era, M.; Tsutsui, T.; Saito, S., *Chemical Physics Letters* **1996,** 254, 103-108.
15. Era, M.; Morimoto, S.; Tsutsui, T.; Saito, S., *Synthetic Metals* **1995,** 71, 2013-2014.
16. Tan, Z.-K., et al., *Nat. Nanotechnol.* **2014,** 9, 687-692.
17. Kim, Y.-H.; Cho, H.; Heo, J. H.; Kim, T.-S.; Myoung, N.; Lee, C.-L.; Im, S. H.; Lee, T.-W., *Adv. Mater.* **2014,** 27, 1248-1254.
18. Schmidt, L. C.; Pertegas, A.; Gonzalez-Carrero, S.; Malinkiewicz, O.; Agouram, S.; Minguez Espallargas, G.; Bolink, H. J.; Galian, R. E.; Perez-Prieto, J., *J. Am. Chem. Soc.* **2014,** 136, 850-853.
19. Hanusch, F. C., et al., *J. Phys. Chem. Lett.* **2014,** 5, 2791-2795.
20. Mitzi, D. B., *J. Chem. Soc., Dalton Trans.* **2001**, 1-12.
21. Eperon, G. E.; Stranks, S. D.; Menelaou, C.; Johnston, M. B.; Herz, L. M.; Snaith, H. J., *Energy Environ. Sci.* **2014,** 7, 982-988.

22. Wehrenfennig, C.; Liu, M.; Snaith, H. J.; Johnston, M. B.; Herz, L. M., *Energy Environ. Sci.* **2014,** 7, 2269-2275.
23. Stranks, S. D.; Burlakov, V. M.; Leijtens, T.; Ball, J. M.; Goriely, A.; Snaith, H. J., *Physical Review Applied* **2014,** 2, 034007.
24. Vak, D.; Kim, S.-S.; Jo, J.; Oh, S.-H.; Na, S.-I.; Kim, J.; Kim, D.-Y., *Appl. Phys. Lett.* **2007,** 91, 081102-081102-3.
25. Green, R.; Morfa, A.; Ferguson, A. J.; Kopidakis, N.; Rumbles, G.; Shaheen, S. E., *Appl. Phys. Lett.* **2008,** 92, 033301-033301-3.
26. Wang, Y.-M.; Teng, F.; Hou, Y.-B.; Xu, Z.; Wang, Y.-S.; Fu, W.-F., *Appl. Phys. Lett.* **2005,** 87, 233512-233512-3.
27. Matyba, P.; Maturova, K.; Kemerink, M.; Robinson, N. D.; Edman, L., *Nat. Mater.* **2009,** 8, 672-676.
28. Slinker, J. D., et al., *Nat. Mater.* **2007,** 6, 894-899.
29. Malliaras, G. G., et al., *Nat. Mater.* **2008,** 7, 168-168.
30. van Reenen, S.; Akatsuka, T.; Tordera, D.; Kemerink, M.; Bolink, H. J., *J. Am. Chem. Soc.* **2012,** 135, 886-891.
31. Meier, S. B.; van Reenen, S.; Lefevre, B.; Hartmann, D.; Bolink, H. J.; Winnacker, A.; Sarfert, W.; Kemerink, M., *Adv. Funct. Mater.* **2013,** 23, 3531-3538.
32. Tordera, D.; Meier, S.; Lenes, M.; Costa, R. D.; Ortí, E.; Sarfert, W.; Bolink, H. J., *Adv. Mater.* **2012,** 24, 897-900.

6 Light-Emitting Electrochemical Cells based on All-Inorganic Perovskite Nanocrystals

This chapter is based on the following publication:

Meltem F. Aygüler, Bianka M. D. Puscher, Yu Tong, Thomas Bein, Alexander S. Urban, Rubén D Costa and Pablo Docampo, *Journal of Physics D:Applied Physics*, 2018, 21, 334001.

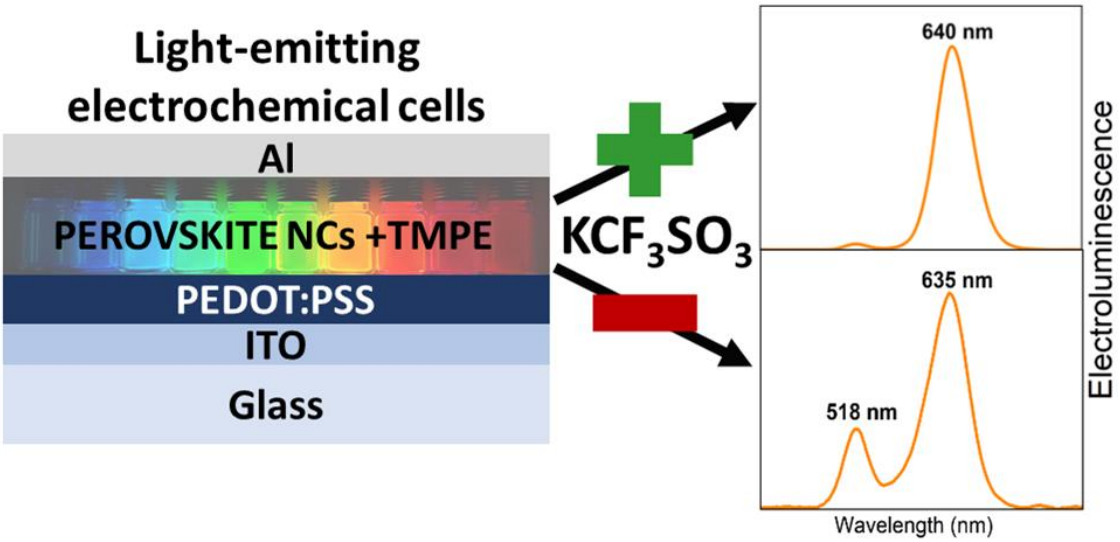

Keywords

All-inorganic perovskite nanocrystals, thin-film lighting devices, light-emitting electrochemical cells, salt additives

6.1 Introduction

Hybrid organic-inorganic (HOIP, $CH_3NH_3PbX_3$, X = Cl, Br, I) and all-inorganic lead halide perovskite ($CsPbX_3$) materials have the potential to revolutionize both photovoltaic and lighting technologies.[1-4] However, the decomposition of the HOIP into PbX_2 and volatile products, such as CH_3NH_2, HI and I_2 due to the low lattice energy, has shifted the attention to the all-inorganic perovskite nanocrystals (NCs). These are more stable to degradation induced by moisture, oxygen, heat, light or combined effects thereof than their hybrid counterparts.[5-6] Therefore, the interest in these NCs has been at high levels after the first demonstration of their synthesis by Protesescu *et al.*[6-9]

The remarkable photoluminescence (PL) properties and simple synthetic routes of all-inorganic perovskite NCs have already established their place in lighting applications.[10-11] They exhibit narrow size distributions as well as narrow PL emission bands with a full width at half maximum (FWHM) of 12-50 nm[5] along with high PL quantum yields (PLQYs) up to 95-100%.[6-7, 12] Furthermore, this class of NCs exhibits high defect tolerance, meaning that they are highly luminescent without any further electronic surface passivation, whereas such passivation is obligatory to obtain a high PLQY from conventional quantum dots (QDs) based on metal chalcogenides or metal pnictides.[5, 13] Additionally, tunable band gaps *via* quantum confinement or simple changes in composition as well as the solution processability have revealed their potential in light-emitting electrochemical cells (LECs), consisting of an active layer sandwiched between two electrodes.[5-6, 14-16]

Recently, the incorporation of conventional QDs in LECs was successfully demonstrated.[17-19] Inspired by these findings, we fabricated the first LECs based on HOIP NCs using an up-scalable spray-coating technique.[20] These devices showed luminance of 1-2 cd/m^2 at injection voltages of 11-12 V. Additionally, we demonstrated the important role of the electrolyte matrix in the device operating mechanism, as devices without this component displayed no detectable luminance. Moreover, the devices were analyzed by applying both constant voltage and pulsed current driving schemes, showing that LECs based on HOIP and all-inorganic NCs follow a common LEC behavior.[20-21]

Here, we show the successful synthesis of all-inorganic $CsPbX_3$ perovskite NCs *via* the hot injection method as well as their application in lighting schemes following the LEC concept. LECs were fabricated by blending the $CsPbX_3$ NCs with an ionic polyelectrolyte comprised of trimethylolpropane ethoxylate (TMPE) and KCF_3SO_3. These devices featured a luminance of 8 cd/m^2 for mixed halide $CsPb(Br/I)_3$ NCs at low injection voltages of 4 V unlike their hybrid

counterparts, which require injection voltages of around 11-12 V. Additionally, the spectral electroluminescence (EL) width of the devices (~30 nm) is narrower than that of the HOIP based NCs (~150 nm), owing to the homogeneous size distribution and superior structure stability of the all-inorganic NCs. We also show that the addition of the salt KCF_3SO_3 enhances the device performance due to improved carrier injection and suppresses halide segregation in mixed halide systems with further stabilization of the lattice by potassium cations. As a result, we believe that all-inorganic perovskite NC-based LECs provide an alternative route to circumvent complicated fabrication processes of other perovskite-based lighting devices.

6.2 Results

6.2.1 Synthesis and Characterization of $CsPbX_3$ NCs

We synthesized $CsPbX_3$ NCs (X = I, Br, Cl) following the hot injection method, where the previously prepared cesium-oleate solution was reacted with a warm solution of the PbX_2 in a high boiling solvent (octadecene) at 170 °C (for details, see Experimental Section).[6] OLA and OA were added to the reaction flask to dissolve PbX_2 and to stabilize the NCs. Mixed-halide perovskite NCs were prepared by mixing the appropriate ratios of PbX_2 salts. Photos of the NC dispersions under UV light are displayed in Figure 6.1A.

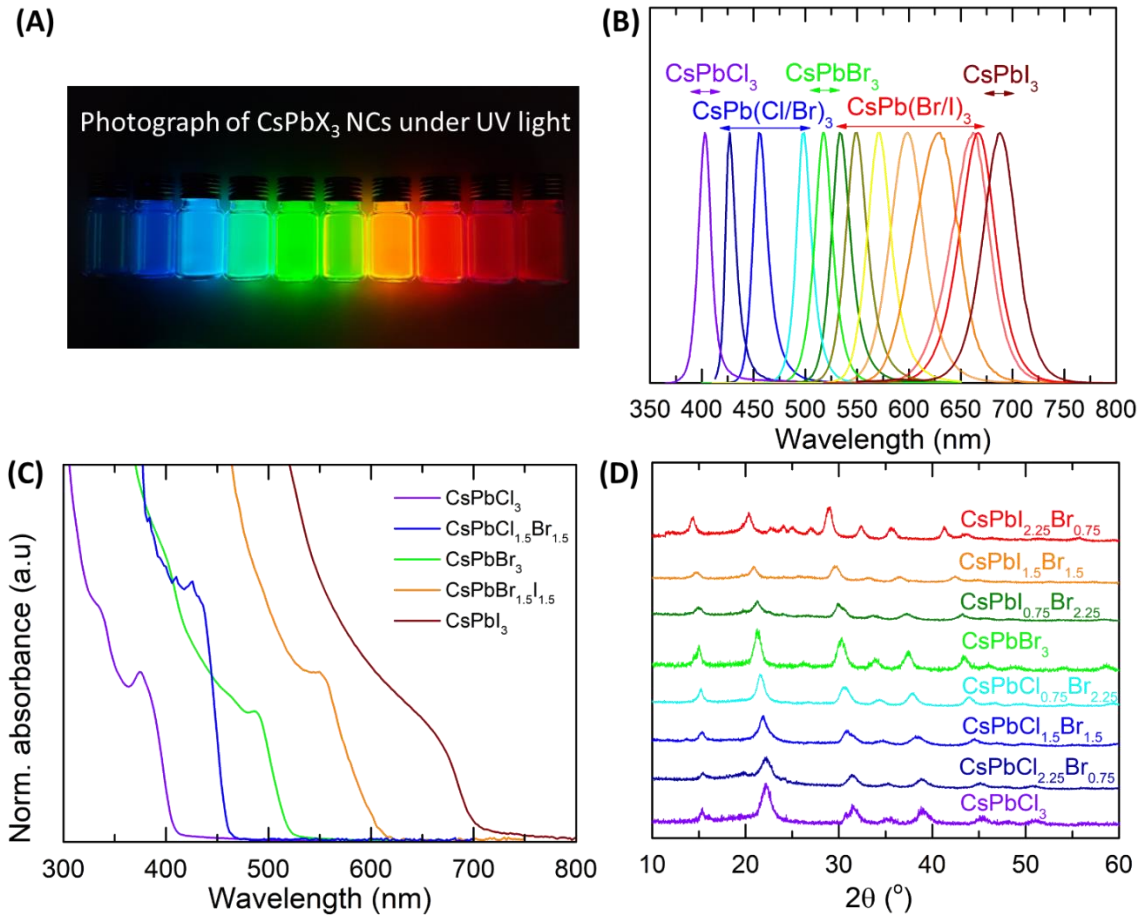

Figure 6.1 (A) Photographs of NC dispersions with different halide composition under UV-illumination (366 nm) and their corresponding (B) PL spectra, (C) UV-VIS spectra and (D) XRD patterns.

We investigated the optical features of the NCs in detail by obtaining steady-state PL and absorption spectra of their dispersions (Figure 6.1B and C). Importantly, both can be tuned over the entire visible spectral region by changing the halide ratio during the synthesis. Notably, all samples exhibit sharp band edges in the absorption spectra. Additionally, the dispersions all showed narrow emission line widths of 11-48 nm (Table 6.1) and high PLQYs of 40-80%, whereby the low PLQYs (<50%) belong to chloride-based NCs. Furthermore, the high PLQYs suggest that surface dangling bonds do not play a significant role in the emission. We emphasize that the photostability of $CsPbBr_3$ NCs in solution is exceedingly high. Under continuous excitation at 405 nm, only a small drop in PL intensity at the beginning of the measurement was observed, as seen in Figure 6.2. These results highlight the suitability of the NCs for lighting applications.

Table 6.1 Full width half maxima of PL measurements of $CsPbX_3$ NCs with different halide concentrations.

NCs	FWHM (nm)	NCs	FWHM (nm)
$CsPbCl_3$	14	**$CsPbBr_{1.75}I_{1.25}$**	26
$CsPbCl_{2.25}Br_{0.75}$	11	**$CsPbBr_{1.5}I_{1.5}$**	38
$CsPbCl_{1.5}Br_{1.5}$	17	**$CsPbBr_{1.25}I_{1.75}$**	49
$CsPbCl_{0.75}Br_{2.25}$	18	**$CsPbBr_1I_2$**	42
$CsPbBr_3$	21	**$CsPbBr_{0.75}I_{2.25}$**	40
$CsPbBr_{2.25}I_{0.75}$	21	**$CsPbI_3$**	37
$CsPbBr_2I_1$	24		

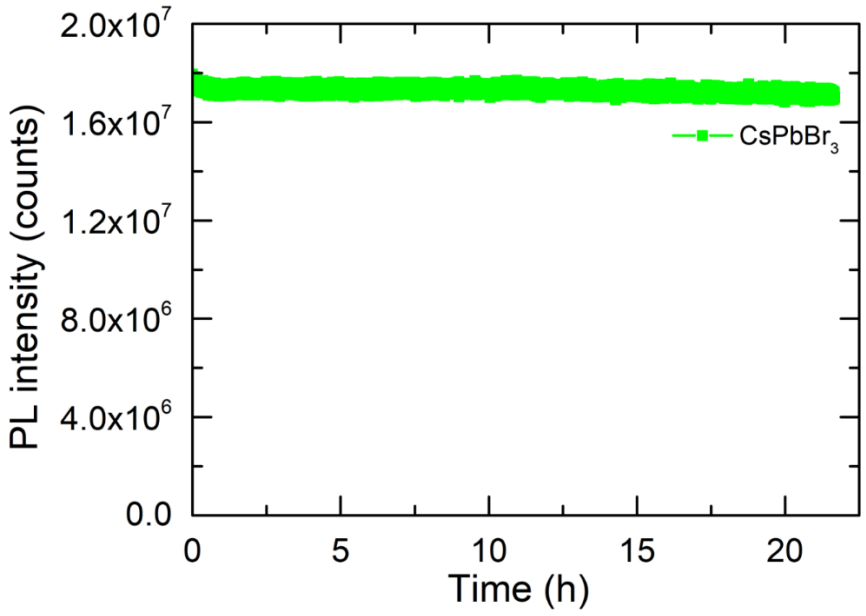

Figure 6.2 The photostability of $CsPbBr_3$ NCs under 405 nm light excitation.

Cesium-based lead halide perovskites are known to crystallize in orthorhombic, tetragonal and cubic polymorphs of the perovskite lattice.[6, 22-23] However, here X-ray diffraction (XRD) data show that all $CsPbX_3$ NCs are in the cubic phase (Figure 6.1D). The reflections in the XRD patterns are shifted due to the different unit cell sizes, resulting from variation of the halide component. As expected, upon incorporation of Cl^- the lattice shrinks, and all the peaks shift to higher angles while incorporation of I^- expands the cell and the peaks shift to lower angles due to

the larger unit cell. Furthermore, transmission electron microscopy (TEM) images not only confirm the high crystallinity of the NCs but also show the fairly homogeneous size distribution of the perovskite NCs (Figure 6.3).

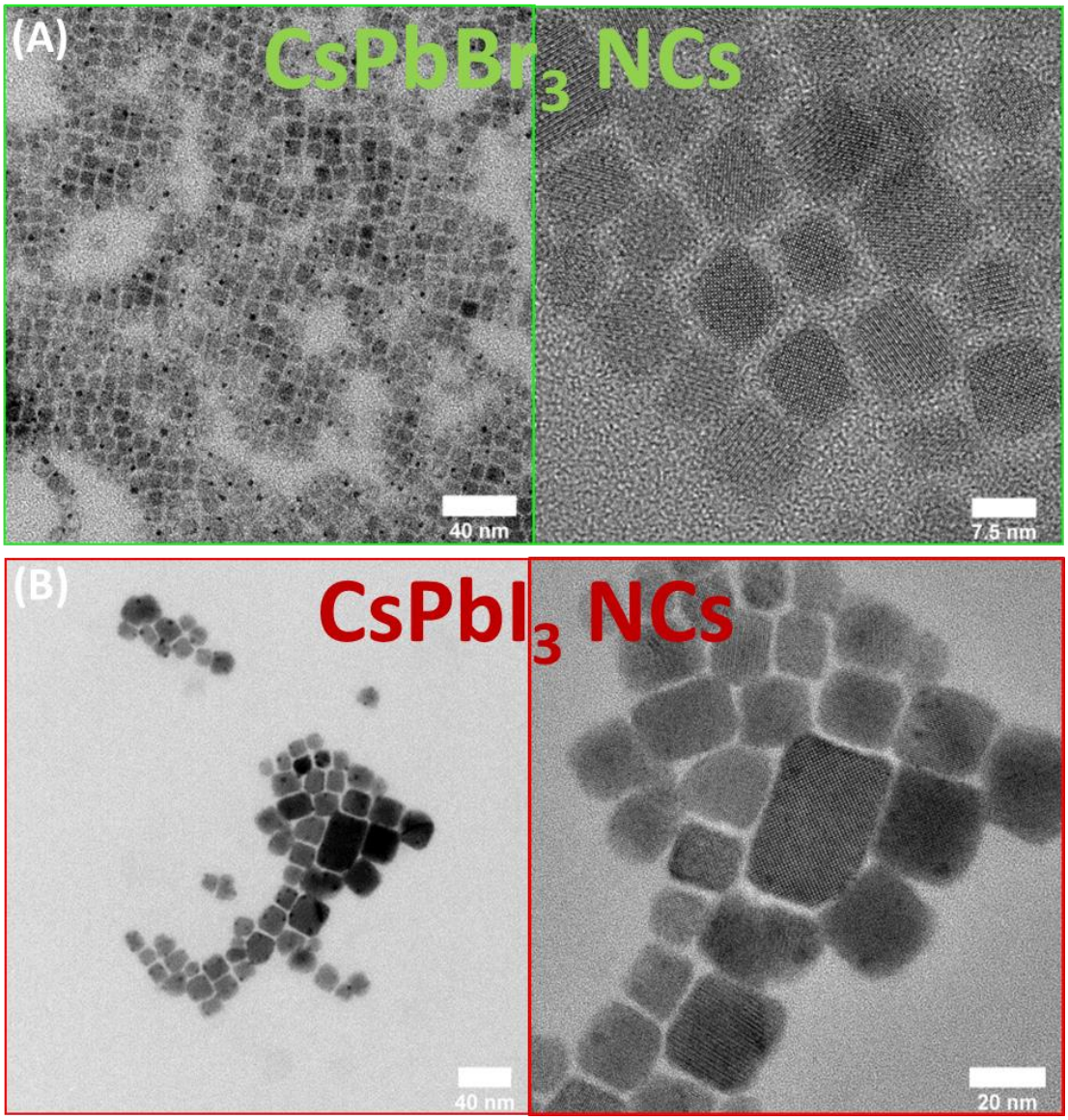

Figure 6.3 TEM images of (A) $CsPbBr_3$ and (B) $CsPbI_3$ NCs at different magnifications.

6.2.2 Fabrication of Light-Emitting Electrochemical Cells (LECs)

Taking advantage of the remarkable features of these perovskite NCs, we have successfully fabricated LECs. We initially purified the NCs by washing them with toluene once after the synthesis and found this process to be crucial for the formation of homogeneous films, as shown in AFM images in Figure 6.4. Whereas the films prepared from the non-purified NCs showed the

formation of micron-sized rods due to unreacted excess ligands in the solution, the films prepared with purified NCs possessed a homogeneous morphology without any visible rods. We have additionally analyzed the formed rods with TEM, resulting that they were formed by several NCs as seen in Figure 6.5. For device fabrication, we mixed the purified NCs with TMPE polymer and KCF_3SO_3 and spin-coated the solution on indium-doped tin oxide (ITO) coated glass substrates modified by the deposition of poly(3,4-ethylenedioxythiophene) polystyrene sulfonate (PEDOT:PSS). The devices were completed by thermal evaporation of aluminum (Al) serving as the top electrode. A schematic structure of these devices is shown in the inset of Figure 6.6 (see Experimental Section for further experimental details).

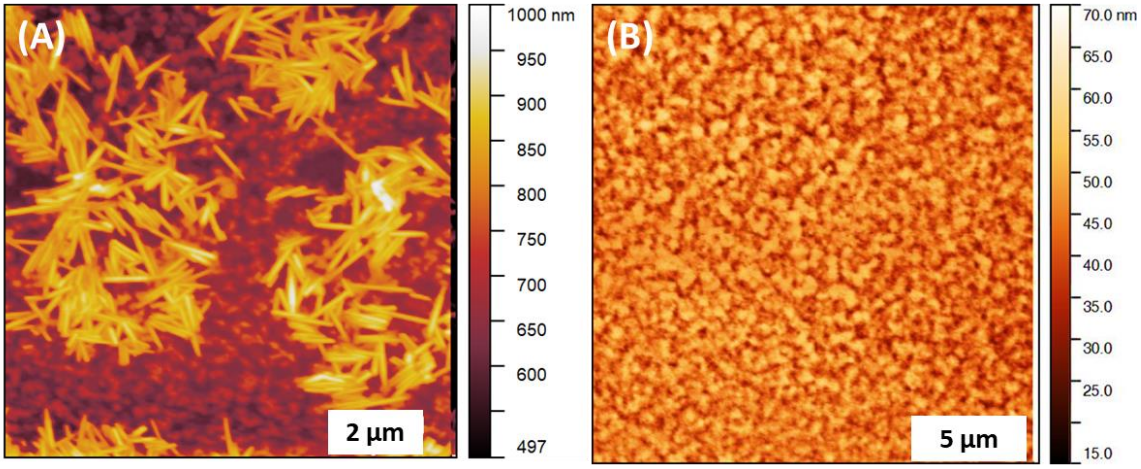

Figure 6.4 AFM images of the films prepared with $CsPbBr_3$ NCs (A) before and (B) after purification.

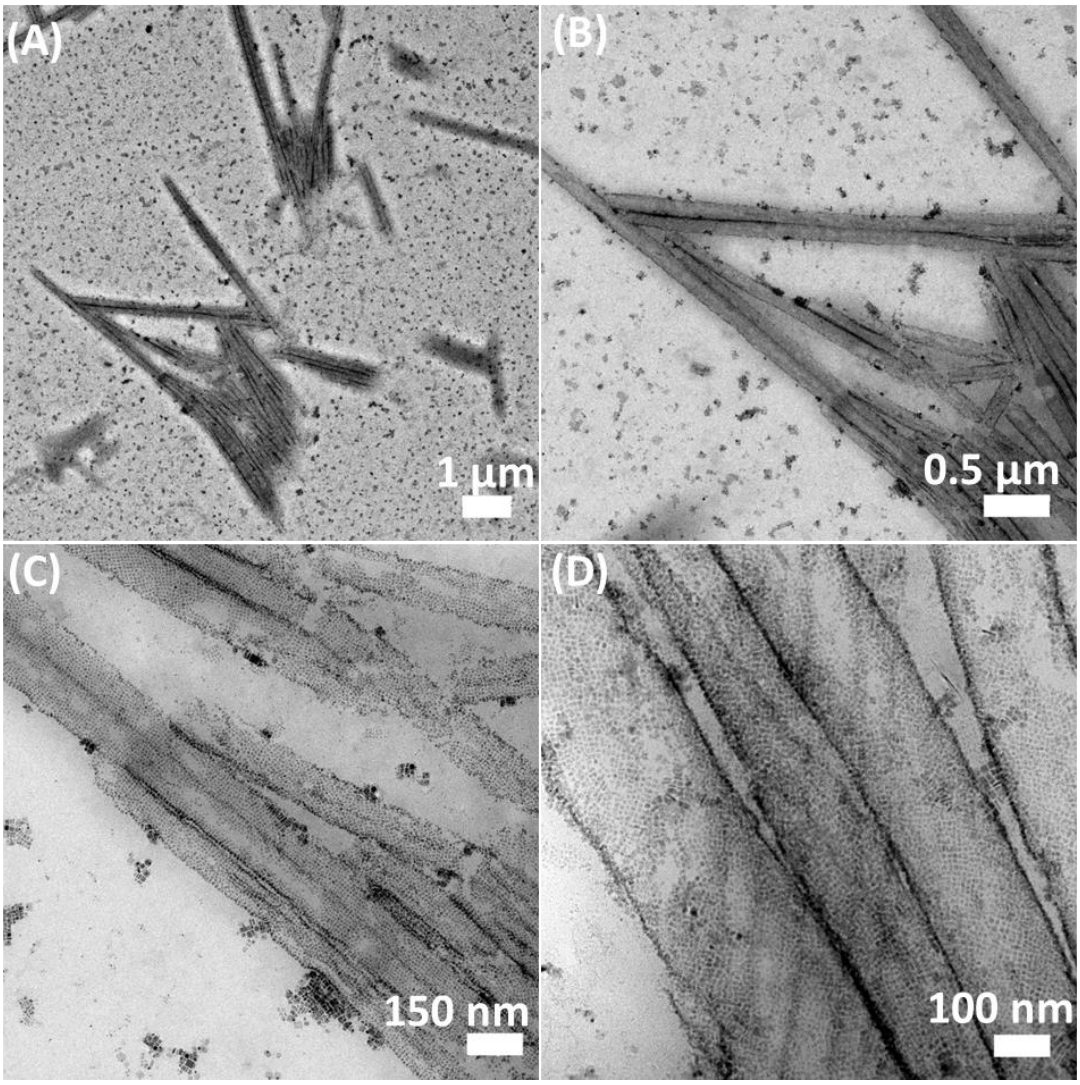

Figure 6.5 TEM images of rods at different magnifications: (A) 1 µm, (B) 0.5 µm, (C) 150 nm and (D) 100 nm.

To assess the quality of the all-inorganic NC-based LECs we compare their performance with that of our previously demonstrated HOIP perovskite NC-based LECs using methylammonium lead bromide ($MAPbBr_3$) NCs.[20] Corresponding luminance-current density *versus* applied voltage (LIV) plots are depicted in Figure 6.6B and D for the HOIP NCs and all-inorganic $CsPbBr_3$ without any purification, respectively. The LIV assays show an injection voltage of around 4 V with a maximum luminance of 5.4 cd/m^2 for the $CsPbBr_3$ NC based LECs. In comparison, the HOIP-LECs display an injection voltage around 12 V with a maximum luminance of 1.4 cd/m^2. Additionally, the inorganic NCs show very sharp and narrow EL spectra in stark contrast to the very broad EL emission of the HOIP-LECs (Figure 6.6A and C). This highlights some of the advantages of all-inorganic perovskites for LEC devices.

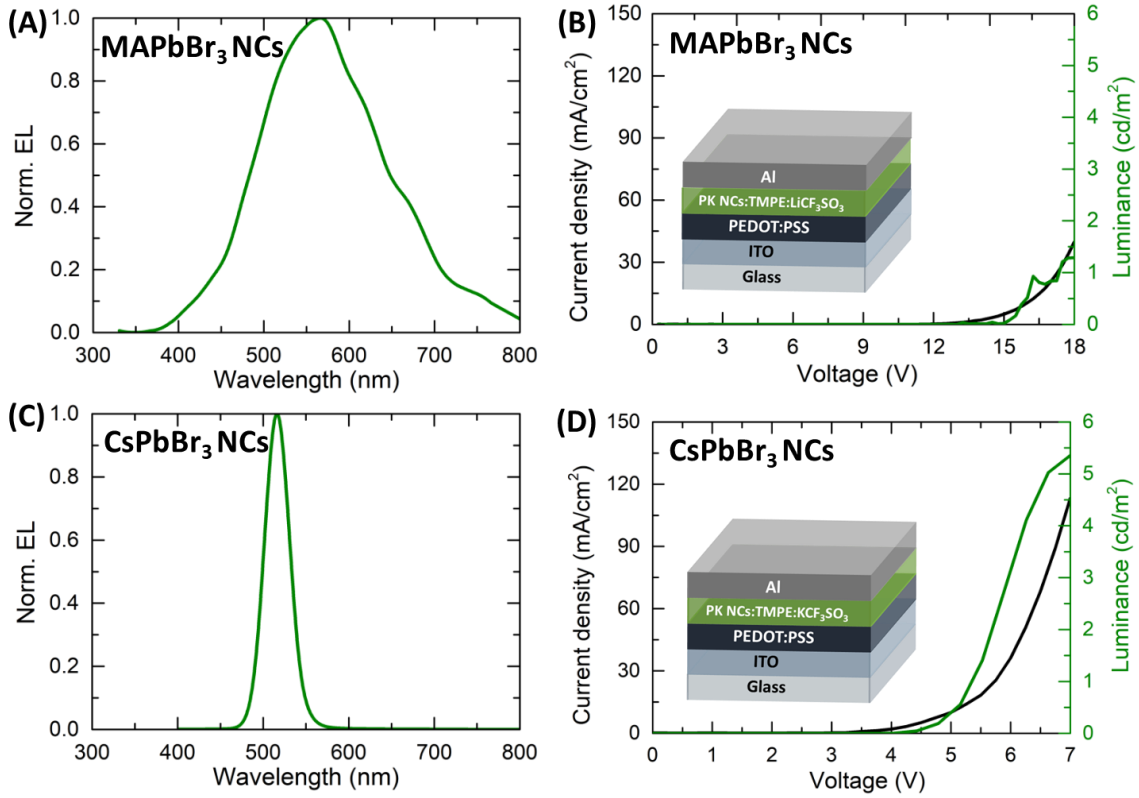

Figure 6.6 EL spectra (left) and luminance-current density *versus* applied voltage characterization (right) of LECs with (A, B) $MAPbBr_3$ NCs[20] and (C, D) $CsPbBr_3$. The insets in B and D show the architecture of LECs used in this work.

In general, the main reason for the rather low performance of single-layer devices is still unknown, but it has been tentatively attributed to the electrochemical stability with respect to i) halide segregation and ii) formation of hot spots located at surface defects where non-radiative electron-hole recombination occurs.[24] Therefore, some passivation is still needed to achieve stable devices.[24-26]

Here, we found that devices with mixed halide perovskite compositions exhibit different behavior in the case that the salt KCF_3SO_3 is added to the purified NC and TMPE polymer mixture (Figure 6.7). To study this effect, we focused on LECs with $CsPbBr_{1.25}I_{1.75}$ NCs. Here, devices without the salt exhibited an EL emission with a maximum at 640 nm and a secondary peak at 520 nm (Figure 6.7A) evolved upon applying a high voltage (7 V) and low luminance of <1 cd/m^2 (Figure 6.7B). The low brightness of the devices is due to the reduced ionic mobility in the active layer and the lack of efficient electron-hole recombination. This is a result of the working principle of LECs, as ionic polyelectrolytes without salt do not control the growing doped regions near the electrodes. On the other hand, devices with mobile ions show an injection voltage of around 4 V

as well as a luminance of 8 cd/m^2 along with an EL spectrum centered at 640 nm up to an applied bias of 10 V (Figure 6.7C and D). Moreover, 3D EL of these devices can be seen in Figure 6.8.

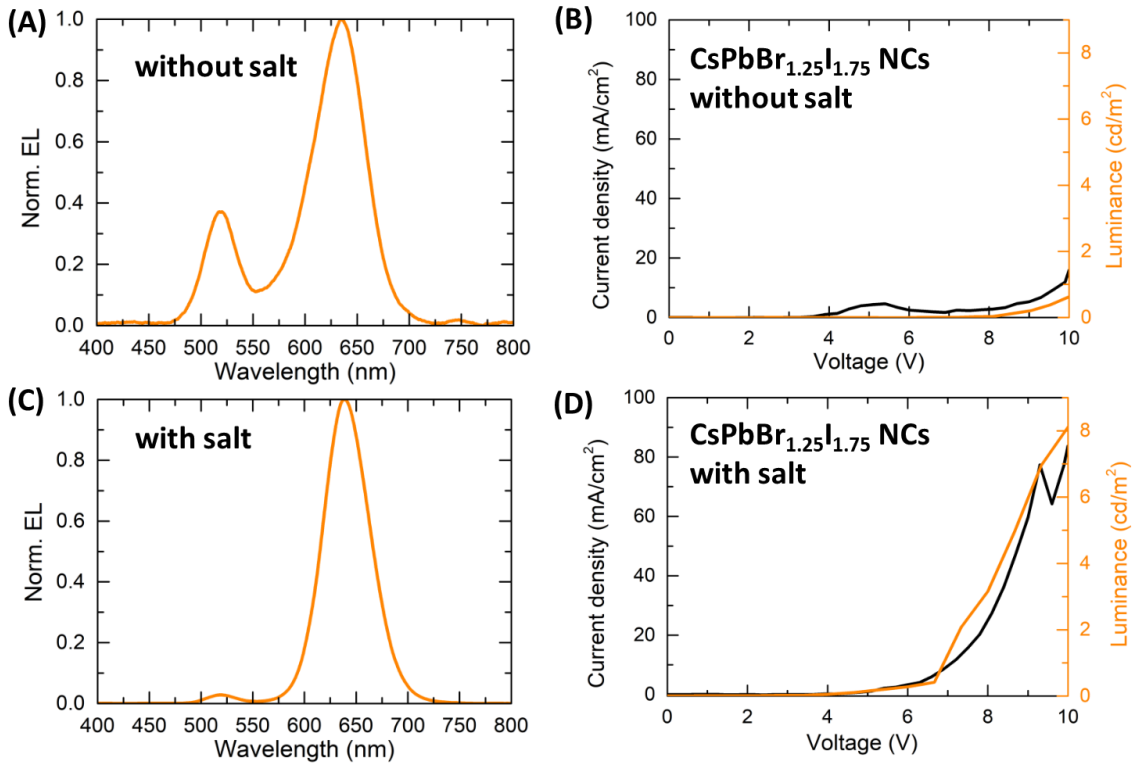

Figure 6.7 EL of the LECs comprised of $CsPbBr_{1.25}I_{1.75}$ NCs (A) without salt and (C) with salt (KCF_3SO_3). LIV characterization of the same devices (B) without salt and (D) with salt at 10 V.

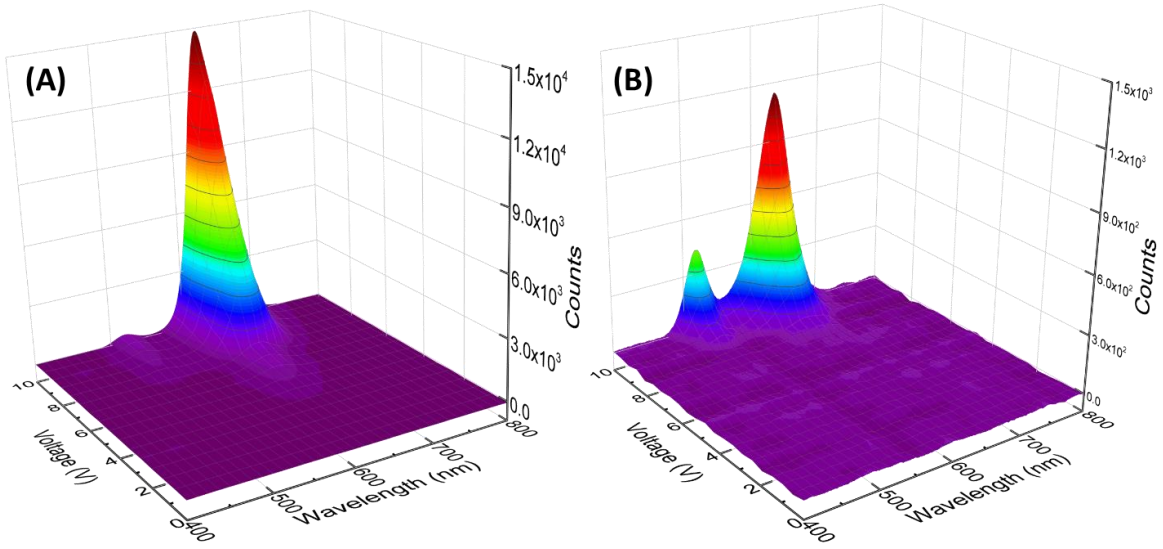

Figure 6.8 3D EL of the devices in Figure 6.7 (A) with and (B) without salt (KCF_3SO_3).

6.3 Discussion

The working principle of LECs is based on a p-i-n junction, where the ions accumulate at the electrode interfaces once a voltage is applied. The doped regions grow with time, leading to the formation of a p-i-n junction between them and the drop in the applied potential triggers the charge recombination and light emission.[16, 27] Therefore, an optimized salt concentration balances the space charge effects at the interfaces, improving the conductivity of the layer by electrochemical doping and increasing the current density as well as the recombination rate in devices.[28-31] For perovskite NC-based LECs, the addition of salt, KCF_3SO_3, analogously provides small, mobile ions that can accumulate in high concentrations near the electrodes. Therefore, the improvements in injection voltage and luminance values are rationalized in terms of balanced charge carrier injection after increased redistribution of ionic space charges, confirming the results of Li *et al.* who demonstrated a single layer light-emitting diode using a perovskite/poly(ethylene oxide) composite film with a low turn-on voltage thanks to the ionic conductivity of the film and thus the formation of a p-i-n homojunction.[32]

Our results show that all-inorganic perovskite-based LECs outperform their HOIP NC-based counterparts, both in terms of injection voltages and total luminance.[20] The improvement in the luminance values can be attributed to the significantly higher PLQYs of the all-inorganic NCs (40-80%), in comparison to only 5-15% obtained from HOIP NCs in our previous work. Additionally, time-resolved PL measurements indicate that the inorganic perovskite NCs exhibit significantly higher radiative recombination rates, as the PL lifetimes in the HOIP NCs are longer despite a significantly lower quantum yield, as shown in Figure 6.9.

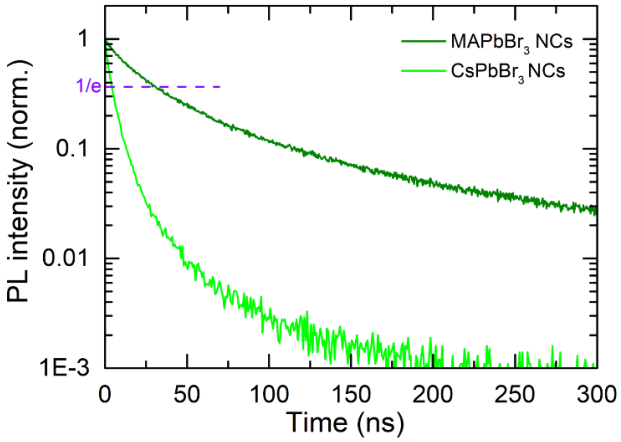

Figure 6.9 Time-resolved PL spectra of HOIP ($MAPbBr_3$) and fully inorganic ($CsPbBr_3$) perovskite NCs in solution. The decay times ($\tau_{1/e}$) are 30.9 and 4.3 ns for $MAPbBr_3$ and $CsPbBr_3$ NCs, respectively.

Interestingly, we observe lower injection voltages in all-inorganic LECs, which we attribute to the higher conductivity of inorganic perovskite $CsPbBr_3$ NCs than HOIP ones.[21] Additionally, the striking difference in the FWHM of the EL spectra between LECs based on the HOIP NCs and all-inorganic NCs is likely due to their large distribution in size of the former that causes degradation of the active layer upon application of the electric field and changes of the spatial light distribution. Thus, this finding suggests that inorganic perovskite NCs are more stable and maintain the same spectral shape in the devices.

Mixed halide perovskites are known to exhibit halide segregation upon illumination.[33-34] We have also observed the same phenomenon with the application of voltage in our devices.[35] However, it is noteworthy that this can be overcome with the incorporation of the salt KCF_3SO_3. This may be due to the fact that the small K^+ cation can find a place in the cystal structure and cause a contraction of the PbX_6 octahedral volume, thus improving the phase stability as Nam et al. reported for $CsPbI_2Br_1$ perovskite with the incorporation of KI.[36] Calculations have demonstrated that the K^+ ions preferentially locate on interstitial sites rather than on substitutional sites due to energetic reasons.[37-38] Thus, in light of these observations, the inclusion of K^+ cations in the active layer seems to prevent halide segregation by occupying intersititial sites.

6.4 Conclusion

In this work, we have successfully synthesized all-inorganic perovskite NCs with different halide compositions *via* a hot injection method. These NCs show high PLQYs and narrow PL emission as well as a rather narrow size distribution. Taking advantage of the excellent optoelectronic properties of these NCs, we have fabricated working LECs. Furthermore, we demonstrate an enhancement of luminance values of LECs based on inorganic perovskite NCs as well as a decrease in the injection voltages from 7 V to 4 V with the addition of a KCF_3SO_3 salt, which we attribute to improved control of space charge effects and balanced carrier injection. Our results also show that the salt helps to stabilize the perovskite structure in mixed halide systems by suppressing halide segregation. Moreover, our results suggest that all-inorganic perovskite NCs are more efficient than hybrid organic-inorganic perovskite NCs due to their higher PLQYs and narrower size distribution. Therefore, we believe that the use of all-inorganic perovskite NCs in LECs shows promising potential for the development of efficient lighting technologies with single layer solution-processable devices.

6.5 Experimental Section

6.5.1 Synthesis of $CsPbX_3$ NCs and characterization details

The NCs were synthesized according to a published report by Protesescu *et al.*[6] All chemicals except olelylamine (OLA) were purchased from Sigma Aldrich and used as received. OLA (approximate C_{18}-content 80-90%) was purchased from Acros Organics.

Cs-oleate was prepared by following procedure: Cs_2CO_3 (0.814 g), octadecene (ODE, 40 mL) and oleic acid (OA, 2.5 mL) were loaded into a 250 ml 3-neck flask and dried under vacuum for 1 h at 120 ^oC. Then, the solution was heated under N_2 to 150^oC until Cs_2CO_3 reacted with OA.

OLA and OA were dried under vacuum for 2 h at 120 ^oC before use. ODE (10 mL) and PbX_2 (0.376 mmol, X=Cl, Br, I) or mixtures of the lead halide salts were loaded into a 100 ml 3-neck flask and dried under vacuum for 1 h at 120 ^oC. Dried OLA (1 mL) and OA (1 mL) were injected into the flask at 120 ^oC under a N_2 atmosphere. After all PbX_2 was solubilized, the temperature was increased to 140-200 ^oC, the Cs-oleate solution (0.8 mL, prepared as described above) was quickly injected and the reaction mixture was then rapidly cooled by an ice-water bath. In the synthesis of $CsPbCl_3$ NCs, the higher temperature of 150 ^oC and 1 mL of trioctylphosphine (TOP, Fluka) were necessary to solubilize the lead salt. The resulting solution was centrifuged at 10000 rpm for 10 min and the solids were redispersed in 1 mL toluene. The NCs were centrifuged at 12000 rpm for 10 min and the precipitate was used for the fabrication of LECs.

The powder XRD measurements were performed using a Cu-$K_{\alpha 1}$-source on a G670 Imaging Plate Guinier Diffractometer (Huber Diffraktionstechnik GmbH & Co. KG) . Steady-state absorption spectra were measured with a Lambda 1050 UV-VIS spectrophotometer (PerkinElmer, Inc.) using an integrating sphere. Steady-state photoluminescence measurements were performed with a Fluotime 300 spectrofluorometer (Picoquant GmbH). The excitation wavelength was fixed at 405 nm. TEM measurements were performed with a JEM-2011 (JEOL GmbH) equipped with LaB6 operated at 200 kV and an EDS (EDAX) detector. AFM characterization was performed under ambient conditions using a NANOINK atomic force microscope with Si n-type tip with a radius of <10 nm in tapping mode with a scan rate of 0.2 Hz, a proportional gain of 50 and an integral gain of 30. The PLQYs were measured using an integrating sphere in a Fluorolog-3 FL3-22 (Horiba Jobin Yvon GmbH) spectrometer. For the photostability measurements, a colloidal solution of $CsPbBr_3$ NCs was continuously illuminated at an excitation of 405 nm, and the intensity of the PL maxima (515 nm) was recorded as a function of excitation time.

6.5.2 Fabrication of LECs and Characterization Details

ITO-coated glass substrates were patterned by etching with zinc powder and an HCl solution (3 M). The substrates were washed with deionized water and a 2% Hellmanex detergent solution. They were consecutively cleaned with deionized water, acetone, and ethanol and dried by pressurized air. The substrates were further cleaned with 2-propanol before the deposition of PEDOT:PSS. PEDOT:PSS (Heraeus) was diluted with 2-propanol at a ratio of 1:2 and this solution was spin-coated (dynamic dispense) on ITO substrates at 2000 rpm for 45 s. The layers (50-60 nm) were annealed at 120 ºC for 10 min. The precipitate from the purification of NCs was used for creating the active layer. 0.25 mL of trimethylolpropane ethoxylate (TMPE, 5 mg/mL in hexane) was added to the NCs. Thereafter, 5 µL of KCF_3SO_3 (1 mg/mL in THF) was added to the mixture of polymer and NCs. This mixture was deposited on PEDOT:PSS layers via spin-coating (static dispense) at 1000 rpm for 30 s, resulting in a thickness of 60-70 nm. The aluminum cathode (90 nm) was thermally evaporated using a shadow mask under high vacuum ($<1\times10^{-6}$ mbar) using a Covap evaporator (Angstrom Engineering) integrated into the inert atmosphere glovebox. Current density and luminance *versus* voltage were measured using an Avaspec-ULS2048LTEC spectrophotometer (Avantes) calibrated with a white LED in conjunction with 1916-c optical power meter (Newport Corporation) equipped with a calibrated silicon diode and an OLT OLED Lifetime-Test System (Botest Systems GmbH). The EL spectrum was recorded using the above-mentioned Avantes spectrophotometer.

6.6 References

1. Xiao, Z.; Kerner, R. A.; Zhao, L.; Tran, N. L.; Lee, K. M.; Koh, T.-W.; Scholes, G. D.; Rand, B. P., *Nat. Photonics* **2017,** 11, 108.
2. Kim, Y.-H.; Cho, H.; Heo, J. H.; Kim, T.-S.; Myoung, N.; Lee, C.-L.; Im, S. H.; Lee, T.-W., *Adv. Mater.* **2014,** 27, 1248-1254.
3. Tan, Z.-K., et al., *Nat. Nanotechnol.* **2014,** 9, 687-692.
4. Saliba, M., et al., *Energy Environ. Sci.* **2016,** 9, 1989-1997.
5. Huang, H.; Bodnarchuk, M.; Kershaw, S. V.; Kovalenko, M. V.; Rogach, A. L., *ACS Energy Lett.* **2017,** 2, 2071-2083.
6. Protesescu, L.; Yakunin, S.; Bodnarchuk, M. I.; Krieg, F.; Caputo, R.; Hendon, C. H.; Yang, R. X.; Walsh, A.; Kovalenko, M. V., *Nano Lett.* **2015,** 15, 3692-3696.
7. Tong, Y., et al., *Angew. Chem. Int. Ed.* **2016,** 55, 13887-13892.
8. Akkerman, Q. A.; D'Innocenzo, V.; Accornero, S.; Scarpellini, A.; Petrozza, A.; Prato, M.; Manna, L., *J. Am. Chem. Soc.* **2015,** 137, 10276-10281.
9. Sun, S.; Yuan, D.; Xu, Y.; Wang, A.; Deng, Z., *ACS Nano* **2016,** 10, 3648-3657.
10. Song, J.; Li, J.; Li, X.; Xu, L.; Dong, Y.; Zeng, H., *Adv. Mater.* **2015,** 27, 7162-7167.
11. Li, G., et al., *Adv. Mater.* **2016,** 28, 3528-3534.
12. Protesescu, L., et al., *ACS Nano* **2017,** 11, 3119-3134.
13. Haque, A.; Ravi, V. K.; Shanker, G. S.; Sarkar, I.; Nag, A.; Santra, P. K., *J. Phys. Chem. C* **2017**.
14. Yao, E.-P.; Yang, Z.; Meng, L.; Sun, P.; Dong, S.; Yang, Y.; Yang, Y., *Adv. Mater.* **2017,** 29, 1606859.
15. Polavarapu, L.; Nickel, B.; Feldmann, J.; Urban, A. S., *Adv. Energy Mater.* **2017,** 7, 1700267.
16. Costa, R. D.; Orti, E.; Bolink, H. J.; Monti, F.; Accorsi, G.; Armaroli, N., *Angew. Chem. Int. Ed.* **2012,** 51, 8178-8211.
17. Qian, G.; Lin, Y.; Wantz, G.; Davis, A. R.; Carter, K. R.; Watkins, J. J., *Adv. Funct. Mater.* **2014,** 24, 4484-4490.
18. Bader, A. J. N.; Ilkevich, A. A.; Kosilkin, I. V.; Leger, J. M., *Nano Lett.* **2011,** 11, 461-465.
19. Frohleiks, J.; Wepfer, S.; Kelestemur, Y.; Demir, H. V.; Bacher, G.; Nannen, E., *ACS Appl. Mater. Interfaces* **2016,** 8, 24692-24698.
20. Aygüler, M. F.; Weber, M. D.; Puscher, B. M. D.; Medina, D. D.; Docampo, P.; Costa, R. D., *J. Phys. Chem. C* **2015,** 119, 12047-12054.

21. Puscher, B. M. D.; Aygüler, M. F.; Docampo, P.; Costa, R. D., *Adv. Energy Mater.* **2017,** 7, 1602283.
22. Nedelcu, G.; Protesescu, L.; Yakunin, S.; Bodnarchuk, M. I.; Grotevent, M. J.; Kovalenko, M. V., *Nano Lett.* **2015,** 15, 5635-5640.
23. Stoumpos, C. C.; Malliakas, C. D.; Kanatzidis, M. G., *Inorg. Chem.* **2013,** 52, 9019-9038.
24. Zhang, X., et al., *J. Phys. Chem. Lett.* **2016,** 7, 4602-4610.
25. Yang, D.; Li, X.; Zeng, H., *Adv. Mater. Interf.* **2018,** 5, 1701662.
26. Wang, S.; Bi, C.; Yuan, J.; Zhang, L.; Tian, J., *ACS Energy Lett.* **2018,** 3, 245-251.
27. Pei, Q.; Yu, G.; Zhang, C.; Yang, Y.; Heeger, A. J., *Science* **1995,** 269, 1086-1088.
28. Bastatas, L. D.; Lin, K.-Y.; Moore, M. D.; Suhr, K. J.; Bowler, M. H.; Shen, Y.; Holliday, B. J.; Slinker, J. D., *Langmuir* **2016,** 32, 9468-9474.
29. Suhr, K. J.; Bastatas, L. D.; Shen, Y.; Mitchell, L. A.; Holliday, B. J.; Slinker, J. D., *ACS Appl. Mater. Interfaces* **2016,** 8, 8888-8892.
30. Shen, Y.; Kuddes, D. D.; Naquin, C. A.; Hesterberg, T. W.; Kusmierz, C.; Holliday, B. J.; Slinker, J. D., *Appl. Phys. Lett.* **2013,** 102, 203305.
31. Reenen, S. v.; Matyba, P.; Dzwilewski, A.; Janssen, R. A. J.; Edman, L.; Kemerink, M., *Adv. Funct. Mater.* **2011,** 21, 1795-1802.
32. Li, J.; Bade, S. G. R.; Shan, X.; Yu, Z., *Adv. Mater.* **2015,** 27, 5196-5202.
33. Hoke, E. T.; Slotcavage, D. J.; Dohner, E. R.; Bowring, A. R.; Karunadasa, H. I.; McGehee, M. D., *Chem. Sci.* **2015,** 6, 613-617.
34. Slotcavage, D. J.; Karunadasa, H. I.; McGehee, M. D., *ACS Energy Lett.* **2016,** 1, 1199-1205.
35. Li, G.; Price, M.; Deschler, F., *APL Mater.* **2016,** 4, 091507.
36. Nam, J. K.; Chai, S. U.; Cha, W.; Choi, Y. J.; Kim, W.; Jung, M. S.; Kwon, J.; Kim, D.; Park, J. H., *Nano Lett.* **2017,** 17, 2028-2033.
37. Yao, D.; Zhang, C.; Pham, N. D.; Zhang, Y.; Tiong, V. T.; Du, A.; Shen, Q.; Wilson, G. J.; Wang, H., *J. Phys. Chem. Lett.* **2018,** 9, 2113-2120.
38. Son, D.-Y.; Kim, S.-G.; Seo, J.-Y.; Lee, S.-H.; Shin, H.; Lee, D.; Park, N.-G., *J. Am. Chem. Soc.* **2018,** 140, 1358-1364.

7 Mechanically Stacked Perovskite/CIGS Tandem Solar Cells

Manuscript in preparation:

Meltem F. Aygüler*, Moritz Schultes*, Tim Helder, Alexander G. Hufnagel, Sebastian Häringer, Thomas Bein, Erik Ahlswede and Pablo Docampo

* These authors contributed equally to this work.

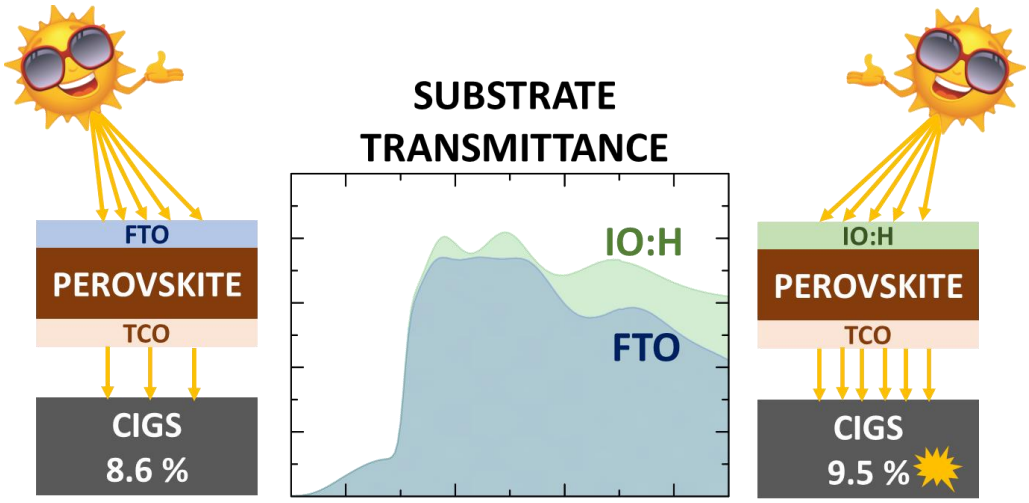

Keywords

Perovskite/CIGS tandem solar cells, transmittance, hydrogenated indium oxide, halide segregation

7.1 Introduction

Tandem solar cells offer avenues to overcome the Shockley-Queisser efficiency limit of single junction solar cells as well as a further path to reduce the cost per watt of solar electricity.[1-4] In these configurations, a more complete harvesting of the solar spectrum can be achieved by the absorption of high-energy photons in the top-cell, where the botttom-cell receives the transmitted low-energy photons.[4] Although a monolithic two-terminal (2-T) device is more practical and simple to fabricate, it requires sophisticated simultaneous optimization of several elements such as current matching between the device and a careful design of the full fabrication sequence in order not to damage the bottom-cell.[5] On the other hand, the development of practical tandem devices has been hampered due to the lack of appropriate wide-band gap top-cell materials to be integrated with existing photovoltaic cells at low cost.[3, 6]

In the last decade, hybrid halide perovskites have been developed as efficient absorber materials for solar cells, rivaling the efficiency of copper indium gallium selenide (CIGS), cadmium telluride (CdTe) and polycrystalline silicon (Si). The perovskites have become highly attractive for use in tandem solar cells due to their easy band gap tunability and solution processability on various substrates.[7] Unlike III-V semiconductors that suffer from lattice and thermal-expansion-coefficient mismatches as well as expensive vacuum-based film growth[8-9], halide perovskites offer versatile low-temperature deposition techniques such as spin-coating[10], doctor-blading[11], slot-die coating[12] on the bottom-cell without requiring any lattice matching thanks to their softness and defect-tolerance[4]. Therefore, perovskites have made significant progress in the past few years in their integration in tandem configurations.[7, 13-14]

A fundamental requirement for a successful tandem solar cell is the extraction of current at higher voltage from the top-cell than from the bottom-cell. In turn, this requires high radiative efficiency, a marked feature of the family of hybrid organic-inorganic perovskites, which allows certain perovskite blends to obtain lower voltage differences between the equivalent voltage of the band gap and V_{oc} than those of other thin-film devices such as CdTe, CIGS, organic and dye-sensitized solar cells.[15] However, this difference is much larger for many wide band gap halide perovskites (E_g > 1.6 eV) due to the photoinduced phase-segregation of the mixed halide perovskite systems, creating trap-forming iodide-rich domains and highly disordered bromide-containing perovskite blends.[3, 16]

The perovskite material layer is not the only critical optical layer in a semitransparent perovskite top-cell. In particular, the transmittance of the contacts plays a significant role in determining overall efficiency in tandems since they need to allow as many photons as possible in the long

wavelength region to reach the bottom device.[13] The typical requirement of transparent conductors for thin film solar cells is transmittance of 80% for wavelengths between 400-1100 nm. Additionally, all contacts must minimise voltage losses.[15]

In this work, we elucidated the transparency of perovskite top-cells employing the wide band gap perovskite, $Cs_{0.10}MA_{0.15}FA_{0.75}PbI_2Br$, with a band gap of 1.73 eV in a four-terminal (4-T) perovskite/CIGS tandem configuration. To this end, we have utilized different transparent conductive oxides (TCOs) for both substrate and back electrode in perovskite solar cells (PSCs). We find that the transmittance of the substrate is more critical than the back electrodes' transmittance to exploit the CIGS efficiency, obtaining 1 % more efficient CIGS solar cells with IO:H substrates due to the higher transmittance in the long wavelength region. Moreover, the cause of the low observed V_{oc} despite the wide band gap of the perovskite was unveiled by detecting compositional changes of the perovskites under illumination and bias in X-ray diffraction (XRD) measurements. Lastly, we suggest solutions to not only improve the efficiency of PSCs by improving design but also to overcome the V_{oc} deficiency by preventing halide segregation and better Fermi level alignment between valence band (VB) of perovskite and hole-transport material (HTL). Thus, we believe that our results will contribute to the development of novel tandem solar cells although there is still too much room to improve both *PCE* and V_{oc} values.

7.2 Fabrication of Mechanically Stacked Perovskite/CIGS Tandem Solar Cells

Theoretical simulations predict the highest efficiencies for tandem stacks when the band gap of the perovskite top-cell is in range of 1.70-1.85 eV.[1] Accordingly, we have chosen a perovskite composition of $Cs_{0.10}MA_{0.15}FA_{0.75}PbI_2Br$ which shows the absorbance spectra with a sharp band edge around 730 nm that corresponds to a band gap of 1.73 eV (Figure 7.1A), as estimated via a Tauc plot of direct band gap (inset of Figure 7.1A). We also confirmed the phase purity and crystallinity of the wide band gap perovskite by acquiring the X-ray diffraction (XRD) pattern of a perovskite thin film, shown in Figure 7.1B.

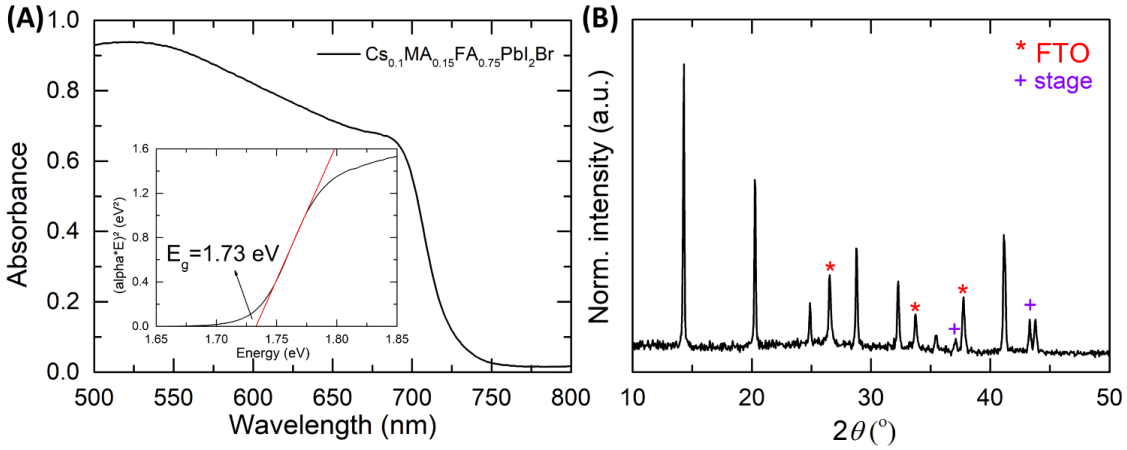

Figure 7.1 (A) Absorbance spectra of a wide band gap $Cs_{0.10}MA_{0.15}FA_{0.75}PbI_2Br$ perovskite on glass. The inset in (A) shows the corresponding Tauc plot. (B) XRD pattern of the wide band gap perovskite layer of identical composition on FTO/SnO_x.

After confirming the perovskite suitability for tandem applications, we fabricated four-terminal (4-T) perovskite/CIGS tandem solar cells illustrated schematically in Figure 7.2. With a CIGS bottom subcell, the semi-transparent perovskite top-cell used in this work was in a typical stack composed of TCO/SnO_x/C60-Self-Assembled-Monolayers (SAM)/SiO_2 NPs/Perovskite/spiro-OMeTAD/MoO_x/TCO. Briefly, we deposited the electron transport layer (ETL) SnO_x on different TCOs (such as fluorine doped tin oxide, FTO and hydrogenated indium oxide, IO:H) via atomic layer deposition (ALD). Before the absorber deposition, we functionalized the surface of SnO_x with a C60-SAM in order to reduce nonradiative recombination at the interface[17] and deposited SiO_2 nanoparticles (NPs) to increase the wetting of the surface. The wide band gap perovskite absorber, $Cs_{0.10}MA_{0.15}FA_{0.75}PbI_2Br$ was then deposited by a two-step spin-coating procedure employing the antisolvent method. The solar cells were finalized by spin-coating of 2,2′,7,7′-tetrakis(N,N-dimethoxyphenylamine)-9,9′-spirobifluorene (Spiro-OMeTAD) as the hole transport layer and sputtering of TCO back electrodes (such as indium doped zinc oxide, IZO or IO:H). The detailed description of the device fabrication can be found in the Experimental Section.

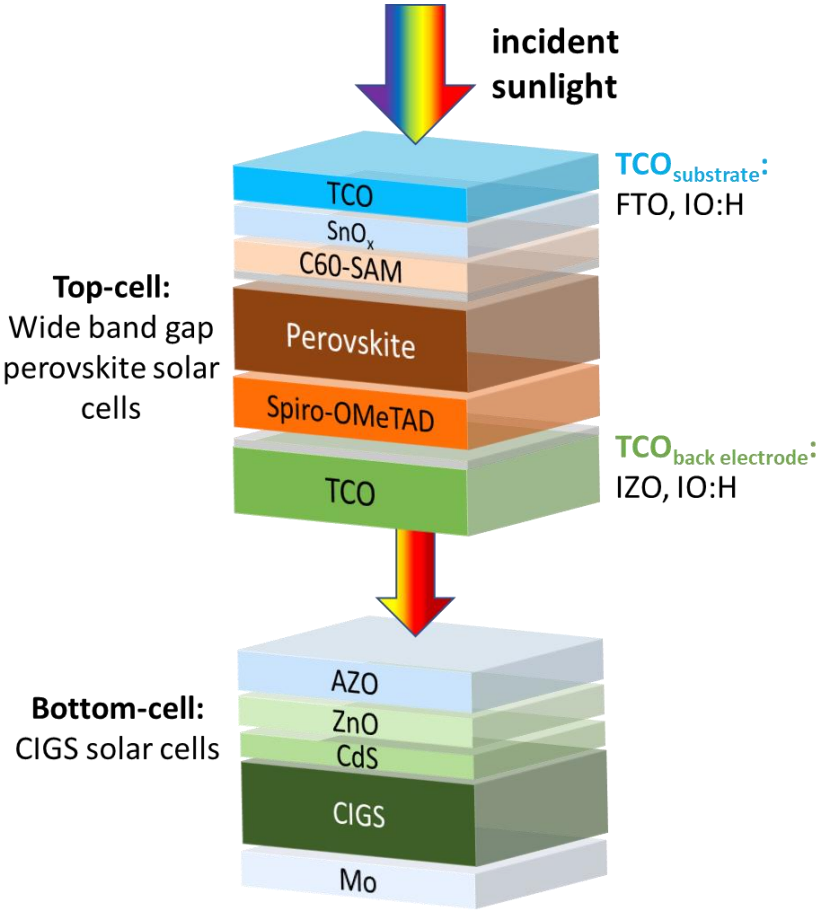

Figure 7.2 Device architectures used in this work.

7.2.1 Transmittance of Transparent Conductive Oxides in Tandems

In tandem solar cells, the efficiency of the configuration strongly depends on the design of a semi-transparent perovskite subcell with excellent photovoltaic performance and concurrently outstanding transparency to allow as many photons as possible in the long wavelength region to reach the bottom device. To this end, we fabricated semi-transparent PSCs with different TCOs (as a substrate and a back electrode) to investigate the effect of tranparency of the top-cell on the performance of the CIGS subcell.

First, we prepared PSCs on different substrates, namely IO:H and FTO, to investigate the substrate transparency. As shown in Figure 7.3A, the transmittance of the perovskite filter rises significantly around 700 nm, leading to an efficient transmittance of low-energy photons for the bottom CIGS solar cells, with an average value of around 75 % and 65 % for PSCs with IO:H and FTO substrates, respectively. Next, we analyzed the influence of transmittance of the back electrode in PSCs on the CIGS performance by preparing semitransparent PSCs on FTO and IO:H substrates with different back-electrodes such as IZO and IO:H. For a given substrate (FTO or

IO:H), the transmittance of the PSCs does not differ substantially, regardless of the type of back electrode (Figure 7.3B). For example, the same back electrode shows different transmittance on different substrates (green and blue solid lines in Figure 7.3B) or similar transparency on the same substrates (green solid and dotted lines in Figure 7.3B). Thus, we conclude that the choice of substrate decides the transparency of the top-cell rather than the back electrode in tandem solar cells.

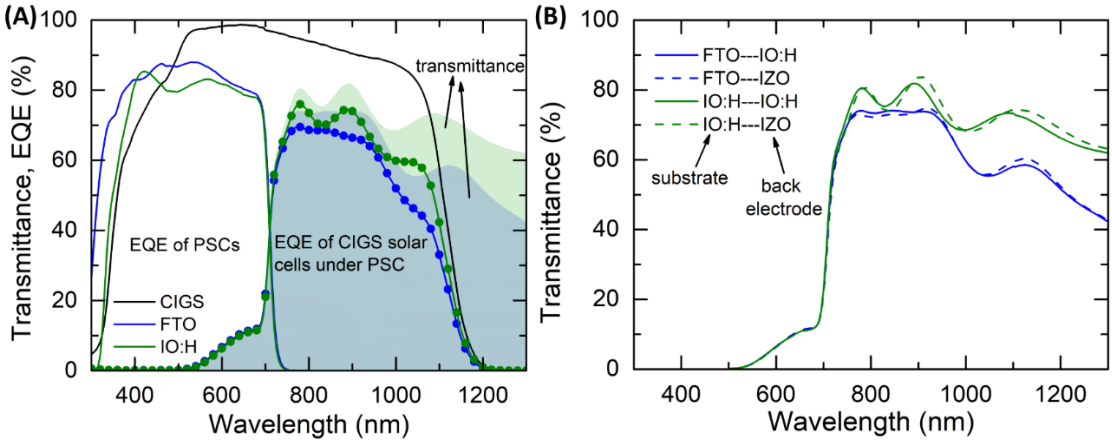

Figure 7.3 (A) Transmittance of PSCs on FTO and IO:H and EQE of PSCs and CIGS solo and under perovskite filter. The blue and green solid curves represent the EQE of PSCs with FTO and IO:H substrates, respectively. The blue and green solid lines with dots represent the EQE of CIGS solar cells under PSCs with FTO and IO:H, respectively. (B) Transmittance of semitransparent PSCs in different combinations of TCOs as a substrate and back electrode.

The higher transmittance of IO:H substrates (Figure 7.3A), particularly in the long wavelength region (~1000 nm) enables achieving higher CIGS performance under the perovskite filter. For instance, as seen in Table 7.1, the performance of CIGS solar cells under IO:H based perovskite solar cells is almost 1% higher than that achieved with the FTO counterparts (8.61 and 9.46 % for FTO and IO:H substrates, respectively), consistent with the higher EQE of the same cells (lines with dots in Figure 7.3A). Furthermore, as seen in Table 7.1, the performance of CIGS solar cells under the perovskite filter on the same substrate with different back electrodes is similar (8.69 % for IZO and 8.61 % for IO:H), confirming that the transparency of the PSCs does not change with different back electrodes. Thus, the overall tandem efficiencies reach 18.8 and 17.8 % for FTO and IO:H substrates with IO:H as a back electrode, respectively (Table 7.1).

Table 7.1 Performance summary of perovskite cells on different substrates (S) with a back electrode of IO:H and different back electrodes (BE) on FTO substrates, CIGS stand-alone and with filter, and 4-T tandem cell. (RS:reverse scan and FS:forward scan)

		PCE (%)	**V_{oc} (V)**	**J_{sc} (mA/cm^2)**	**FF**
Perovskite top-cell	**RS**	10.22	1.05	15.35	0.64
FTO (S) – IO:H (BE)	**FS**	10.07	1.09	15.34	0.60
CIGS	**without filter**	20.94	0.71	38.52	0.77
	with filter	8.61	0.68	16.30	0.78
4-T tandem cell - FTO		18.83			
Perovskite top-cell	**RS**	8.33	1.12	14.95	0.50
IO:H (S) – IO:H (BE)	**FS**	7.83	1.12	14.91	0.47
CIGS	**without filter**	21.06	0.71	38.56	0.77
	with filter	9.46	0.68	17.72	0.79
4-T tandem cell - IO:H		17.79			
Perovskite top-cell	**RS**	8.69	1.10	14.80	0.59
FTO (S) – IZO (BE)	**FS**	8.47	1.11	14.77	0.52
CIGS	**without filter**	21.26	0.71	38.35	0.78
	with filter	8.69	0.68	16.19	0.79
4-T tandem cell - IZO		17.38			

Moreover, the current-voltage (*J-V*) measurements of both subcells are shown in Figure 7.4, highlighting that semitransparent PSCs with different substrates show almost no hysteresis. As seen in Table 7.1, the PSCs exhibit a PCE of 10.22 %, a short-circuit current (J_{sc}) of 15.35 mA/cm^2, a fill factor (*FF*) of 64 % and an open-circuit voltage (V_{oc}) of 1.05 V on FTO, whereas the performance decreases to 8.33 % with a J_{sc} of 14.95 mA/cm^2, a *FF* of 50 % and a V_{oc} of 1.12 V in IO:H cells. Furthermore, the EQEs of the semitransparent PSCs (Figure 7.3A) show a very sharp edge at the bandgap around 730 nm and closely follow the absorption data (Figure 7.1B). The better performance of FTO cells can be also explained by EQE results, as these substrates absorb more in the short wavelength range (~300 nm) than IO:H cells as shown in Figure 7.3A.

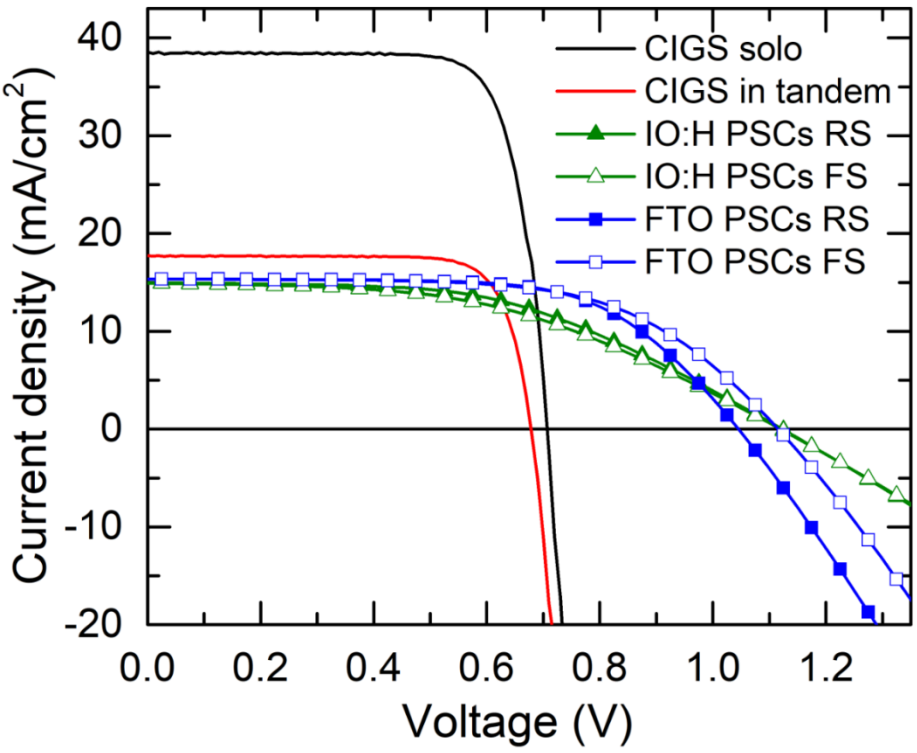

Figure 7.4 *J-V* curves of the CIGS cell with and wihout perovskite filter as well as reverse and forward scan of semitransparent PSCs on different substrates with a back electrode of IO:H. Black solid line stands for *J-V* curve of stand-alone CIGS, whereas red solid line represents the *J-V* curve of CIGS in tandem configuration. Blue and green curves show the *J-V* scans of PSCs with FTO and IO:H sunbstrates in tandem configuration, respectively. Filled and unfilled dots are for reverse (RS) and forward scan (FS).

7.2.2 Is V_{oc} Improving with an Increase in Band Gap?

Raising the Br content is effective at increasing the band gap of the structure, yet equivalent rises in the V_{oc} fail to materialize in full devices.[18] Therefore, the V_{oc} of wide band gap solar cells used above in tandem configuration is still limited to below 1.2 V, corresponding to a high voltage deficit of 550 mV compared to ~400 mV in lower-bandgap perovskite counterparts.[19] This could be due to the segregated phases in the mixed halide perovskites, where the band gap is lowered due to the iodide-rich domains which pin the V_{oc}.[20] Therefore, we conducted a series of XRD measurements on the perovskite, $Cs_{0.05}(FA_{0.83}MA_{0.17})_{0.95}Pb(I_{0.83}Br_{0.17})_3$, under illumination and bias.

Figure 7.5A and B show the comparison of the perovskite peaks at 24.6° and 28.4° and before and after illumination patterns clearly reveal changes in the peak shape and thereby the crystal structure, in particular on the small-angle side. This small-angle feature can be hypothesized to

be due to ascribed to the formation of an iodide-rich phase under illumination due to the increased lattice parameter compared to the original peak. The formation of a smaller shoulder-like feature on the large-angle side also indicates a Br-rich phase. Furthermore, we analyzed the evolution of the peak at 14.1° as seen in Figure 7.5C, exhibiting asymmetric broadening (green to red curve) on the small-angle side, which can be again attributed to the formation of a dominant iodide-rich phase. The Full-Width at Half-Maximum (FWHM) of this peak in Figure 7.5D continously increases with time due to more pronounced halide segregation and increasing inhomogeneity of the cystal structure.

However, these structural changes are fully reversed after 7 days without illumination and bias to their original positions as seen in all XRD patterns and FWHM in Figure 7.5. Therefore, we attribute the V_{oc} deficiency in wide band gap perovskites to the phase segregation under illumination and bias due to halide migration, assuming that these structural changes will be more dominant in wide band gap perovskites containing 33 % Br.

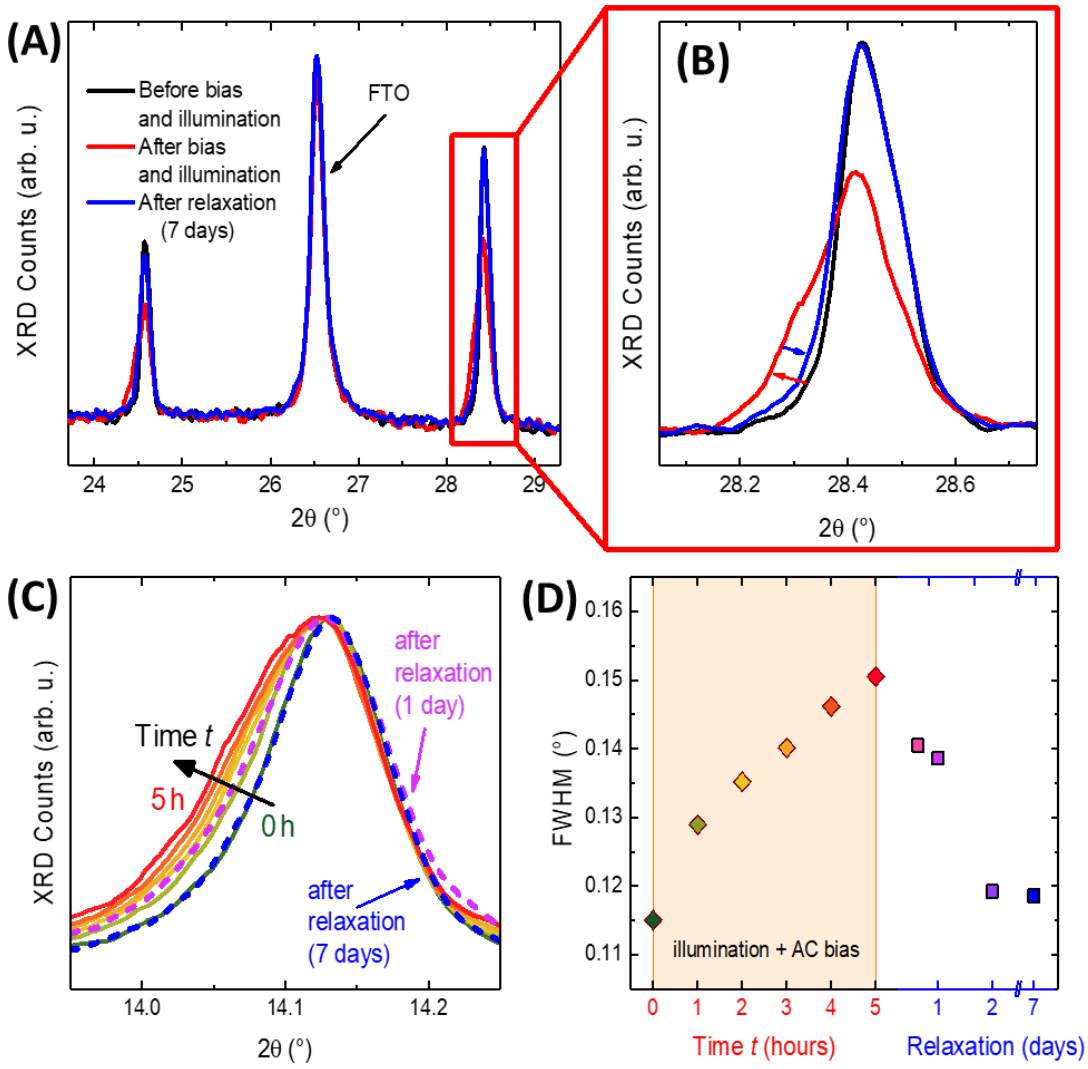

Figure 7.5 (A) XRD spectra of the perovskite peaks at 24.6° and 28.4° before and after illumination and bias as well as after relaxation. (B) Enlargement of the perovskite peak at 28.4°. (C) Monitoring of the perovskite peak at 14.1° under white-light illumination and AC bias by in-situ XRD measurements. (D) Full-Width at Half-Maximum of the 14.1° peak in (C).

7.3 Future Outlook

The tandem configuration used in this work in principle has the potential to break a world-record of perovskite/CIGS tandem solar cells, but it is presently limited by the *PCE*s of PSCs despite the outstanding performance of the stand-alone CIGS cell. The *PCE* losses in PSCs in this work are attributed to the architectural design of the PSCs, which causes some shorting in the solar cells, particularly in IO:H substrates. In addition to this, the active area might be damaged during the cutting of the solar cells in order to fit on top of CIGS solar cells. However, these issues can be

easily solved by a new design for the PSCs. Lastly, we believe that using an optical coupling spacer between the two cells will also push the performance of CIGS tandem cells since it minimizes the optical loss for the bottom-cell resulting from the multiple reflections in the air gap between the subcells.[21]

Additionally, the low V_{oc} is still a problem in wide band gap PSCs but we believe that this challenge can be tackled by the following suggested solutions. First, smaller cations like potassium ions which possibly locate on the defect sites in the perovskite structure and stabilize the perovskite structure further[22] can be used in order to prevent the halide segregation. Furthermore, the reason of V_{oc} deficiency can be a misalignment of the Fermi levels between perovskite and HTL. With the incorporation of bromide into the perovskite structure, the VB of perovskite is lowered, meaning that holes cannot be collected efficiently due to the larger difference[23] in between the VB of perovskite and HTL. In this case, charges will accumulate at the interface and increase the charge recombination, causing a decrease in V_{oc} of PSCs. Therefore, HTLs with a deeper VB might solve this problem and improve the V_{oc} of PSCs, provided the misalignment is the reason for the V_{oc} deficiency.

7.4 Conclusion

In conclusion, we have optimized the transparency of perovskite top-cell in 4-T perovskite/CIGS tandem solar cells by using different TCOs in the top-cell, achieving 75 % transmittance. We revealed that the IO:H used as a substrate has a higher transmittance than FTO counterparts in the long wavelength region, which improves the CIGS performance under a semitransparent perovskite filter by allowing more photons to pass through to the bottom-cell. In addition, our results showed that the transmittance of the substrate is more critical than the back electrode's since PSCs with IZO and IO:H as back electrodes led to similar PCEs in CIGS. Furthermore, the V_{oc} deficiency in PSCs was ascribed to the phase segregation in mixed halide wide band gap perovskite caused by illumination and bias during the *J-V* measurements. Thus, in addition to transparency improvement of perovskite top-cell, we believe that overall efficiency of tandem solar cells can be further boosted by redesigning the architecture of PSCs and preventing V_{oc} losses in PSCs.

7.5 Experimental Section

7.5.1 ETL Deposition

Fluorine-doped tin oxide (FTO) coated glass substrates (<7 Ω/sq) were patterned by etching with zinc powder and HCl solution (3 M). The substrates were washed with deionized water and a 2% Hellmanex detergent solution. They were consecutively cleaned with deionized water, acetone and ethanol and dried by pressurized air. The substrates were further cleaned by oxygen plasma for 5 min before the deposition of ETL.

SnO_x ETL was prepared by atomic layer deposition on FTO coated glass substrates. Tetrakis(dimethylamino)tin (IV) (TDMASn, Strem, 99.99%) was used as a tin precursor. The deposition was conducted at 118 °C with a base pressure of 5 hPa in a Picosun R-200 Advanced ALD reactor. The precursor was held in a glass vessel at 75 °C. Ozone was produced by an ozone generator (INUSA AC2025). Nitrogen (99.999%, Air Liquide) was used as the carrier gas and purge gas with a flow rate of 50 sccm. The growth rate measure, determined by ellipsometry on Si (100) substrates placed next to the FTO during depositions, was 0.69 Å/cycle. The Cauchy model was used for the SnO_x layer.

The ETLs were functionalized with C60-SAM (Aldrich), where a concentration of 0.5 mg/mL in anhydrous chlorobenzene (CB, Sigma Aldrich, 99.8%) was heated to 50 °C for 30 min to dissolve. Later, this solution was filtered through a PTFE syringe filter after it cooled down. It was spin-coated at 3000 rpm for 30 s on substrates with ETLs which were plasma-cleaned for 5 min. Lastly, these films were annealed at 120 °C for 10 min. In order to increase the wetting of the surface after deposition of C60-SAM, we spin-coated 0.2 wt% of SiO_2 nanoparticles (NPs) in anhydrous ethanol at 2000 rpm for 30 s and the substrates were annealed at 100 °C for 10 min. The SiO_2 NPs were synthesized following a procedure reported by Bogush *et al.*[24], using fixed amounts of ethanol (2.71 ml), ammonia (101 µl) and tetraethyl orthosilicate (TEOS, 114 µl) and H_2O (27 µl) for 3 mL of a 1.2 wt% dispersion. The solution was stirred at 30° C for 3 hours, resulting in a size of around 20 nm.

7.5.2 Perovskite Deposition

The cations methylammonium bromide (MABr), methylammonium iodide (MAI), formamidinium bromide (FABr), formamidinium iodide (FAI) were purchased from Dyesol. Cesium bromide (CsBr, 99.999% metals basis) was purchased from Alfa Aesar. Cesium iodide (CsI, 99.999%) and all solvents (anhydrous) were purchased from Sigma Aldrich. Lead iodide

(PbI_2), and lead bromide ($PbBr_2$) were purchased from TCI. All chemicals were used without any further purification.

The perovskite solution for $Cs_{0.10}MA_{0.15}FA_{0.75}PbI_2Br$, was prepared by mixing 1.3 M solutions of $FAPbI_2Br$, $MAPbI_2Br$ and $CsPbI_2Br$ at a ratio of 75%:15%:10% in volume percentage. $FAPbI_2Br$ and $MAPbI_2Br$ were dissolved in the mixture of dimethyformamide (DMF):dimethylsulfoxide (DMSO) (4:1 of volume ratio), whereas $CsPbI_2Br$ was dissolved in pure DMSO due to the low solubility in DMF and heated up at 80 °C for 30 min. The exact amounts of the precursors are shown in Table 7.2. The perovskite deposition was performed in a nitrogen-filled glove-box by spin-coating of the precursor solution on the substrates with a 2-step program consisting of 2000 rpm 10 s and 6000 rpm for 20s. 10s before the program ends, chlorobenzene (CB) was dropped on the spinning sample to accelerate the crystallization process. The sample was annealed at 100 °C for 30 min.

Table 7.2 The exact amount of the precursors for the preparation of perovskite solution.

	Chemicals	**Mol concentration (M)**	**Weight (mg)**
1 mL - $FAPbI_2Br$ DMF:DMSO (4:1)	FAI	0.87	149.6
	FABr	0.43	53.8
	PbI_2	0.87	401.1
	$PbBr_2$	0.43	157.8
1 mL - $MAPbI_2Br$ DMF:DMSO (4:1)	MAI	0.87	138.3
	MABr	0.43	48.2
	PbI_2	0.87	401.1
	$PbBr_2$	0.43	157.8
1 mL - $CsPbI_2Br$ DMSO	CsI	0.87	226.2
	CsBr	0.43	91.6
	PbI_2	0.87	401.1
	$PbBr_2$	0.43	157.8

7.5.3 HTL and Back Electrode Deposition

2,2',7,7'-tetrakis-(*N*,*N*-di-*p*-methoxyphenyl-amine)-9,9'-spirobifluorene (75 mg, spiro-OMeTAD, Borun Chemicals, 99.8%) was dissolved in 1 mL of anhydrous chlorobenzene and filtered through a 0.45 µm syringe filter. Later, this solution was doped with 10 µL 4-*tert*-butylpyridine (Sigma-Aldrich, 96%) and 30 µL of a 170 mg/mL lithium bistrifluoromethanesulfonimidate (Li-TFSI) (Sigma-Aldrich, 99.95%) solution dissolved in

anhydrous acetonitrile (Sigma-Aldrich). This solution was deposited by spin-coating at 1500 rpm 40 s and 2000 rpm 5 s in a nitrogen-filled glove-box. The samples were stored in air at a relative humidity of 25-30%. 40 nm of Au was deposited as a back electrode by thermal evaporation at $9 \cdot 10^{-7}$ mbar.

Molybdenum(VI) oxide (Sigma, 99.97%) was thermally evaporated in a Leybold Univex 450 vacuum system. The deposition rate (up to 1 nm/s) and layer thickness was adjusted via the heating current of the boron nitride crucible and controlled by a quartz crystal unit.

All sputtering processes were performed in a von Ardenne CS730S cluster system at ambient temperature with a base pressure before sputtering of 10^{-7} mbar. During sputtering the pressure was adjusted by a butterfly valve and the total gas flow. The total sputtering gas flow was controlled by three mass flow controllers attached to pure argon gas, a mixture of argon-hydrogen (8%, 5N, Air liquide) and argon-oxygen (8%, 5N, Air liquide). IO:H was deposited via reactive sputtering (DC) from a In_2O_3 target (Toshima, 4N , d = 200 mm) with a gas mixture of hydrogen, oxygen and argon. IZO was sputter-deposited (DC) from a $(In_2O_3)_{0.9}(ZnO)_{0.1}$ target (Toshima, 4N, 200 mm) in a oxygen argon sputtering atmosphere. The sputtering conditions for the layers are shown in Table 7.3.

Table 7.3 The sputtering conditions for TCO preparation in semitransparent solar cells.

Layer	Power (W)	Pressure (µbar)	O_2 (%)	H_2 (%)	Total gas flow (sccm)	Time (s)	Thickness (nm)
IO:H	800	5	2.8	2.8	45	75	160
IZO	800	15	1.2	0	45	75	180

7.5.4 CIGS Solar Cells

CIGS solar cells have been supplied by ZSW Baden-Württemberg and were fabricated according to the published procedure.[25]

7.5.5 Solar Cell Characterization

J-V measurements were performed under a WACOM WXS-90S-5 Solar simulator (IEC-60904-9, Class A). A customized 3D-printed setup was used to align the top cell and bottom cell on top of each other with an air filled gap of 2 mm in between. Each subcell has exactly the same aspect ratio with an area of A = 0.5 cm². The *J-V* responses of the cells were measured simultaneously

using customized software and a Keithley 2000. The perovskite top cell was pre-biased for 5 s at 1.5 V before measuring reversely from 1.5 to -0.2 V at 0.2 V/s and subsequently forward from -0.2 V to 1.5 V. The CIGS bottom cell was measured from -0.2 V to 0.8 V at 0.2 V/s.

The transmittance and quantum efficiency measurements were performed with a Bentham PVE300 device characterization system and the corresponding BENWIN+ Software v3.0. An integrational sphere was used to detect the diffuse and direct transmittance of the perovskite top cell in a wavelength range of 300-1300 nm. The EQEs of top and bottom cells were measured without extra light biasing in the same wavelength regime at a chopper frequency of 500 Hz. Before measurement, the system was calibrated using a Si- (300-1100 nm) and Ge-detector (800-1800 nm). The same 3D-Printed holder as in the *J-V* measurements was used to stack the tandem cell.

7.5.6 Characterization of Perovskite Films

XRD measurements were performed with a Bruker D8 Discover X-ray diffractometer operating at 40 kV and 30 mA, employing Ni-filtered Cu $K_{\alpha 1}$ radiation (λ = 1.5406 Å) and a position-sensitive LynxEye detector. XRD patterns were smoothed using a Savitzky-Golay algorithm in Figure 7.5. Samples were illuminated using a simulated LED solar spectrum at a tilted angle, resulting in an intensity of around 0.4 sun. An AC bias was applied by a Tektronix AFG3022 digital function generator. Measurements were performed under ambient conditions in air (relative humidity (34 ± 5) %, temperature (24 ± 2) °C).

To realize a reasonable compromise between measurement time (~30 min) and resolution for the in-situ measurements, we focused on rather small 2θ intervals and recorded X-ray diffractograms consecutively every hour while illuminating the sample with a solar-spectrum white-light LED (~0.4 sun, due to tilted angle) and applying an AC bias with an amplitude of V_{max} = ± 0.5 V at a frequency f = 990 Hz. Additionally, as an overview, diffractograms from 10° to 30° were recorded before and after illumination (presented here from 23.7° to 29.3°). The relaxation of the crystal structure was monitored after 1, 2, and 7 days in the dark without any bias.

Absorbance spectra were recorded using a PerkinElmer Lambda 1050 spectrophotometer equipped with a 150 mm integrating sphere.

7.6 References

1. Yu, Z.; Leilaeioun, M.; Holman, Z., *Nature Energy* **2016,** 1, 16137.
2. Bailie, C. D., et al., *Energy Environ. Sci.* **2015,** 8, 956-963.
3. McMeekin, D. P., et al., *Science* **2016,** 351, 151-155.
4. Chen, B.; Zheng, X.; Bai, Y.; Padture, N. P.; Huang, J., *Adv. Energy Mater.* **2017**, 1602400-n/a.
5. Teodor, T.; Talia, G.; Oki, G.; Seog, L. Y.; Charles, S.; Liang-Yi, C.; Supratik, G., *Adv. Energy Mater.* **2015,** 5, 1500799.
6. Xiao, Z., et al., *Materials Science and Engineering: R: Reports* **2016,** 101, 1-38.
7. Bush, K. A., et al., *Nature Energy* **2017,** 2, 17009.
8. Yazeed, A., et al., *Adv. Funct. Mater.* **2014,** 24, 6629-6638.
9. Tanabe, K.; Watanabe, K.; Arakawa, Y., *Scientific Reports* **2012,** 2, 349.
10. Manda, X., et al., *Angew. Chem.* **2014,** 126, 10056-10061.
11. Deng, Y.; Peng, E.; Shao, Y.; Xiao, Z.; Dong, Q.; Huang, J., *Energy Environ. Sci.* **2015,** 8, 1544-1550.
12. Kyeongil, H.; Yen-Sook, J.; Youn-Jung, H.; H., S. F.; E., W. S.; Jegadesan, S.; J., J. D.; Dong-Yu, K.; Doojin, V., *Adv. Mater.* **2015,** 27, 1241-1247.
13. Shen, H., et al., *Energy Environ. Sci.* **2018**.
14. Albrecht, S., et al., *Energy Environ. Sci.* **2016,** 9, 81-88.
15. Lal, N. N.; Dkhissi, Y.; Li, W.; Hou, Q.; Cheng, Y.-B.; Bach, U., *Adv. Energy Mater.* **2017,** 7, 1602761.
16. De Wolf, S.; Holovsky, J.; Moon, S.-J.; Löper, P.; Niesen, B.; Ledinsky, M.; Haug, F.-J.; Yum, J.-H.; Ballif, C., *J. Phys. Chem. Lett.* **2014,** 5, 1035-1039.
17. Wojciechowski, K., et al., *ACS Nano* **2014,** 8, 12701-12709.
18. Bush, K. A.; Frohna, K.; Prasanna, R.; Beal, R. E.; Leijtens, T.; Swifter, S. A.; McGehee, M. D., *ACS Energy Lett.* **2018**, 428-435.
19. Kim, J., et al., *Adv. Mater.* **2018,** 30, 1706275.
20. Zhou, Y., et al., *ACS Appl. Mater. Interfaces* **2016,** 8, 2232-2237.
21. Zhao, D.; Wang, C.; Song, Z.; Yu, Y.; Chen, C.; Zhao, X.; Zhu, K.; Yan, Y., *ACS Energy Lett.* **2018,** 3, 305-306.
22. Nam, J. K.; Chai, S. U.; Cha, W.; Choi, Y. J.; Kim, W.; Jung, M. S.; Kwon, J.; Kim, D.; Park, J. H., *Nano Lett.* **2017,** 17, 2028-2033.
23. Yao, D.; Zhang, C.; Pham, N. D.; Zhang, Y.; Tiong, V. T.; Du, A.; Shen, Q.; Wilson, G. J.; Wang, H., *J. Phys. Chem. Lett.* **2018,** 9, 2113-2120.

24. Bogush, G. H.; Tracy, M. A.; Zukoski, C. F., *Journal of Non-Crystalline Solids* **1988,** 104, 95-106.

8 Conclusion

This thesis focused on the intrinsic degradation factors of halide perovskites in device concepts covering lighting devices and solar cells. In the first part, a solution to reduce the hysteresis of perovskite solar cells is suggested by tuning the Fermi level alignment between SnO_x ETL and perovskite absorber. Thermal annealing the SnO_x ETL at different temperatures in air allows for the fine-tuning of their Fermi level. A strong correlation between the Fermi level positions of SnO_x and trap depth suggest that deep traps cause charge accumulation at the interface, leading to enhanced charge recombination at the ETL-perovskite interface which results in higher hysteresis in solar cells on the basis of the trapping-detrapping charge transport mechanism in SnO_x layers. Together with partially eliminating trap states in the ETL or at the ETL-absorber interface, a reduction in the trap energy provides a better Fermi level alignment and hence in more efficient and hysteresis-free solar cells.

The investigations of charge transport characteristics by ToF measurements demonstrate that the mobilities for both electrons and holes are decreased by 3 orders of magnitude in the stacked solar cells compared to perovskite-only-thin films. This result strongly suggests that the perovskite cannot be a charge transport-limiting factor in the photovoltaic devices. Complementary studies where the thicknesses of the charge extraction layers are varied show that the transit time of charge carriers significantly increases with thicker layers of both TiO_2 and spiro-OMeTAD, concluding that the transport time of photoinduced charge carriers is mainly determined by the charge-selective layers.

Furthermore, the scope of the halide perovskites was extended to the synthesis of hybrid organic-inorganic perovskite nanoparticles (NPs) with two different organic cations and their application in lighting devices constructed according to the concept of LECs. Exchanging the cations from MA to FA results in a red-shift in both emission and absorbance spectra as well as six times lower recombination rate, leading to a lower PLQY, and in turn to a lower device performance. LEC devices based on these NPs demonstrate the importance of the electrolyte matrix by showing stable luminance, while those without this component do not exhibit any EL features.

The NP concept together with their application in lighting devices was further studied by exchanging the organic cations with Cs to obtain $CsPbX_3$. The corresponding nanocrystals (NCs) were synthesized *via* a hot injection method, resulting crystalline NCs featuring a homogenous size distribution and in high PLQYs. The inorganic mixed halide NCs comprising bromide- and

iodide-based LECs emitted at around 8 cd/m^2 at low driving currents. The use of the salt KCF_3SO_3 in the active layer decreased the injection voltage and also prevented the halide segregation in the perovskite NCs, attributed to a further stabilization of the perovskite lattice with potassium ions.

Finally, the importance of the transparency of the perovskite top-cell was unveiled in 4-terminal (4-T) perovskite/CIGS tandem solar cells, employing different TCOs as substrates as well as back electrodes. It was found that the transparency of the top-cell is determined by the transparency of the substrate rather than the semitransparent back electrode. Here, IO:H substrates can achieve higher transmittance at the long wavelength region in comparison with FTO counterparts. The observed V_{oc} loss in the resulting tandem cells is attributed to an intrinsic feature of these perovskites, namely halide segregation indicated by XRD measurements.

Although halide perovskite optoelectronics have shown almost the same improvements in a few years as 50 years of silicon solar cell research, there are still several important hurdles to tackle for potential industrial applications. Their instability towards extrinsic factors such as UV light, moisture and oxygen is one of the main concerns of halide perovskites. However, these issues can be presumably alleviated by using the sealing technologies that have been developed for organic electronics. On the other hand, the intrinsic degradation processes associated with the perovskite material itself still remain as a serious issue requiring further mechnaistic research.

Despite the efforts presented in this thesis to prevent the hysteresis of PSCs associated with intrinsic features of perovskites, more efforts should be invested to understand the origin and mechanism of this phenomenon. Interface engineering is expected to offer ways to remove the hysteresis. On the other hand, the favorable and tunable optical band gap of these materials provides an advantage over other photovoltaic materials in tandem configurations with crystalline silicon and CIGS solar cells as well as potential colourful applications in lighting devices. Although a solution is suggested in this thesis to prevent the halide segregation, the long-term stability of wide band gap lead halide perovskite materials is not known yet. With the great body of knowledge developed and with the enormous advances achieved so far, a bright future is expected for this intriguing family of optoelectronic materials.

Curriculum Vitae

List of Publications

Mechanically Stacked Perovskite/CIGS Tandem Solar Cells
Meltem F. Aygüler, Moritz Schultes, Tim Helder, Alexander G. Hufnagel, Sebastian Haeringer, Thomas Bein, Erik Ahlswede and Pablo Docampo, *Manuscript in preparation*

Light-Emitting Electrochemical Cells Based on Inorganic Metal Halide Perovskite Nanocrystals
Meltem F. Aygüler, Bianka M. D. Puscher, Yu Tong, Thomas Bein, Alexander S. Urban, Rubén D. Costa and Pablo Docampo, J. Phys. D, **2018**, 51 (33), 334001

Understanding the Role of Cesium and Rubidium Additives in Perovskite Solar Cells: Trap States, Charge Transport, and Recombination
Yinghong Hu, Eline M. Hutter, Philipp Rieder, Irene Grill, Jonas Hanisch, Meltem F. Aygüler, Alexander G. Hufnagel, Matthias Handloser, Thomas Bein, Achim Hartschuh, Kristofer Tvingstedt, Vladimir Dyakonov, Andreas Baumann, Tom J. Savenije, Michiel L. Petrus and Pablo Docampo, Adv. Energy Mater., **2018**, 8 (16), 1870073

Influence of Fermi Level Alignment with Tin Oxide on the Hysteresis of Perovskite Solar Cells
Meltem F. Aygüler, Alexander G. Hufnagel, Philipp Rieder, Michael Wussler, Wolfram Jaegermann, Thomas Bein, Vladimir Dyakonov, Michiel L. Petrus, Andreas Baumann and Pablo Docampo, ACS Appl. Mater. Interfaces, **2018**, 10 (14), 11414-11419

Charge Transport Limitations in Perovskite Solar Cells: The Effect of Charge Extraction Layers
Irene Grill, Meltem F. Aygüler, Thomas Bein, Pablo Docampo, Nicolai F. Hartmann, Matthias Handloser and Achim Hartschuh, ACS Appl. Mater. Interfaces, **2017**, 9 (43), 37655-37661

Impact of Rubidium and Cesium Cations on the Moisture Stability of Multiple-Cation Mixed-Halide Perovskites
Yinghong Hu, Meltem F. Aygüler, Michiel L. Petrus, Thomas Bein and Pablo Docampo, ACS Energy Lett., **2017**, 2 (10), 2212-2218

Unveiling the Dynamic Processes in Hybrid Lead Bromide Perovskite Nanoparticle Thin Film Devices

Bianka M. D. Puscher, Meltem F. Aygüler, Pablo Docampo and Ruben D. Costa, Adv. Energy Mater., **2017**, 7 (15), 1602283

Highly luminescent cesium lead halide perovskite nanocrystals with tunable composition and thickness by ultrasonication

Yu Tong, Eva Bladt, Meltem F. Aygüler, Aurora Manzi, Karolina Z Milowska, Verena A. Hintermayr, Pablo Docampo, Sara Bals, Alexander S. Urban, Lakshminarayana Polavarapu and Jochen Feldmann, Angew. Chem. Int. Ed., **2016**, 55 (44), 13997-13892

Light-emitting electrochemical cells based on hybrid lead halide perovskite nanoparticles

Meltem F. Aygüler, Michael D. Weber, Bianka M. D. Puscher, Dana D. Medina, Pablo Docampo and Rubén D. Costa, J. Phys. Chem. C, **2015**, 119 (21), 12047-12054

Book Chapter

Aygüler M.F., Docampo P. (2017) *Quantum Dot Based Light-Emitting Electrochemical Cells*. In: Costa R. (eds) Light-Emitting Electrochemical Cells. Springer, Cham

Journal Covers

Perovskite Solar Cells: Understanding the Role of Cesium and Rubidium Additives in Perovskite Solar Cells: Trap States, Charge Transport, and Recombination
Cover Picture, Adv. Energy Mater., **2018**, 8 (16)

Perovskite Nanoparticles: Unveiling the Dynamic Processes in Hybrid Lead Bromide Perovskite Nanoparticle Thin Film Devices
Back Cover, Adv. Energy Mater., **2017**, 7 (15)

Oral Presentations

Influence of Fermi Level Alignment with Tin Oxide on the Hysteresis of Perovskite Solar Cells
Meltem F. Aygüler, Alexander G. Hufnagel, Philipp Rieder, Michael Wussler, Wolfram Jaegermann, Thomas Bein, Vladimir Dyakonov, Michiel L. Petrus, Andreas Baumann and Pablo Docampo
International Conference on Hybrid and Organic Photovoltaics (HOPV), **2018**, Benidorm, Spain

Light-Emitting Electrochemical Cells Based on Inorganic Metal Halide Perovskite Nanocrystals
Meltem F. Aygüler, Bianka M. D. Puscher, Yu Tong, Thomas Bein, Alexander S. Urban, Rubén D. Costa and Pablo Docampo
International Conference on Hybrid and Organic Photovoltaics (HOPV), **2018**, Benidorm, Spain

Effects of Annealing Temperature of Tin Oxide Electron Transport Layers on the Hysteresis of Perovskite Solar Cells
Meltem F. Aygüler, Michael Wussler, Alexander Hufnagel, Wolfram Jaegermann and Pablo Docampo
Perovskite Thin Film Photovoltaics (ABXPV), **2017**, Valencia, Spain

Light-Emitting Electrochemical Cells Based on Hybrid Lead Halide Perovskite Nanoparticles
Meltem F. Aygüler, Michael D. Weber, Bianka M. D. Puscher, Dana D. Medina, Pablo Docampo and Rubén D. Costa
1st International Conference on Perovskite Solar Cells and Optoelectronics (PSCO), **2015**, Lausanne, Switzerland

Light-Emitting Electrochemical Cells Based on Hybrid Lead Halide Perovskite Nanoparticles
Meltem F. Aygüler, Michael D. Weber, Bianka M. D. Puscher, Dana D. Medina, Pablo Docampo and Rubén D. Costa
European Materials Research Society Fall Meeting (E-MRS), **2015**, Warsaw, Poland

Poster Presentations

Light-Emitting Electrochemical Cells based on Inorganic Metal Halide Perovskite Nanocrystals
Meltem F. Aygüler, Bianka M. D. Puscher, Yu Tong, Thomas Bein, Alexander S. Urban, Rubén D. Costa and Pablo Docampo
CeNS Workshop, **2018**, Venice, Italy

Light-Emitting Electrochemical Cells based on Inorganic Metal Halide Perovskite Nanocrystals
Meltem F. Aygüler, Bianka M. D. Puscher, Yu Tong, Thomas Bein, Alexander S. Urban, Rubén D. Costa and Pablo Docampo
NIM Conference "The Future of Nanoscience", **2018**, Tutzing, Germany

Effects of Annealing Temperature of Tin Oxide Electron Transport Layers on the Hysteresis of Perovskite Solar Cells
Meltem F. Aygüler, Alexander Hufnagel, Michael Wussler, Wolfram Jaegermann, Thomas Bein[†], Michiel Petrus and Pablo Docampo
SolTech Workshop, **2017**, Munich, Germany

Fully Inorganic Lead Halide Perovskite Nanocrystals for Light-Emitting Electrochemical Cells
Meltem F. Aygüler, Bianka M. D. Puscher, Rubén D. Costa, Thomas Bein and Pablo Docampo
3rd International Congress Next Generation Solar Energy Meets Nanotechnology, **2016**, Erlangen Germany

Fully Inorganic Lead Halide Perovskite Nanocrystals for Light-Emitting Electrochemical Cells
Meltem F. Aygüler, Bianka M. D. Puscher, Rubén D. Costa, Thomas Bein and Pablo Docampo
CeNS Workshop, **2016**, Venice, Italy

Light-Emitting Electrochemical Cells Based on Hybrid Lead Halide Perovskite Nanoparticles
Meltem F. Aygüler, Michael D. Weber, Bianka M. D. Puscher, Dana D. Medina, Pablo Docampo and Rubén D. Costa
NIM Summer Retreat, **2016**, Herrsching, Germany

Light-Emitting Electrochemical Cells Based on Hybrid Lead Halide Perovskite Nanoparticles
Meltem F. Aygüler, Michael D. Weber, Bianka M. D. Puscher, Dana D. Medina, Pablo Docampo and Rubén D. Costa
SolTech Workshop, **2016**, Munich, Germany